Cape Peninsula
University of Technology

STRUCTURAL ANALYSIS OF SPENT NUCLEAR FUEL DRY STORAGE CASKS

THIERRY TSHIBALA KAMPOY

Supervisor: Prof Nawaz Mahomed

Co-supervisor: Prof Graeme Oliver

Bellville campus

August 2020

The thesis is submitted in fulfilment of the requirement for the degree of
Master of Engineering: Mechanical Engineering
in the Faculty of Engineering at
Cape Peninsula University of Technology

DECLARATION

I, Thierry Tshibala Kampoy, declare that the contents of this thesis represent my own unaided work, and that the thesis has not previously been submitted for academic examination towards any qualification. Furthermore, it represents my own opinions and not necessarily those of the Cape Peninsula University of Technology.

Signed…… Date……

ABSTRACT

The structural analysis of the accidental handling drop onto an unconfined concrete floor of a spent nuclear fuel (SNF) interim dry storage cask (IDSC) has been successfully carried out at the transportation stage, using representative material properties for the (IDSC) without shock absorption. The IDSC system consists of a transportable storage cask (TSC) held within a transfer cask (TC), the latter equipped with handles for transportation of the system. This system is used in many nuclear power plants to provide offsite storage of the spent nuclear fuel assemblies. As it can easily be exposed to a handling drop at the transportation stage, this current study has made use of the handling drop as a loading case to determine if it is suitable to use a specific grade of steel and stainless steel to construct the IDSC at the transportation stage while falling on a concrete floor.

The objective was to establish the structural response of the IDSC under an impact force initiated from a nine-metre height. This height is considered the worst case in accidental handling drops in nuclear waste transport operations. Finite element (FE) simulations were performed using ABAQUS/Explicit. The analysis was carried out for three drop orientations: vertical drop and oblique drops at 45 degrees and 60 degrees to the horizontal.

The results showed that the highest stresses experienced by the IDSC occurred with an oblique drop at an angle of 60 degrees to the horizontal. For the particular IDSC design considered, the maximum von Mises equivalent stresses obtained on the outer-shell were beyond the elastic limit of the material for all test cases. This implies that more energy is being absorbed by the outer-shell as compared to the inner-shell.

The vertical drop modelling technique was selected to be tested over two different base surfaces. This included a drop test onto both a deformable (flexible) and a rigid base. The energy absorbed by the IDSC over a rigid base was extremely severe in that the IDSC sheared between the sealing.

Four finer mesh density ratios were chosen for the mesh convergence study. The four mesh density ratios were associated with the ABAQUS/EXPLICIT default mesh sizes, that is, 1:6, 1:8, 1:10, and 1:12. After running the analyses at different mesh ratios, it was established that the results converged adequately at the last three mesh ratios. Therefore, the most preferred mesh density was 1:12 based on the convergence study, which resulted in stable energy transfers. This meant that once the kinetic energy decreased, the internal energy increased slightly, thus rendering the results acceptable. The parameters of the unconfined concrete structure are those of a 50 MPa Grade Concrete based on similar studies conducted

previously. The results also illustrated that a large deformation can be captured at a mesh density ratio of 1:12.

Regions with different high stress concentrations were detected along the height of the TSC at a position of 2 m from the bottom edge (midway) and along the full length of the TC. The equivalent plastic strains (PEEQ) and Von Mises stresses obtained during the vertical drop were lower in magnitudes than those for the two oblique angles of 45 degrees and 60 degrees.

The results obtained were validated against a similar existing study in which LS-DYNA3D and ABAQUS/Explicit were used.

ACKNOWLEDGEMENTS

I would like to direct my genuine gratitude and appreciation to my supervisors for their continuous support, encouragement, and guidance throughout the duration of my research. I also would like to direct my sincere gratitude and appreciation to the laboratory staff of the Product Lifecycle Management Competency Centre (PLMCC) at the Cape Peninsula University of Technology, particularly Ms Nadine de Lille and Mr Michael Peterson, for their technical support and assistance.

Lastly, I would like to express my sincere gratitude and appreciation to Dr Greg Mitchell, at Finite Element Analysis Services (Pty) Ltd., who guided me during the course of my studies.

TABLE OF CONTENTS

LIST OF FIGURES

LIST OF TABLES

GLOSSARY

Acronyms and Abbreviations:

IAEA	: International Atomic Energy Agency
IDSC	: Interim dry storage cask
SNF	: Spent nuclear fuels
TC	: Transfer cask
CC	: Concrete cask
TSC	: Transportable storage canister
SAR	: Safety analysis reports
FE	: Finite element
τ	: Shear strength
τ_y	: Shear yield strength
[k]	: Stiffness matrix of a single element
[B]	: Strain-displacement matrix
[D]	: Elasticity matrix
[C]	: Damping matrix
d_c	: Scalar compression damage variable
d_t	: Scalar tension damage variable
$d\varepsilon^p$	: Corresponding Plastic strain increment
ε_c	: Compressive strain
ε_c'	: Strain at ultimate compressive strength
ε_t	: Tensile strain
ε^p	: Uniaxial plastic strain
ε_c^{pl}	: Equivalent plastic strain in compression
ε_t^{pl}	: Equivalent plastic strain in tension
ε_c^{in}	: Cracking strain in compression
ε_t^{ck}	: Cracking strain in tension
E	: Young's modulus of a material
E^h	: Element young's modulus of a material
E_{DC}	: Deformed energy of the concrete
E_{DM}	: Deformed energy of the metallic cask
E_0	: Modulus of elasticity in brittle materials
E_K	: Kinetic energy of the IDSC
E_R	: Resistance energy
E_S	: Spalling-resistant energy

E_T : Tunnelling -resistant energy

E_C : Scabbing-resistant energy

$[\mathrm{K}]$: Global stiffness matrix

$[\mathrm{M}]$: Mass matrix

$\mathrm{R}^{\mathrm{ext}}$: External nodal force vector

$\mathrm{R}^{\mathrm{int}}$: Internal nodal force vector

S : Nodal displacement vector

$\dot{\mathrm{S}}$: Global vector of nodal velocities

$\ddot{S}$: Global vector of nodal accelerations

C : Speed of sound

dV : Change in volume of an element

V^{h} : Element volume

V_0 : Original velocity

V_r : Residual velocity of the IDSC after impact

t : Step time

γ : Shear strain

ν : Poisson's ratio

$\Delta\mathrm{t}$: Change in step time

$\Delta\mathrm{tcr}$: Critical time

$\Delta\mathrm{L}$: Change in length

σ : Cauchy true stress

σ_{c} : Compressive stress

σ_{cu} : Ultimate compressive strength of unconfined cylinder

σ_{u} : Ultimate stress

σ_y : Yield stress

σ_0 : Stress vector at a state

σ_1 : Principal stress in a one known direction

σ_{VM} : Von Mises Stress

σ_{YS} : Yielding strength

σ_t : Tensile stress

σ_T : True stress

f : Yielding function

f_{bo} : Initial equibiaxial compressive

fco : Initial uniaxial compressive yield stress

f_c' : Concrete compressive strength

ρ	: Density of a material
C_d	: Average crater diameter
E_d	: Dynamic young's modulus
X_d	: Penetration depth
V	: Impact velocity
Z	: Plastic potential function
ALLAE	: Artificial strain energy for the whole model
ALLIE	: Total internal strain energy for the whole model
ALLKE	: Total kinetic energy for the whole model
C3D8R 3D	: First-order reduced integration solid continuum element
CPU	: Central processing unit
PEEQ	: Equivalent plastic strain

Terms:

Yield Criterion:	A hypothesis concerning the limit of elasticity under any combination of stresses. Since stress and strain are tensor quantities, they can be described on the basis of three principal values; in the case of stresses, these are denoted by σ_1, σ_2 and σ_3.
Maximum Principal Stress Theory:	States that yield occurs when the largest principal stress surpasses the uniaxial tensile yield strength.
Maximum Principal Strain Theory:	States that yield occurs when the maximum principal strain reaches the strain corresponding to the yield point in a simple tensile test.
Maximum Shear Stress Theory:	Assumes that yield occurs when the shear stress (τ) exceeds the shear yield strength (τ_y), also known as the Tresca criterion.
Total Strain Energy Theory:	Assumes that that the stored energy associated with elastic deformation at the point of yield is independent of the specific stress tensor. Thus yield occurs when the strain energy per unit volume is greater than the strain energy at the elastic limit in simple tension.
Distortion Energy Theory:	Proposes that yield occurs when the distortion component of the strain energy exceeds that at the yield point for a simple tensile test; also known as the Von Mises criterion. It also states that the total strain energy can be separated into two components: volumetric (hydrostatic) and shape (distortion/shear) strain energy.
Penetration:	The formation of a crater on the target being impacted at the interface between concrete and IDSC.

1. INTRODUCTION

1.1 Motivation for the Research

The interim dry storage cask (IDSC) is used to confine spent nuclear fuel (SNF) assemblies (Macfarlane, 2001). This storage system should be secure enough to prevent the risk of public exposure to the suggested high-level radioactivity in SNF known as gamma radioactivity (Feiveson et al., 2011). The IDSC process is divided into two main stages: the transportation stage and final disposal stage. During the transportation stage, the IDSC consists of a transfer cask (TC) and a transportable storage cask (TSC) based on the Magnastor system^{TM} (refer to Figure 1.1). At the final disposal stage, the TSC is removed from the TC and stored inside a concrete cask (CC). All possible assumptions and dimensions were taken from a safety analysis report (Magnastor, 2008).

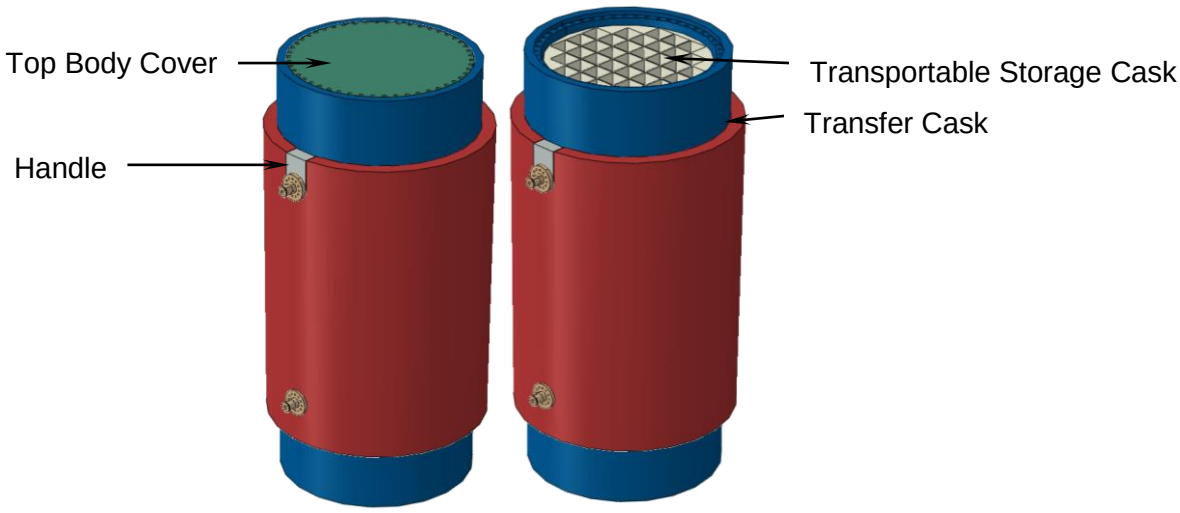

Figure 1.1: A Magnastor Storage System modeled in Solidworks.

Manufacturers of the IDSC, such as Magnastor Storage and Areva Transnuclear, have stated in their safety analysis reports (SAR) that the IDSC has been tested under different load scenarios and accident conditions. This enables one to understand the handling ability of the IDSC (Magnastor, 2008, p 11). However, a detailed study covering all structural behaviours of the IDSC under accidental conditions is not made available in the SAR. Therefore, there is a need to further conduct a study under different possible load scenarios. This research will only study handling drops that are presumed to possibly occur while transferring the IDSC for the final disposal stage.

1.2 IDSC Design Parameters

The designers of IDSCs such as a Magnastor, Transnuclear, Areva and Westinghouse have designed the structure of the IDSC in metallic containers to contain radioactive material such as uranium (Grande, 1992). Therefore, the design of SNF dry storage should ensure its structural integrity under both normal and accidental incidents (Klymyshyn, et al., 2013). This structural integrity could be proven by a range of technical analyses, such as FE-simulations, which is preferred because of proven accuracy for similar structural problems.

The study of handling drop impact on the IDSC is not new; a previous study was conducted using a shock absorber on both ends of the IDSC (Shin Lee et al., 2005). This study investigated the design requirements of the cask by experimental tests and FE-simulations. The materials used in the components of the IDSC are assumed to either exhibit elastic–plastic or elastic–perfectly-plastic behaviour (Magnastor, 2008). The FE analyses were carried out for three drop orientations, which were vertical drop, horizontal drop and oblique drop. The aim was to establish conditions in which large deformations were experienced. The three drop orientations onto a rigid base from a height of 9 m were simulated using both LS-DYNA3D and ABAQUS/Explicit.

1.3 IDSC simulation process

A handling drop of an IDSC system at the transportation stage can be simulated using finite element analysis for analysing structural behaviours. The finite element (FE) analysis is a numerical procedure for analysing the mechanical behaviour of structures and fluids. The software requires the user's understanding of what causes a change in the handling ability of the structure in order to establish the boundary conditions. It is critical that the finite element model used in the simulation is realistic in describing the actual physical conditions involved in the storage system at the transportation stage, in order to obtain realistic results. There are geometric complexities involved in the structural components, material nonlinearity, as well as discontinuous contact pressures between the system components at the transportation stage. Based on these complexities, it is necessary to use a nonlinear solution procedure. However, such finite element procedures require incrementally larger numbers of time steps and iterations, which may result in computational time difficulties. Therefore, this research only makes use of a linear solution to investigate the structural behaviour.

The methods which are crucial for obtaining realistic results are discussed in the theory part of the dissertation, such as: High handling drop velocity as a result of the drop height (9m), which causes effects that need to be considered carefully; the energy absorbed by the IDSC

and the energy absorbed by the concrete floor; and mesh convergence. Different drop orientations were simulated to analyse deformation induced along the length of the IDSC. The use of FE simulations makes it easier to change any parameter of the IDSC and reinforced concrete pad in order to see how such changes affect the handling ability of the structure.

Previous studies presented the results as energy and effective stresses of each component and were compared between the two FE simulation analysis codes, with the effective stress labels as the maximum von Mises stress scale on the inner and outer shells (Shin Lee et al., 2005). However, this did not display a detailed study of the IDSC under the conditions of a handling drop without shock absorption. Hence, there is a need to conduct a study that will cover the analysis of the IDSC without shock absorption.

Aquaro et al.(2009) carried out drop testing of the IDSC, which dealt with the numerical and experimental analysis of a shell-type shock absorber for the IDSC. This study also considered 9 metre free drop tests, which were performed on reduced scale models that were designated as follows: large-scale models (1:2 and 1:6), and small-scale models (1:12). The accuracy of the results was not suitable; however, while using the scale 1:9, a suitable accuracy was met with an error of less than 20%. The experimental results were compared with those from the FE analysis computer codes, taking into account the reduced scale models as well as the prototype (Aquaro et al., 2009).

Therefore, the analysis of the ISDC handling drop test requires an adoption of the conducted studies of Aquaro et al.(2009) and Shin Lee et al.(2005) as a guide, since they have taken into account a worst case scenario of the possible height that the IDSC could be lifted, that of 9m.

The current study will also take into account the same height of 9m using ABAQUS/Explicit finite element code, while the studies referred to have used both LS-DYNA and ABAQUS/Explicit finite element codes. The IDSC in this current study is modelled on that of the Magnastor System. The reason for not replicating the design parameters of the studies of Aquaro et al. (2009) and Shin Lee et al. (2005) is that this study was a practical application based on the situation at the Koeberg Nuclear Power Station in South Africa, where the Magnastor System is deployed. The results obtained from the ABAQUS finite element code for the Magnastor System will be compared with those of these previous studies.

1.4 Background

Dry storage was originally designed to provide temporary off-site storage for spent nuclear fuel (SNF). These assemblies of fuel rods must be replaced from time to time because they

lose their radiation heat efficiency. About one third of the nuclear fuel in a reactor is removed and replaced with fresh fuel at each refuelling. The spent fuel assemblies, which generate a considerable amount of heat and radiation, are placed into spent fuel (boron water) pools at the reactor site, as initial storage, for a period of up to ten years. After their radiation level has reduced to a certain level, the spent fuel assemblies are placed into dry storage systems, referred to as interim dry storage casks (IDSCs), as mentioned previously, for onsite storage and to prevent human exposure (Baker, et al., 2015). Hence, interim dry storage is a method of storing high-level waste, such as SNF, that has already been cooled in the spent fuel pool.

Casks are typically steel cylinders that are either welded or bolted closed. The fuel rods inside are surrounded by helium gas. Ideally, the steel cylinder provides leak-proof containment of the spent fuel. Each cylinder is surrounded by additional steel, concrete, or any other material to provide radiation shielding for workers and members of the public (Rigby, 2010).

Concrete has been used in the construction of nuclear facilities because of two primary properties: its structural strength, and its ability to shield radiation (IAEA, 2004). Concrete structures have been known to last for hundreds of years, but they are also known to deteriorate in very short periods of time when exposed to physical and chemical environmental conditions. This can place the use of concrete in nuclear facilities for containment and shielding of radiation at risk (Baisden & Choppin, 2007). Radioactive materials have made the performance of concrete crucial for the safe operation of spent fuel storage facilities, as SNF is stored in concrete structures, casks, and vaults for planned periods of up to 40 years. This concrete is exposed to several conditions that have been shown to cause it to deterioration. These include freeze thaw, heat, cracking, acids, chlorides, sulfates, carbonation, calcium leaching, and radiation, which are compounded by the aging of these concrete structures. However, this research will focus more on steel casks and stainless steel canisters, taken into account during the transportation stage only.

1.5 IDSC Design Parameters

The South African government currently has an important challenge of meeting potentially increased demand for electricity energy, whilst reducing atmospheric emissions. Nuclear power has begun to attract renewed interest in a growing number of countries as a sustainable option to meet the increasing demand for energy, particularly in the developing economies (Ogunlade, et al., 2006). However, the management and disposal of spent fuel is understood as one of the crucial concerns in nuclear firms (IAEA, 2004). Thus, the emission of radioactive materials must be prevented. Magnastor, which is one of the manufacturers of the IDSC

technology, has provided a reliable design of the IDSC consisting of different components for the confinement of radioactive materials (Magnastor, 2008, p 11).

The wet storage pools at Koeberg Power Station in Cape Town, South Africa, do not have any further available space for SNF (refer to Figure 1.2). Hence, the deployment of interim dry storage systems has become necessary. At the transportation stage, the interim dry storage system consists of a transfer cask (TC) and a transportable storage canister (TSC), while at the final disposal stage, it consists of the transportable storage canister (TSC) and shielding concrete cask.

These structures should not break under normal and accidental conditions, since such damage could cause great disruption to the wellbeing of people living in the vicinity. Hence, this study will investigate the structural behaviour of the IDSC in reaction to handling drops.

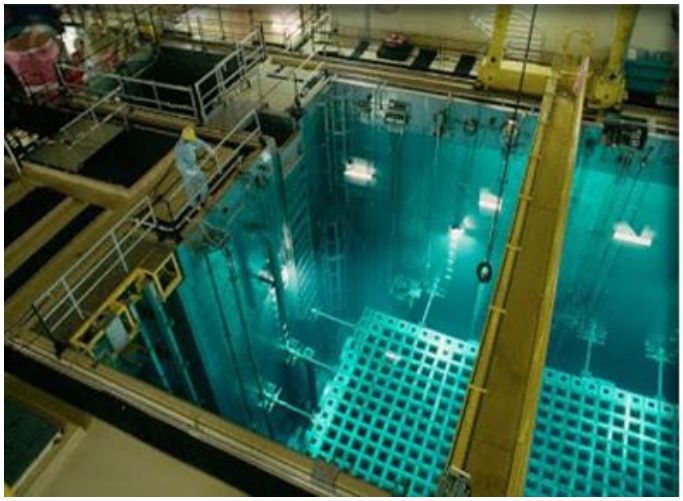

Figure 1.2: Typical wet storage systems used in nuclear engineering firms (IAEA, 2004).

1.6 Research Objectives

This research project was conducted with the following objectives:

- To investigate the structural integrity of the IDSC structure
- To investigate the handling drop at different orientations
- To develop a model describing IDSC material behaviour in order to assess the reliability of the structure
- To develop a model taking into account the interaction between the components of the IDSC structure
- To investigate different modelling orientations and solution procedures and comparing their efficiency and accuracy.

1.7 Research Methodology

The methodology to achieve the aforementioned objectives are outlined below:

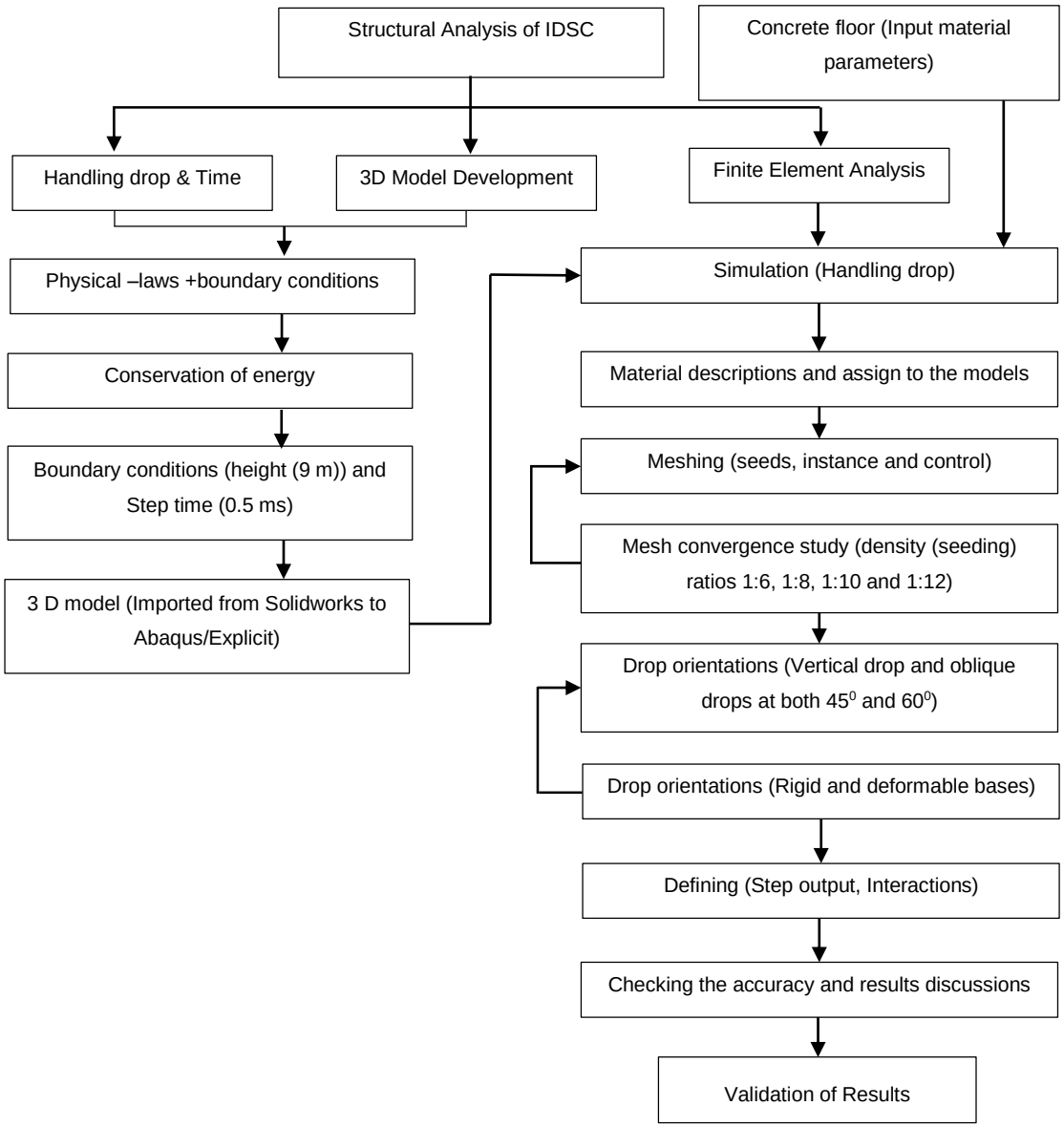

Figure 1.3: General part development and finite element analysis flowchart.

1.7.1 Modelling

This phase involves the modelling of the IDSC, specifically the type manufactured by Magnastor. The modelling approach will consist of examining the structure's requirements in terms of standards and performance, its architecture and as well as design parameters. A model of the IDSC and a reinforced concrete pad was modeled with SOLIDWORKS. This SOLIDWORKS model was later imported to ABAQUS code for FE-simulations.

1.7.2 Simulation

The simulation process was performed in ABAQUS and applied to parametric components of the IDSC. The FE-simulations were carried out based on four different mesh densities (1:6,1:8, 1:10 and 1:12), two base surfaces of which one is deformable and the other one rigid, as well as two different oblique orientations (45 degrees and 60 degrees).

1.7.3 Validation of Results

This section explains the methods used to validate the results to ensure compliance with engineering research. The results obtained from FE simulations were validated by comparing them to similar work simulated using FE analysis. This is to ensure reliability and dependability of the results obtained.

2. LITERATURE REVIEW

2.1 Finite element method

This Chapter provides background studies available in the literature on numerical analysis relevant to the structural analysis of spent nuclear fuel dry storage casks under handling drop loading scenario.

2.1.1 Equilibrium equation for dynamic analysis

The dynamic displacement-based finite element method will be employed in the mechanical structural analysis. An approximate stiffness method is used to determine the displacement field. The typical governing equilibrium equations (Chopra, 1995) are given as follows:

$$[M]\ddot{S} + [C]\dot{S} + [K]S = R^{ext} \tag{2.1}$$

$$[M]\ddot{S} + [C]\dot{S} + R^{int} = R^{ext} \tag{2.2}$$

where [*M*] is the mass matrix, [*C*] the damping matrix, and [*K*] the stiffness matrix of the structural element derived in terms of the nodal displacement vector *S*. The result is the external nodal force vector R^{ext} (Seotaert & Herman, 2009).The latter replaces its last component by the internal nodal force vector R^{int} given by Equation (2.3).

$$R^{int} = \sum_{h} \int_{V^h} [B]^T \sigma \, dV \tag{2.3}$$

where $[B]$ is the strain-displacement matrix of an element in use, σ is the Cauchy true stress tensor defined at a point in the material in a deformed state given in a Voigt form, see (Sippola, 2011), and V^h is the element volume, and *h* under the summation sign symbolises the summation of the entire force vector within the nodal elements. In both equations, the mass matrix, the damping matrix, and the stiffness matrix of the structure are formulated as follows:

$$[\,M] = \sum_{h} \int_{V^h} \rho^h E^{hT} E^h \, dV \tag{2.4}$$

where ρ is the density of the structure's material, E^h is the surface element displacement interpolation matrix, and h symbolises an element in process.

$$[C] = \sum_{h} \int_{V^h} [k]^h E^{hT} E^h \, dV^h \tag{2.5}$$

where [*k*] is the elemental stiffness matrix. The global stiffness matrix $[K]$is then given by:

$$[K] = \sum_{h} \int_{V^h} [B]^{hT} [C]^h B^h \, dV^h \tag{2.6}$$

where $[B]$ is the strain-displacement matrix of an element and $[C]$ is the time-dependent damping matrix (Zienkiewicz, 1967).

2.2 Direct numerical integration methods

To an extent, dynamic structures experience time-dependent changes. This process is also known as transient response. The process is numerically defined by differential equations. The numerical procedure is necessary because of the use of differential equations to analyse a dynamic structure. This leads to an explicit form of the solution, as opposed to a closed form. Therefore, the results of such numerical integration methods will be approximate.

There are two basic characteristics that the numerical integration methods can be linked to: firstly, that the differential equations are satisfied only with discrete time intervals Δt and not at all times *t*. Secondly, the derivatives of the velocity $\dot{S}$ and acceleration $\ddot{S}$ are dependent on each time interval Δt. Consequently many numerical integration methods are available depending on the type of variables preferred, such as S, $\dot{S}$ and $\ddot{S}$ at each time interval Δt. Direct numerical methods are mostly adequate for the linear dynamic analysis response of structures. This Chapter also takes into account other concepts such as single and multiple degrees of freedom of a structure.

2.3 Explicit method

In the explicit integration method, the central difference method is discussed with nodal variables such as displacement, velocity and acceleration as mentioned previously. The displacements of S_{p-1} and S_{p+1} will be analysed taking into account their time instances which varies between *p*-1 and *p*+1. As by the illustration in Figure 2.1, there are three additional displacements at a certain time instances initiated with the first time instance $p-1$, which arranging between the first and last time instances, are $S_{p+\frac{1}{2}}$, S_p and $S_{p-\frac{1}{2}}$. Therefore, in total made five displacement magnitudes. The velocity $\dot{S}$ can be found at these displacement

points. After obtaining the magnitude of velocity, the acceleration can be obtained as the second derivative $\ddot{S}$. Therefore, the magnitudes of velocity $\dot{S}$ and acceleration $\ddot{S}$ at these points of displacement can be numerically calculated while considering the change in time Δt.

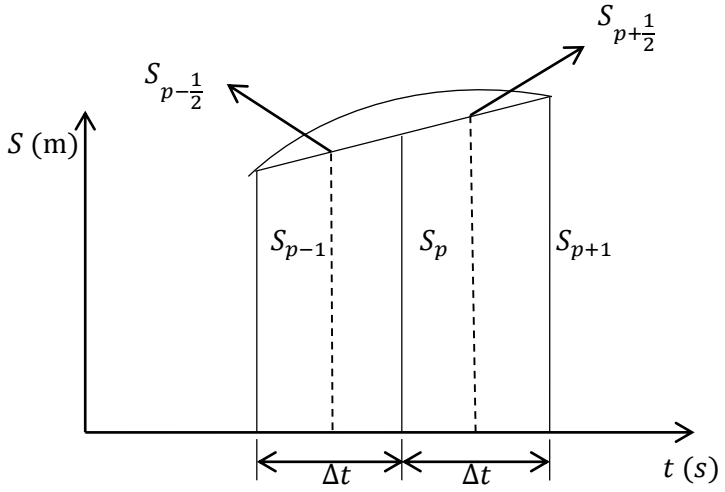

Figure 2.1: Central difference method.

The derivatives in the partial differential equation are approximated by linear combinations of function values at the displacement points (LeVeque, 2005). The method is divided into three approximation groups: forward difference, backward difference and central difference. The forward difference can be seen in Equation (2.7), backward difference in Equation (2.8) and central difference in Equation (2.9).

$$\text{Velocity: } \dot{S}_{p+\frac{1}{2}} = \frac{S_{p+1} - S_p}{\Delta t} \tag{2.7}$$

$$\dot{S}_{p-\frac{1}{2}} = \frac{S_p - S_{p-1}}{\Delta t} \tag{2.8}$$

$$\dot{S}_p = \frac{S_{p+\frac{1}{2}} - S_{p-\frac{1}{2}}}{\Delta t} \tag{2.9}$$

$$\text{Acceleration: } \ddot{S}_p = \frac{\dot{S}_{p+\frac{1}{2}} - \dot{S}_{p-\frac{1}{2}}}{\Delta t} \tag{2.10}$$

Equation (2.11) was obtained by substituting Equations (2.7) and (2.8) into Equation (2.10).

$$\ddot{S}_p = \frac{1}{(\Delta t)^2}\left(S_{p+1} - 2S_p + S_{p-1}\right) \tag{2.11}$$

The four initial equations (2.7), (2.8), (2.9) and (2.10) are not central difference (Nishant, 2003), yet explicit central difference rule is often used in solving the equations of acceleration and velocity in terms of displacement, with an advanced time which combines both continuous time *t* and discrete time Δt.

$$\dot{S}_t = \frac{1}{2\Delta t}[S_{t+\Delta t} - S_{t-\Delta t}] \tag{2.12}$$

$$\ddot{S}_t = \frac{1}{2(\Delta t)^2}[S_{t+\Delta t} - 2S_t + S_{t-\Delta t}] \tag{2.13}$$

The two last derivatives (2.12) and (2.13) are finally substituted in the dynamic Equation (2.1). Hence, the following equations are obtained:

$$[\overline{M}]\{S_{t+\Delta t}\} = \{\overline{R^{exit}}\} \tag{2.14}$$

$$[\overline{M}] = \frac{1}{(\Delta t)^2}[M] - \frac{1}{2\Delta t}[C] \tag{2.15}$$

$$\left[\overline{R^{exit}}\right] = \{R_t\} - \left([K] - \frac{2}{(\Delta t)^2}[M]\right)\{S_t\} - \left(\frac{1}{(\Delta t)^2}[M] - \frac{1}{2\Delta t}[C]\right)\{S_{t-\Delta t}\} \tag{2.16}$$

where $[M]$ is the effective mass matrix of the structure, $\overline{R^{ext}}$ is the effective external force and R^{int} the internal reaction force. When the second order ($(\Delta t)^2$) is reached, based central difference method in the explicit analysis truncation error is inevitable, which implies that the highest frequency T_{max} of the discrete structure is reached (LeVeque, 2005). The truncation error is related to the difference between the exact solution and the numerical approximation. The error depends on the step size used, the order of the method, and the problem being solved. The explicit central-difference integration is stable when the highest frequency is reached with the time step of Δt which range less than the critical time Δt_{cr} (Sippola, 2011). Finally, for the explicit central difference method to be stable, a Taylor series criterion must portray as:

$$\Delta t \leq \Delta t \leq \frac{2}{T_{max}} \tag{2.17}$$

Also, the stability and correctness of the central difference method can be described by means of the Courant criterion as:

$$\Delta \mathrm{t} \leq \frac{\Delta \mathrm{L}}{\mathrm{c}} \tag{2.18}$$

where ΔL is called the smallest distance between the nodes and c is the speed of sound. The later equation can be obtained from Young's Modulus E and the density of the material properties as:

$$c = \sqrt{\frac{E}{\rho}} \tag{2.19}$$

Equation (2.19) is not relevant unless the time increment is small compared to the required time for transferring the information between adjacent nodes of a finite element (Sippola, 2011).

2.4 Time integration method for a number of degree of freedom

The kinematic equations for a body can be derived using a central-difference method.

The velocity and displacement equations at $p + \frac{1}{2}$ and $p + 1$ are approximated as:

$$\dot{S}^N_{p+\frac{1}{2}} = \ddot{S}^N_{p-\frac{1}{2}} + \frac{\Delta t_{(p+1)} + \Delta t_{(p)}}{2} \ddot{S}^N_p \tag{2.20}$$

$$\dot{S}^N_{p+\frac{1}{2}} = \ddot{S}^N_{p-\frac{1}{2}} + \frac{\Delta t_{(p+1)} + \Delta t_{(p)}}{2} \ddot{S}^N_p \tag{2.21}$$

where superscript *N* refers to the degree of freedom in a system likened to a displacement or rotation, subscript *p* refers to the increment number, *Δt* is the time-step, and $\dot{S}$ and $\ddot{S}$ are the velocity and acceleration in the current time- step.

The use of diagonal element matrices ensures the accuracy of the explicit time-step, since the accelerations at the beginning of the increment is calculated as:

$$\ddot{S}^N_p = ([M]^N)\left(R^{ext}_p - R^{int}_p\right) \tag{2.22}$$

where $[M]$ is the mass matrix, R^{ext} is the external load vector, and R^{int} is the internal load vector. The diagonal mass matrix can be inverted to improve computational efficiency. Also

ignoring the use of the tangent stiffness matrix and iteration steps during the analysis can be the reason for the added computational efficiency. The internal load vector is determined by element contributions.

2.5 Single degree of freedom structure

In a general form, the linear dynamic response of a structure of a viscously damped single degree of freedom system is donated as:

$$[M]\ddot{S} + [C]\dot{S} + [K]S = R^{ext} \tag{2.1}$$

Equation 2.1 can be used for both single and multiple degree of freedom systems.

2.6 Multi-degree of freedom

This section of the Chapter illustrates in a global form the dynamic equations that govern the evaluation of the accelerations and displacements of the systems involving multi-degree of freedom. The multi-degrees of freedom structure process are derived from a single degree of freedom structure process (Shabana, 2012). Thus, in addition to Equation (2.1) for a single degree of freedom system, the nodal displacement vector, *S*, of a system with a number degrees of freedom, is denoted by:

$$S = [S_a \quad S_b \quad \cdots \quad S_n] \tag{2.23}$$

The mass$[M]$, damping $[C]$and stiffness $[K]$ matrices for the external nodal force vector part of the dynamic Equation (2.1) are denoted, explicitly, as:

$$[M] = \begin{bmatrix} m_{ab} & m_{ab} & \dots & m_{an} \\ m_{ab} & m_{bb} & \dots & m_{bn} \\ . & . & & . \\ . & . & & . \\ . & . & & . \\ m_{an} & m_{nb} & \dots & m_{nn} \end{bmatrix} \tag{2.24}$$

$$[C] = \begin{bmatrix} c_{ab} & c_{ab} & \dots & c_{an} \\ c_{ab} & c_{bb} & \dots & c_{bn} \\ . & . & & . \\ . & . & & . \\ . & . & & . \\ c_{an} & c_{nb} & \dots & c_{nn} \end{bmatrix} \tag{2.25}$$

$$[K] = \begin{bmatrix} k_{ab} & k_{ab} & \dots & k_{an} \\ k_{ab} & k_{bb} & \dots & k_{bn} \\ . & . & & . \\ . & . & & . \\ . & . & & . \\ k_{an} & k_{nb} & \dots & k_{nn} \end{bmatrix} \quad (2.26)$$

where m_{ij}, $C_{ij}$and $K_{ij}$and *i, j = a, b… n* etc.

The system matrices considered above is a particular case of a general n-degree-of freedom derived from a spring-mass-damper system.

2.7 Choice of explicit method over implicit method

Based on the literature survey, the advantages of ABAQUS/Explicit over Abaqus/Implicit are traced in the following steps:

- ABAQUS/Explicit is suggested for high speed and big structures problems (such as IDSC handling drop test or vehicle crash). The cost increases only linearly with problem size, but this is the case with the cost of solving the nonlinear equations associated with implicit integration, which rises more than linearly with problem size.
- The efficiency with the explicit integration method is assured as compared to the implicit integration method for solving extremely discontinuous short-time events or models (such as the IDSC handling drop test).
- Problems involving stress waves such as can be found in rock drilling, rock blasting, mining-induced seismicity, and other dynamic events can be computationally more efficient in Abaqus/Explicit than in Abaqus/Standard.

In assigning an approach to a nonlinear dynamic problem, one should consider the length of time for which the response is required compared to the stability limit of the explicit method; the size of the problem; and the restriction of the explicit method to first-order, pure displacement method or modified second-order elements. In some cases, the choice is evident, but in many problems of practical interest, the choice depends on particulars of the specific case.

2.8 The choice of the direct integral method

The stability and computational cost of the results suggest a choice between the direct integration methods. The accuracy of results requires a larger number of increments in the explicit method than the implicit method. Although the explicit method takes a large number of increments, the processing time by increment is less. The explicit analysis also needs a

smaller computational storage space compared to that of the implicit. This is because of the formation of the global stiffness matrix which is required per iteration in the implicit analysis. There are possible issues associated with the implicit type of analysis, such as contact algorithm failure and convergence, mostly in situations where a huge number of equations are to be processed. Therefore, an explicit central difference method will be used in this study.

2.9 Discretisation and choice of an element

Discretisation involves dividing the structure to be analysed into the small relevant finite elements associated with nodes and choosing the most adequate element type to model the physical behaviour of the structure. The sizing variations and selections of an element type are totally related to engineering judgment based on convergence. If the size of the element is large enough, less time is required for the computational analysis. However, a discrepancy may arise regarding the results. Therefore, the size of elements should be made small enough to produce acceptable results. The choice of an element to be used is highly dependent upon the geometry of the structure. Elements can be bars (beams or trusses), 2-D elements, or 3-D elements (plates) or solids (bricks and tetrahedral). The two elements type can be distinguishing based on the nodal degrees of freedom, every two dimensional deformable element has three degrees of freedom (two translations and one rotation). The first order 3-D solids elements were considered in this study. The brick element (C3D8R) was used on the concrete pad only. As for the rest of the components, the tetrahedral element (C3D4) was used, which fits very well with the complexity of the structure. The nodal points, which are defined by the element type, are reserved for coordinate locations to define the degrees of freedom (DOFs).

The deformation of the structure at a nodal point is dependent on the DOFs of a node, which represents the potential movements of this point due to the loading of the structure. The nodal points of a structure may have fixed displacements, and others having predetermined loads (Roylance, 2001). The DOFs also represent which forces and moments are transferred from one element to the next. The results of a finite element analysis, (deflections and stresses), are usually given at the nodes.

2.10 Mesh refinement by partitioning

There are several methods developed for partitioning. One often used is graph partitioning. In numerical simulation problems, graph partitioning in geometry refers to a group of computational problems in which the vertices of geometry have to be partitioned into various parts of large pieces while reducing the number of the edges that cross the cut. Partitioning is a convenient method to use to accomplish divide-and-conquer algorithms for a selection of

problems comprising lines (or line segments) in the plane. There are several purposes assigned for the partitioning of an element; one is that the computational cost could be minimised and the other is that the accuracy of the results could be obtained through partitioning. Furthermore, the mesh partitioning method can be assigned to a geometry, this to provide proper refinement in the regions of high stress concentrations.

2.11 Convergence method

This study will take into account a mesh convergence study on the ISDC assembly. Finite element analysis convergence defines the relationship between the number of elements or the number of degrees of freedom and the analysis accuracy. The convergence studies in most cases are associated with mesh generation methods, which is an elementary step in any simulation, yet fundamental. In finite-element stress analysis, the user should first be aware if concentrated stresses in the targeted regions are converging, and second, if they have converged to a rational level of accuracy. Therefore, convergence study is an important parameter, and should be carried out at different mesh densities in order to achieve results that are reliable when using the finite element method.

2.12 Control of discretisation error

Discretisation error is expected during the approximate numerical solution of differential equations. Discretisation error results from the fact that a finite element method is presented by a function of continuous variables, for instance, on a mesh density. Discretisation error can usually be reduced by using a more finely spaced mesh density, with an increased computational cost. In addition, numerical error plays an important role during the model validation phase. If too large, these numerical errors can yield uncertainty for the validation of the model. Furthermore, if large numerical errors are present during a model calibration step, then these errors will have propagated into the model.

2.13 Order of interpolation and Integral points

There are essentially two orders of interpolation used in the ABAQUS code. The first is linear interpolation, and the second is quadratic interpolation. The two orders of interpolation are distinguished by their nodal positions or numbers. First-order nodal points are positioned at each corner of an element only. Therefore, linear functions are assigned to interpolate across elements, resulting in less computational time. Second order elements provide mid-side nodes in addition to the corner nodes. This can be solved using quadratic interpolation, which requires more computational time.

2.14 Finite strain

In continuum mechanics finite strain theorem is used for problems containing large displacements and strains (Sippola, 2011). The method uses two different coordinates for distinguishing between the undeformed and deformed shapes. The two coordinates are labelled such as material coordinates and spatial coordinates. While infinitesimal strain theorem is a mathematical approach to determine tiny displacements and strains of a solid body (Irgens, 2008). This approach will require caution in the case of thin elastic-plastic bodies, such as rods, plates, and shells which are vulnerable to significant rotations, may cause discrepancy in results. Furthermore, with infinitesimal strain theorem is that no need for defining two coordinates respectively. This because the method shows no significant difference between the initial shape and current shape. The difference between finite strain and infinitesimal strain measures can be also based on their strain rate sensitivities.

2.15 Strain rate sensitivity

Austenitic stainless steel grade 304L and low alloy steel are used in various industries, where they are subjected to both static and dynamic loads. Based on the industrial demands, a researcher was conducted on strain rate sensitivity for various metals using both static and dynamic loads (Laubscher, 1997). The conducted research revealed that a plastic flow in metals differs as the strain rate transit from lower to the high strain rates. The study also shows low strain rates ranging from 10^{-4}/s up to 10^{0}/s, while high strain rates ranging from 10^{0}/s up to 10^{4}/s. These strain rates values are used to determine the true stress-strain curve for material input for the simulation.

2.16 True stress-true strain measure

The tensile specimen will exhibit a reduction in cross-sectional area already at the elastic stage of the test through the Poison effects. This reduction in cross-sectional area is not as remarkable as the reduction in a cross-sectional area once the material yields. This implies that the engineering stress can be used in the linear elastic region without expecting any significant error in the case of metals. Yet when the material yields, the true strain and true stress measure should be used (Roylance, 2001). These true stress-strain values are used for material input to finite element analysis.

2.17 ABAQUS finite element code

ABAQUS is a complete FE package based on the finite element procedure and includes linear analysis and nonlinear analysis. ABAQUS flows in two mathematical sequences;

ABAQUS/standard (Implicit) and ABAQUS/Explicit. This current study will be conducted using explicit analysis.

The processes of running this analysis are usually divided into three different phases: pre-processing, simulation, and post-processing. ABAQUS-CAE is a working interface process that incorporates all other possible choices relevant to the finite element analysis streams, such as generating the ABAQUS model, submitting the model to be analysed, and monitoring the jobs for correcting errors. It also provides resources to appraise the correctness of the results. In the current study, the ABAQUS-CAE could be used for the pre-processing of the multiple phases of the model, i.e. importing the SOLIDWORKS model assembly and setting the material property, defining the Step, Contact Interaction, Drop Height, Velocity and Mesh as well as creating a Job name. The Job could then be run from the explicit component after which the postprocessor results could be extracted using visualisation data, coloured in appropriate patterns.

3. MATERIAL BEHAVIOUR MODELS

3.1 Introduction

The TSC is fabricated from austenitic stainless steel grade 304L while the TC made from low alloy steel (Magnastor, 2008). These ductile materials are assumed to either behave as elastic–plastic/elastic or perfectly-plastic. Therefore, this Chapter will elaborate on the behaviours of elastic-plastic and perfectly-plastic materials. The IDSC assembly in this study is assumed to fall onto an unconfined concrete floor at a transportation stage. It is then crucial that the behaviour of unconfined concrete is added to the Chapter. This unconfined concrete is being refer to as plastic behaviour. An experimental tensile tests were conducted for duplex stainless steel 2205 at different room temperatures. Thus, the stress-strain behaviour obtained from the experimental testing will be compared to the yield stress for austenitic stainless steel grade 304L (410MPa) used in the current study at an ambient temperature of 20 degrees. The experimental steps are not explained in the current study, only the results obtained; see Figure 5.8.

3.1.1 Elastic-plastic material behaviours

Of all ductile materials, an elastic deformation is observed in the case where the deformation does not exceed their linear elastic limits σ_y. Once exceeded, plastic deformation begins until the material's ultimate stress σ_u is used, at an ultimate strain value ε_u. Refer to Figure 3.1. In homogenous linear ductile materials, the rate of deformation is dependent on the imposed load (Choung, 2008). The understanding here is derived from material mechanics theory during uniaxial tension and compression tests in order to illustrate the material's response due to an imposed load (Hibber, 2014).

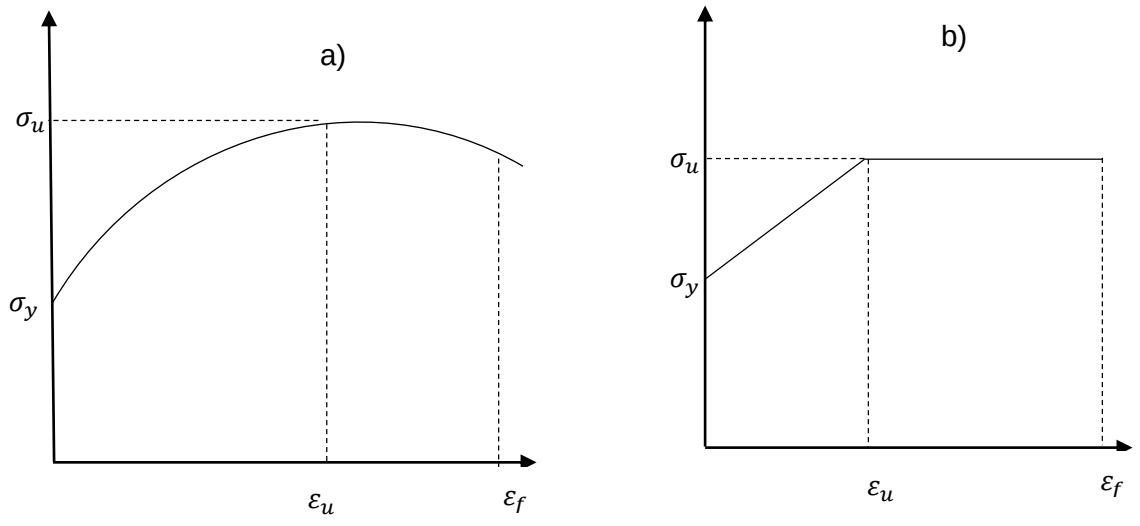

Figure 3.1: Stress –strain diagram: a) elastic–plastic and b) elastic–perfectly-plastic.

The simplified elastic–plastic and elastic–perfectly-plastic stress-strain diagrams presented in Figure 3.1 are assumed for both tensile strength and compressive strength at a material point. These graphs are essential in describing the behaviour of ductile materials initiated at the yield points. Ductile materials display plastic behaviour once the value of stress σ exceed the yield point σ_y. This phase continues until the stress reaches the ultimate strength of σ_u, at a stage neck begins to form in the specimen. The necking happens as a result of inconsistency decrease in the cross-sectional area of the tensile specimen. The necking process completed its course by the fracture ε_f of the tensile specimen. This plastic behaviour can be seen in Figure 3.1 (b). More about tensile tests can be read from (Hibber, 2014). This study will not take into consideration any failure mode, will only focussing on plastic deformation. The measures of plastic deformation will be discussed next.

3.1.2 Corresponding plastic strain

Based on Chen & Han (2007), the corresponding scalar measure of the plastic strain at a material point is given incrementally as:

$$d\varepsilon_p = \left[\frac{2}{3}(d\varepsilon^p)^T d\varepsilon^p\right]^{\frac{1}{2}} \tag{3.1}$$

where ε_p is the corresponding plastic strain at a material point. The integration of Equation (3.1) between two points on the yield surface allows the corresponding plastic strain to be obtained as follows:

$$\varepsilon_p = \int_0^t \left[\frac{2}{3}(d\varepsilon^p)^T d\varepsilon^p\right]^{\frac{1}{2}} dt \tag{3.2}$$

Equation 3.2 is obtained when integrated on the yield surface as the result of the induced stress. Therefore, the plastic strain at a current state at a material point is given as:

$$\hat{\varepsilon}_p = \left[\frac{2}{3}(\varepsilon^p)^T\ \varepsilon^p\right]^{\frac{1}{2}} \tag{3.3}$$

The restriction to this Equation 3.3 is that it can only be considered for the present state at a material point. These measures can be used to measure the monotonous plastic strain and show no difference in application (Sippola, 2011).

3.1.3 Maximum shear stress of ductile material

The theorem of maximum shear stress was presented by Tresca in 1864 after an extensive series of uniaxial tensile tests. The theorem examines the plastic flow of ductile materials through which it is stated that a ductile material does not yield plastically except when the maximum shear stress within the particle of an element matches or surpasses a critical value. After this yielding begins (Roylance, 2008, p.83). The statement is then reduced to a mathematical expression as follows:

$$\tau_{max} \geq k \tag{3.4}$$

where τ_{max} is the induced maximum shear stress in a material and k the shear yield strength of a material as the ability to handle any induced stress. The maximum shear stress of an element is obtained by using the principal stresses of a plane. These principal stresses of a plane associate their direction as well. In a general form, the maximum shear stress is denoted as:

$$\tau_{max} = \frac{\sigma_1 - \sigma_2}{2} = \frac{\sigma_0}{2} \tag{3.5}$$

where σ_1 is the maximum principal stress in a one known coordinate of the sample element and σ_2 the maximum principal stress in another known coordinate. Therefore, the shear yield strength k varies with the properties of material (Roylance, 2008, p.83).

3.1.4 Elastic-plastic yielding function for homogenous ductile materials

The tensile testing of the ductile materials shown in much research reveals that the stress at a material point does not remain uniaxial throughout a process; it rather changes to multi-axial depending on the active domain. For instance, the stress in a necking domain stress escapes its original state of being uniaxial to the multi-axial stress states. It is then important that the yielding criterion is standardised for multi-axial and expressed as a yielding function. Previously, the yielding criterion of a material was introduced in conjunction with the maximum shear stress. However, here it is introduced with a simple mathematical function (f) known as yielding function and shown with some material dependent variables as:

$$f(\sigma_{0,}\ I_1, I_2\ , \ldots) \leq 0 \tag{3.6}$$

where σ_0 is the stress vector varying with all the magnitudes and natures of principal stresses of a prism planes and I_i are invariants components of the chosen coordinates system. This criterion is brought to completion in an active material state when $f > 0$ yielding occurs and

yielding is not present when the state of a material portrays a pattern of $f \leq 0$. Thus the latter shows that the material is in the elastic state (Sippola, 2011, p.25).

3.1.5 Von Mises yield criterion and yield function

Based on failure theorem of an isotropic ductile material, the state of stresses at a point can be expressed with principle stresses. These principle stresses are relative of their coordinated vectors such as b_i , where $\mathrm{i} = 1, 2, 3$ in a space (3D) pattern. The theorem also provides that, the properties of materials are invariants in all coordinates. Therefore, the principal stresses of an isotropic are also independent of the chosen coordinate system. The theorem used to determine the principles stresses of an isotropic ductile material is referred to as a von Mises yield criterion. The von Mises Yield criterion is given as follows:

$$\sigma_{VM} = \sqrt{\frac{(\sigma_1 - \sigma_2)^2 + (\sigma_1 - \sigma_3)^2 + (\sigma_2 - \sigma_3)^2}{2}} \tag{3.7}$$

where σ_{VM} is the von Mises Stress and $\sigma_{1,}\, \sigma_2$ and σ_3 are the principal stresses of a homogenous ductile material on their respective chosen coordinates. After several uniaxial tensile tests were conducted, a conclusion was drawn that a ductile material does not yield unless the one of the stress components of a specimen reaches $\sigma_1 = \sigma_{YS}$, where $\sigma_2 = \sigma_3 = 0$ then von Mises Yielding criterion can be rewritten as:

$$\sigma_{VM} = \sqrt{\frac{(\sigma_{YS} - 0)^2 + (\sigma_{YS} - 0)^2 + (0 - 0)^2}{2}} = \sqrt{\frac{2\sigma_{YS}^2}{2}} = \sigma_{YS} \tag{3.8}$$

where σ_{YS} is the yielding strength of a material. It is compared with the von Mises Yield criterion to determine the state of a material at a point. The expression of the yielding criterion of an isotropic ductile material could be reduced to the simplest form called yield function (f) the reduced equation is defined in terms of principal stresses and k is the shear yield strength of a material defined as:

$$f = (\sigma_1 - \sigma_2)^2 - (\sigma_1 - \sigma_3)^2 - (\sigma_2 - \sigma_3)^2 - 6\tau^2 \tag{3.9}$$

The shear yield strength of a material (τ) can be easily calculated by means of the yield strength σ_{YS} of a material. This stands true in terms of the assumption made in the theory on the von Mises criterion which states that the hydrostatic stress component has no effect on

the yield criterion of a material point (Sippola, 2011, p.24). Therefore, the magnitude of the shear yield strength of a material can be obtained by

$$\tau = \frac{\sigma_{YS}}{\sqrt{3}} \tag{3.10}$$

3.1.6 Flow rules for ductile materials

As soon as the material goes into the plastic deformation, the components of the plastic strain increment may be defined by

$$d\varepsilon^p = ds\frac{\partial Z}{\partial \sigma_i} \tag{3.11}$$

where ds is a positive proportionality constant, dependent with the hardening rule for elasto-plastic material, and Z is the plastic potential function (Prasad, 2018, p.46). The flow rule of an elasto-plastic material is divided into two categories. One called associated flow rule and the other considered as non-associated flow rule. The flow rule is said to be associated, when $Z = f$ in Equation (3.11). Therefore, Equation (3.11) at an initial state is said to be a non-associated flow rule. The associated flow rule equation can be obtained once substituting f instead of Z in Equation (3.11). The form of flow rule obtained after substitution is shown in Equation (3.12),

$$d\varepsilon^p = ds\frac{\partial f}{\partial \sigma_i} \tag{3.12}$$

Here, ds is a non-negative hardening parameter in an increment form in oder to determine the magnitude of the plastic strain. The associated flow rule method endorsed that the direction of plastic strain increment to be normal to the yield surface. This is why the associated flow rule is also called as normality of hypothesis of plasticity. The plastic strain increment is given in a following form:

$$\frac{\partial f}{\partial \sigma_i} \tag{3.13}$$

The flow rule process as well defines a process that illustrates the absence of the plastic straining as $ds = 0$ if $f \leq 0$ (Sippola, 2011, p.25).

3.1.7 Hardening rules

The hardening rules are characterised in two ways, one being an isotropic hardening rule and the other a kinematic hardening rule. Refer to Figure 3.2.

A general-purpose hardening rule illustrates that a continuous increase in stress is very crucial once yield occurs. This may be conducted in order to encourage plastic deformation on the yield surface.

For an isotropic hardening rule, no complexity was found using the hardening rule: it is user friendly. The rule flows adequately in an isotropic material with repetitious loading. But it is not to be used when the loading direction changes (Sippola, 2011, p.27).

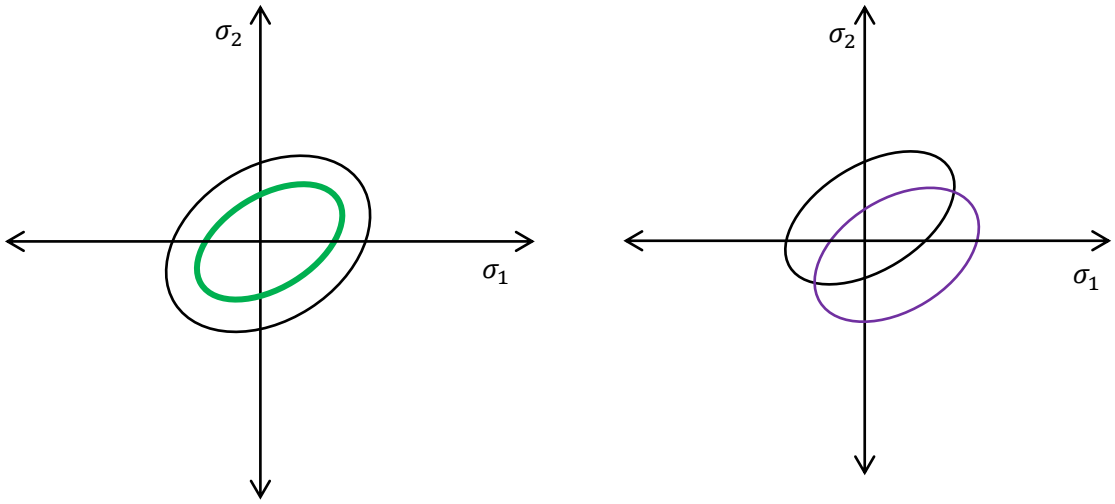

Figure 3.2: Isotropic hardening rule (left) and Kinematic hardening rule (right)

The application of an isotropic hardening rule on the von Mises yield surface is illustrated in Figure 3.2, which is the cut plane of the yield surface of the specimen. The cut plane is radial on a von Mises yield surface and the axis of representation follow the pattern of the Cartesian coordinates, where $\sigma_1 = \sigma_2 = \sigma_3$ increases homogeneously without changing the shape size of the yield surface. An isotropic hardening rule can be expressed in a form of the yield function as follows:

$$f(\sigma_i, \sigma_{YS}) = 0 \tag{3.12}$$

The configuration of the yield function is quantified by the preliminary yield function and its actual size changes as the hardening parameter σ_{YS} changes. The change of the hardening parameter σ_{YS} is dependent on the corresponding plastic strain (ε_p) mentioned previously in Equation (3.2) and given in an equation form as:

$$\sigma_{YS} = \sigma_{VM}(\varepsilon_p) \tag{3.13}$$

The understanding here is a derivitive of the uniaxial tensile test in the plastic domain. This plastic domain is a reflection of the total applied stress (σ_i) versus the plastic strain (ε^p). In order to obtained the plastic domain the uniaxial tensile test is arranged such that it could be obtained from the process curve ($\sigma_i \varepsilon$) using the Hooke's law (3.14) together with additive strain decomposition (3.15), the method was made possible by setting $\sigma_i = \sigma_{VM}$ as well as $\varepsilon^p = \varepsilon_p$. The kinematic harding rule comes into being once the loading direction changes.

$$\sigma_i = E \times \varepsilon \tag{3.14}$$

$$d\varepsilon = d\varepsilon^e + d\varepsilon^p \tag{3.15}$$

The method was achieved by reducing the absolute compressive yield stress value while enhancing that of the tensile yield stress by the hardening rule. The process was taken into account as that for the Bauschinger effect to enable the translation of the yield surface to a rigid body. Figure 3.2 shows an illustration of the kinematic hardening on von Mises yield surface. The method could also be given in a form yield function as:

$$f(\sigma_i - \alpha) = 0 \tag{3.16}$$

where α is the back-stress of which physical value is dependent of the plastic strain. The increment of the back-stress can be obtained using Ziegler's hardening rule mostly for merely linear work hardening. This increment of back-stress is given as follows:

$$d\alpha = E_p \frac{1}{\sigma_{YS}} (\sigma_i - \alpha)\, d\varepsilon_p \tag{3.17}$$

The part in bracket $(\sigma_i - \alpha)$ shows the direction on which the increment of back-stress depends, called a reduced stress vector, and E_p accounted for plastic modulus. These two hardening rules can be used simultaneously. Owing to this fact the two terms could be reduced into a single term known as mixed hardening (Sippola, 2011, p.28).

3.1.8 Stresses in a finite element

The stresses of an element are frequently calculated at the integration points. These points ensure the closest accuracy of the results, and later the method is made available for calculating the stresses at the nodal points of an element (Seshu, 2012, p.3). In a case of minor displacement analyses the nodal points of an element are of great value to obtain the

strain state at the material point to determine stresses. The total nodal displacement is given as follows:

$$\varepsilon = [B]u \tag{3.18}$$

where $[B]$ is the displacement-matrix and u is the nodal displacement of the element. In a general concept, the train increment $\Delta\varepsilon$ can be obtained of the polar decomposition gradient and during the increment, the approximate rotation of the principal axes is permitted where necessary (Seshu, 2012 ,p 92).

In finite element analysis the use of the decomposition of the deformation gradients is distinguished by variations with a range of elastic and plastic deformations. Regarding the study by Seshu (2003), once higher ranges of elastic and plastic strains are expected, it should then be associated with a multiplicative decomposition of the deformation gradient (Sippola, 2011). But for lower ranges of the elastic and plastic strains or negligible plastic strain, a simplified decomposition method such as the one of Equation (3.15), called additive, should be used.

3.1.9 Stresses in a linear elastic section

Stresses at a material point, when observed linear elastic state can be calculated by the relationship between stresses and strains. The relations can be expressed in Cartesian coordinates (*xyz*) using a generalized Hook's equation (3.19). This may be defined in a matrix form as follows:

$$\sigma_i = [D]\varepsilon \tag{3.19}$$

where $[D]$ is taken for the elasticity matrix. For an isotropic material, this equation can be repeated as follows:

$$\begin{Bmatrix} \sigma_x \\ \sigma_y \\ \sigma_z \\ \tau_{xy} \\ \tau_{yz} \\ \tau_{xz} \end{Bmatrix} = \begin{Bmatrix} 1-\upsilon & \upsilon & \upsilon & 0 & 0 & 0 \\ \upsilon & 1-\upsilon & \upsilon & 0 & 0 & 0 \\ \upsilon & \upsilon & 1-\upsilon & 0 & 0 & 0 \\ 0 & 0 & 0 & \frac{1}{2}-\upsilon & \frac{1}{2}-\upsilon & 0 \\ 0 & 0 & 0 & 0 & 0 & 0 \\ 0 & 0 & 0 & 0 & 0 & \frac{1}{2}-\upsilon \end{Bmatrix} = \begin{Bmatrix} \varepsilon_x \\ \varepsilon_y \\ \varepsilon_z \\ \gamma_{xz} \\ \gamma_{yz} \\ \gamma_{xz} \end{Bmatrix} \tag{3.20}$$

where *Q* stands for the constant of the elasticity matrix and can be given as follows:

$$Q = \frac{E}{(1+v)(1-2v)} \tag{3.21}$$

in which *E* is the elastic modulus of the material and v is the Poison's ratio.

3.1.10 Stress Increment–Strain Increment Relation in the Plastic Region

Elastic-plastic finite element problems have a nonlinear stress-strain relation. This induced nonlinear behaviour can be controlled by Newton–Raphson iterations in conjunction with the implicit Euler method. The total strain increment can be estimated as:

$$d\varepsilon_{p+1} = d\varepsilon^{e}_{p+1} + d\varepsilon^{p}_{p+1} \tag{3.22}$$

The equation above is expressed by considering a time step. The time step changes from an initial state of p to an advanced state as $(p+1)$ during the yielding at a material point. The elastic increment strain can be given incrementally in a term of the time step as:

$$d\varepsilon^{e}_{p+1} = [D]^{-1} d\sigma_{i(p+1)} \tag{3.23}$$

where $d\sigma_{i(p+1)}$ is stress increment and for plastic is given by associated flow rule,

$$d\varepsilon^{p}_{p+1} = \left(ds\frac{\partial Z}{\partial X}\right)_{p+1} \tag{3.24}$$

in this instance, $\mathrm{d}s$ is observed as an increment of a scalar also called plastic multiplier through which the plastic strain of an elastoplastic material is defined and *Z* regarded for plastic potential function. The flow rule is said to be associated where the von Mises yield function is considered, which brings about a relationship of plastic potential function and yield function as $Z = f$. This assumption is sealed when $ds > 0$ while $f = 0$. See section 3.1.5; it explains flow rules for elastoplastic material. At a stage, the total increment strain can be expressed in a differential equation form:

$$d\varepsilon_{p+1} = [D]^{-1} d\sigma_{i(p+1)} + \left(ds\frac{\partial Z}{\partial X}\right)_{p+1} \tag{3.25}$$

Here it is crucial that the residual equation is developed before developing the New-Rhapson iteration that can be used at each time step. The residual equation in a context here can be defined using equation (3.25) in a power order of b^{th} iteration as:

$$Q^{-b} = [D]^{-1} d\sigma_{i(p+1)}^{b} + \left(ds \frac{\partial Z}{\partial X}\right)_{p+1}^{b} + d\varepsilon_{p+1}^{b} \tag{3.26}$$

where Q^{-b} is called the residual vector at the b^{th} iteration. Further, the state of a material point that illustrates yielding of a material is beginning $(f = 0)$ can be expressed in terms of time step as:

$$f_{(p+1)} = 0 \tag{3.27}$$

Therefore, in a matrix form the New-Raphson iteration can be obtained by derivatives of the two Equations of (3.26) and (3.27) which gives:

$$-\begin{bmatrix} Q^{-b} \\ f^{b} \end{bmatrix} = \begin{bmatrix} \Delta\sigma^{b} \\ \Delta s^{b} \end{bmatrix} \begin{bmatrix} [D]^{-1} + \dfrac{\partial^2 f}{\partial \sigma_i^2} & \dfrac{\partial f}{\partial \sigma_i} \\ \dfrac{\partial f^T}{\partial \sigma_i} & -E_p \end{bmatrix}_{p+1}^{b} \tag{3.28}$$

where E_p is called the modulus of plasticity, Δs^{b}stands for the interactive increment strain at a step time and $\Delta\sigma^{b}$ known as the interactive increment stress of a time step. The iteration above (3.28) is arranged in such way that at the start the process should begin by an assumption that:

$$\varepsilon_{p+1}^{p} = \varepsilon_p \text{ or } \Delta\varepsilon_{p+1}^{b} = \Delta\varepsilon_p \tag{3.29}$$

This assumption is true unless an initial iteration is taken as zero. Therefore, the initial states of the iteration are given as:

$$ds^{b+1} = ds^{b} + \Delta s^{b} \ , ds^{0} = 0 \tag{3.30}$$

$$d\sigma_{i(p+1)}^{b+1} = d\sigma_{i(p+1)}^{b} + \Delta\sigma^{b} \ , \ d\sigma_{i(p+1)}^{0} = 0 \tag{3.31}$$

On complete of the b^{th} iterations, the change in the theoretical values of the stresses and plastic strains are obtained by

$$\varepsilon_{p+1}^{p} = \varepsilon_{p}^{p} + [D]^{-1} d\sigma_{(p+1)} \tag{3.32}$$

$$\sigma_{i(p+1)} = \sigma_{ip} + d\sigma_{(p+1)} \tag{3.33}$$

3.2 Plastic material behaviour

The floor on which the IDSC system is anticipated to be falling onto, is a reinforced concrete floor as previously introduced. This is based on nuclear regulations as given in Magnastor, 2008. However, the floor throughout this study is assumed to be plain concrete (unconfined concrete) in behaviours. The assumption was adopted after several researches and industrial consultations were conducted. There are few reasons aligned with the assumption made; one is that during the casting of concrete the reinforcement bars are placed at the bottom to carry tensile forces (Gu, 2016). The other reason is based on plasticity input in the Abaqus code.

The crushing of concrete in compression and the cracking of the concrete in tension are the two common failure modes of unconfined concrete. The behaviour of unconfined concrete is been introduced in several researches using constitutive model, called concrete damage plasticity (CDP) model (Carol, et al., 2001). It was found necessary by the researchers to have a simplified model of CDP due to a degree of complexity of the CDP theory, so a simplified concrete damage plasticity (SCDP) model was developed.

The SCDP model was prepared in tabular forms to simulate the behaviour of unconfined concrete. The parameters taken into account, included a damage parameter, and strain hardening/softening rules, as well as other elements. The results were tabulated using different concrete grades (B20, B30, B40 and B50), as shown in Table 5.4. The behaviours of the B50 concrete grade in all the aspects relatively to the effective application in a finite element method were presented. The presented data in Table 5.4 will be use as the input variables for concrete floor.

The variables were presented in the pattern of hardening and softening variables. The loss of elastic stiffness and the development of the yield surface in concrete materials are based on their responses to compressive and tensile load variables. Numerically these variables are characterized separately by two hardening strain variables, (ε_c^{pl}) and (ε_t^{pl}) known as equivalent plastic strains in compressive and tensile mediums consecutively. Their values are obtained using uniaxial compressive and tensile tests. Their formulae were derived using isotropic hardening variables such as an inelastic compression crushing strain (ε_c^{in}) and tensile cracking strain (ε_t^{ck}), and are given as follows,

$$\varepsilon_c^{pl} = \varepsilon_c^{in} - \left[\left(\frac{d_c}{1-d_c}\right) \times \left(\frac{\sigma_c}{E_0}\right)\right] \tag{3.34}$$

$$\varepsilon_t^{pl} = \varepsilon_t^{ck} - \left[\left(\frac{d_t}{1-d_t}\right) \times \left(\frac{\sigma_t}{E_0}\right)\right] \tag{3.35}$$

where E_o is the young's modulus at a material point. d_c and d_t are two scalar variables at a damage point, and once reached 1 unit (completely damage). The magnitudes of compressive σ_c and tensile σ_t strengths of concrete are expressed as follows,

$$\sigma_c = (1-d_c)E_0\left(\varepsilon_c - \varepsilon_c^{pl}\right) \tag{3.36}$$

$$\sigma_c = \sigma_{cu}\left[2\left(\frac{\varepsilon_c}{\varepsilon_c'}\right) - \left(\frac{\varepsilon_c}{\varepsilon_c'}\right)\right] \tag{3.37}$$

$$\sigma_t = (1-d_t)E_0\left(\varepsilon_t - \varepsilon_t^{pl}\right) \tag{3.38}$$

These formulations are used to obtain variables that will later be input data to the ABAQUS finite element analysis (Milad, et al., 2017).

3.2.1 Failure energy absorption by the concrete floor

The anticipated damage to the concrete floor during the drop incident of the IDSC, has been studied using local failure mode. One of the reasons is that local failure mode (LFM) to the IDSC is dependent on LFM of the concrete floor. The local LFM to the concrete floor has been studied using the method of the penetration depth. This penetration depth study is based on conservation of energy method as per previous studies conducted on the topic (Hyeon, et al., 2017). The method taking into account the energy absorptions on both IDSC and concrete floor. The conservation of energy equation is given as follows:

$$E_K = E_R \tag{3.39}$$

where E_K is the kinetic energy of the IDSC ; E_R is the resistance energy of a reinforced concrete floor. The thermal energy and sound energy after the impact are neglected. Note that only the material models dependent upon the strain rate, size effect factor and nose shape-factor of an IDSC as well as the spalled concrete failure cone are adopted from the existing studies. The magnitudes of kinetic and resistance energies are given by:

$$E_K = \frac{m(V_o^2 - V_r^2)}{2} \tag{3.40}$$

where V_0 is the original velocity of the IDSC; V_r is the residual velocity of the IDSC after impact, and:

$$E_R = E_{DM} + E_{DC} + E_S + E_T + E_C \tag{3.41}$$

The constituents of the resistant energy (E_R) are labelled as follows: a) E_{DM} the deformed energy of the metallic cask (IDSC); b) E_{DC} the deformed energy of the concrete; c) E_S spalling-resistant energy; d) E_T tunnelling (perforation)-resistant energy; and e) E_C scabbing-resistant energy. Each of these constituents can be obtained as by the formulations made available, refer to the work conducted by (Károlyi, 2016), see Figure 3.2. However, shape parameters of the IDSC and concrete positioning require no incorporation of the last two forms of energies that are tunnelling-resistant energy and scabbing-resistant. These forms of energies could have been considered only if the concrete floor was horizontally suspended. More details are available, refer to (Hyeon, et al., 2017).

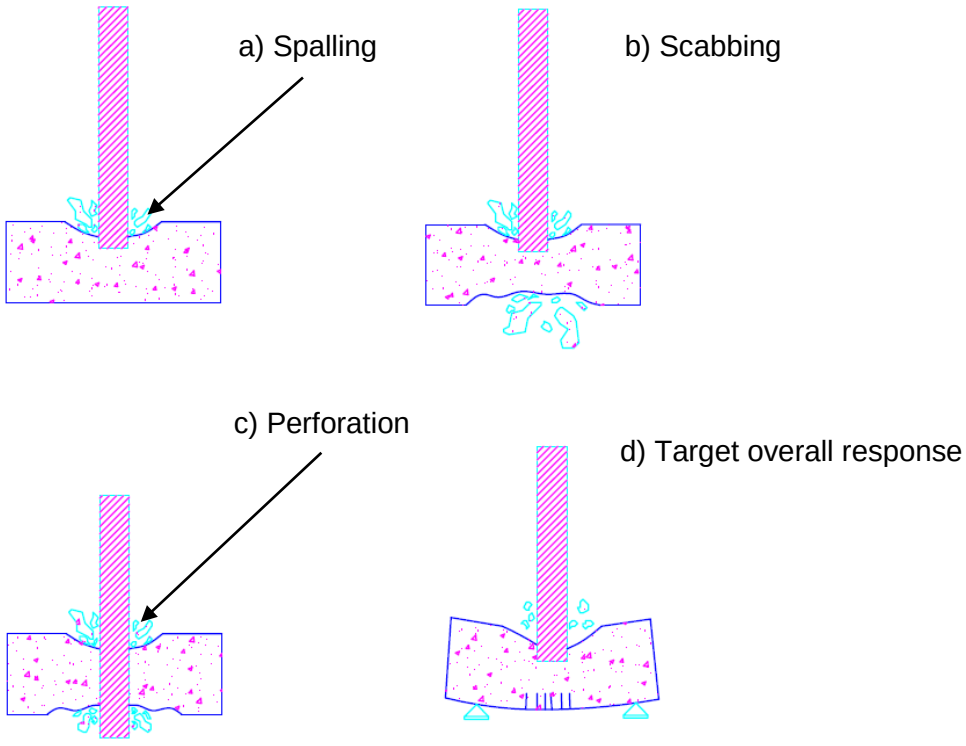

Figure 3.3: Failure mode of concrete floor subjected to impact load

Figure 3.3 illustrates local failure conditions caused by the handling drop impact. The illustrations are velocities dependent at a point, the handling drop impact necessitates the use

of spalling energy because of no change in impact velocity. This is not the case with missiles impact, with low velocities rebound from the target creating negligible or no local damage on the target. Figure 3.3 (a) illustrates spalling energy to be expected during the increase in impact velocities, in both the handling drop of IDSC and the missile spalling energy which forms a spalling crater on the contact face of the target may be anticipated. As the velocity increases, the expectation on handling drop is slightly different compared with that of the missile. The penetration depth increases and eventually cracking starts at the back of the target which results in scabbing of the concrete as shown in Figure 3.3 (b). This stands true based on the shape factor at the end face of the missile and its velocity. The penetration depth is higher compared to the handling drop. Also, with the two last conditions in Figure 3.3 (c) and (d) are for missile with higher velocities, the missile perforates through the concrete target. The condition (d) may be taken into consideration for the concrete floor in a case of it being suspended horizontally as mentioned earlier.

3.2.2 Penetration depth determination

The penetration depth prediction method was originally developed based on the test data of plain concrete as mentioned above. Therefore, no effects from steel fibers, reinforcing bars, or cask hardness on the penetration depth are considered. The method takes into account impact velocity in conjunction with other parameters such as the weight of the IDSC, compressive strength of concrete and contact surface at the end of the IDSC. The contact surface will be referred to as an end-shape function. The end-shape function should be determined before estimating the penetration depth (X_d). The end-shape function can be understood with an arrangement such as (N=0.72 for flat nose, 0.84 for hemispherical, 1.0 for a blunt nose, and 1.13 for a sharp nose (Hyeon, et al., 2017). All the necessary parameters are obtained, thus the penetration depth (X_d) of concrete can be given as follows.

$$X_d = 2d\sqrt{G} \text{ if } G \leq 1 \tag{3.42}$$

$$X_d = (G+1)d \quad \text{if } G > 1 \tag{3.43}$$

$$G = 3.8 \times 10^{-5} \frac{Nm}{d\sqrt{f_c'}} \left(\frac{V_o}{d}\right)^{1.8} \quad (\text{in kg, Pa}, m/s, \text{and m}) \tag{3.44}$$

where *m* is the shape mass, *d* is the contact diameter, V_0 is the initial velocity and *fc'* is the concrete compressive strength. The end–shape function (N) will be considered as that for a flat nose (0.72). Based on the details available for the IDSC which include the total mass

(107300kg), Nose function (0.72), ending shape diameter (2.54 m) and concrete compressive strength (50MPa). The penetration depth can be estimated as follows;

$$G = 3.8 \times 10^{-5} \frac{0.72 \times 107300}{2.54\sqrt{50000000}} \left(\frac{13.29}{2.54}\right)^{1.8} = \quad 0.0032$$

$$\mathrm{X_d} = 2d\sqrt{G} = 2 \times 2.54\sqrt{0.0032} = 0.287\, m$$

After establishing the magnitude ($0.287\, m$) of penetration depth expected during the impact, the energy absorbed by the concrete floor can be determined using the kinetic energy or potential energy formula.

4. CONTACT BETWEEN PARTS GEOMETRIES OF IDSC

4.1 Introduction

In solid mechanics or continuum mechanics, contact in a general description is referred to as interactions between part geometries of an assembly. The interactions of two objects in contact should be detected during the simulation. This should be conducted to avoid nodal penetrations between the two objects. The contact between two objects can either be defined as rigid (master) to deformable (slave) or deformable to deformable. In the case of the IDSC analysis, both rigid-to-deformable and deformable-to-deformable contacts are important. The details regarding these contacts are discussed in this Chapter.

4.1.1 Contact interaction

During the dynamic simulations of the IDSC, it was crucial to assign contact interactions between two different objects. These contact interactions should be well-defined for each contact surface to improve the results of the analyses. In ABAQUS finite element code, in terms of master and slave surfaces, the contacts are adequately defined.

A rigid surface is observed as a master contact in contact with a deformable slave surface. Whenever the master surface is element-based, it is defined by the surfaces connecting the nodes of the elements. With regards to the slave surface, it is not taken as a set of nodes unless the node-to-surface discretisation method is considered. Surface contact is not detected except when the slave surface nodes penetrate the master surface. However, the master surface nodes can penetrate the imaginary slave surface nodes without a surface contact being detected, as shown in Figure 4.1.

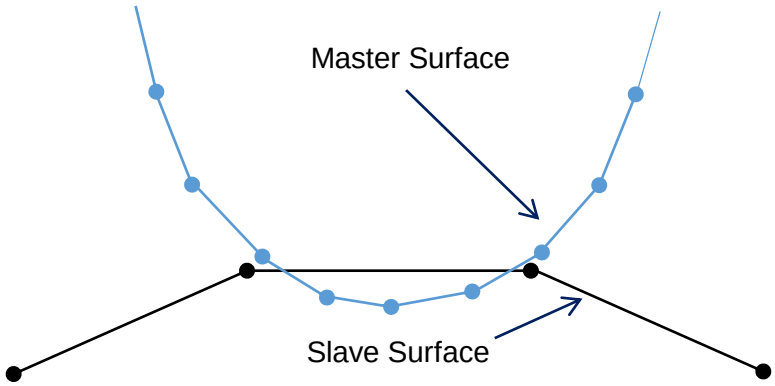

Figure 4.1: Detected penetrations of master nodes

Figure 4.1 illustrates the master surface node penetrating the slave surface but not the slave surface nodes. The contact errors could be avoided by considering the followings steps when selecting the slave and the master surfaces and contact discretisation:

- Node-based surface considered as slave surface
- Slave surfaces being aligned to deformable bodies
- Rigid surface stands for master surface
- Smaller surfaces assigned to slave surfaces
- All slave surfaces aligned with a finer mesh rather than master surfaces
- Surfaces are selected based on materials and geometric capabilities, such that any harder component materially and geometrically is considered for master surface.

With regards to contact discretisation, implicit simulations are restricted only to the use of node-to-surface or surface-to-surface discretisation, whereas explicit simulations are associated with node-to-face discretisation. In addition to the three discretisation methods, another is called edge-to-edge discretisation. This can be used for either implicit or explicit analysis (Sippola, 2011, p.19).

4.1.2 Contact surface discretisation

As mentioned earlier, the above discretisation techniques differ based on the type of analysis in motion. For example, node-to-surface discretisation is formulated for ABAQUS/Explicit and surface-to-surface works in conjunction with ABAQUS/Implicit in which the slave surface is the most considered shape.

In finite element simulations, the domains near the slave nodes are most useful in determining the average integral contact conditions. The averaging integral domains are approximately centred at the slave nodes. This accommodates the consideration of the adjacent slave nodes in the determination of the contact constraints. The starting contact direction required is defined by an average point perpendicular to the slave surface in the domain enclosed by the slave node. It is worthwhile to depend on the surface-to-surface discretisation as compared to the node-to-surface discretisation, as it guarantees smoother and improved results at contact pressures and stresses. Further, the large possibilities of surface penetrations are diminished by master-slave surface contact. However, in the case of comparable mesh densities, it is much more desirable to use node-to-surface instead of surface-to-surface discretisation on the partitioning of the master-slave surface. The results of the two discretisation techniques give another perspective. This perspective is that the results can only change significantly with the use of coarse mesh and not with fine mesh. Different illustrations are made available

below, in which contact discretisation comparisons between ABAQUS/Explicit and ABAQUS/Implicit are demonstrated:

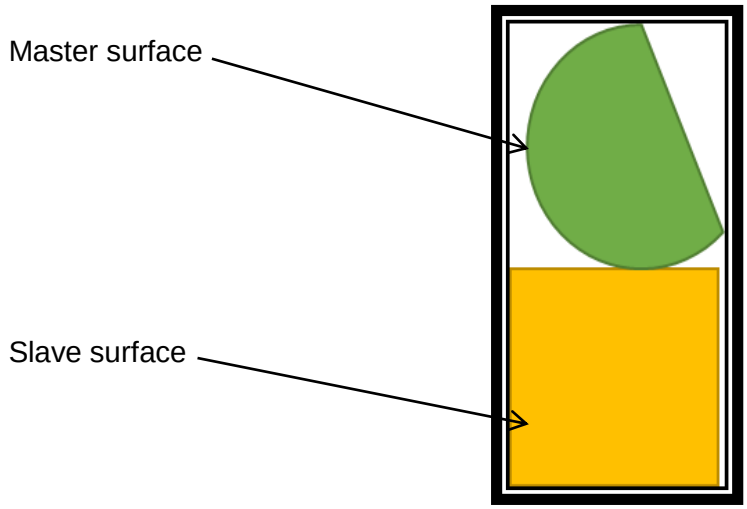

Figure 4.2: Undetected penetrations of master nodes into the slave surfaces

This means no penetration occurs in both surface-to-surface if used in ABAQUS/Explicit and node-to-surface when used in ABAQUS/Implicit.

Note that based on the ABAQUS code, the surface-to-surface approach is used by default in ABAQUS/Implicit with exceptions, while it is optional in ABAQUS/Explicit. Owing to the case of unlimited acoustic elements tied to shell elements in ABAQUS/Implicit, the use of the surface-to-surface approach significantly adds to the computational cost. Therefore, the node-to-surface approach is used by default in this context (Anon, 2013).

4.1.3 Contact surface weighting techniques

There are two contact surface weighting techniques in which surface contacts are defined in the ABAQUS code, the first being once contact weighting and the second being twice contact weighting. The basic idea was introduced formerly on the master-slave algorithm. The idea was purely master-slave, also known as once contact weighting. This implies that contact interactions are carried out once, as selected, and on the other hand for exaggerating coarse mesh elements. Only master surface nodes could penetrate the slave nodes without any contact resistance as previously shown in Figure 4.1.

The second technique is an alternative known as balanced master-slave, in which each contact surface is selected twice to avoid element penetrations. The second technique is achieved by swapping the master-slave arrangement, which is contrary to the first contact surfaces selected (Sippola, 2011). The average result of the two techniques will then be the

closing contact arrangement. Although it has been understood that the balanced technique minimises surface penetrations, there is still the issue of computational cost, as the computational process is carried out twice. It is advised that, while dealing with two deformable bodies that are touching each other, the balanced master-slave technique should be used.

Therefore, it is better to use the explicit element analysis code rather than implicit element analysis, as unnecessary over-constrained issues may occur. Therefore, pure master-slave is more appropriate (Dassault Systèmes, 2014).

4.1.4 Contact constrained optimisation

The equilibrium equation of motion requires an increase in parameters of consideration due to the contact detected constraints. Thus, a proper understanding of constraint methods for the detected contact conditions is vital while running a computational finite element simulation. The two constraint methods that can be used for defining the surfaces detected and their contact forces applicable in the ABAQUS program are the Lagrange multiplier method and the penalty method, as illustrated in Figure 4.3.

Both the Langrage multiplier and the penalty method consist of a supported spring mass (*m*) with stiffness (*k*) attached to the top support. The bottom surfaces, however, are made rigid. The first configuration (x_1) shows the suspended mass moving towards the bottom with an acceleration field of *g* magnitude. The change in height of oscillation from its origin to the bottom base, considered as (*Y*), is much clearer as the final height is reached shown in the second shape (x_2).

Therefore the contact is detected at a point where $Y \leq 0$ and for this reason the nonlinearity of boundary conditions becomes a vital concern. So an assumption is made on contact constraint, since the contact has been detected as $Y \leq 0, mg \geq kY$ (Sippola, 2011).

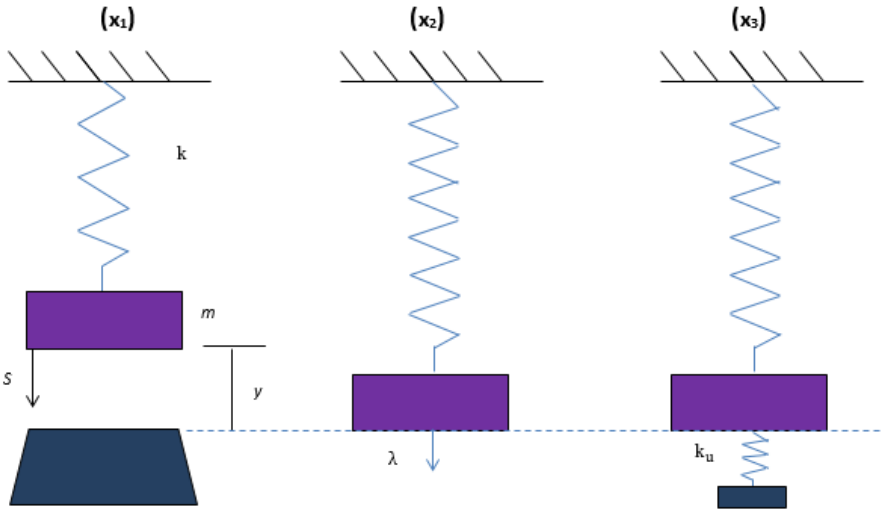

Figure 4.3: One dimensional finite element surface contact illustration

The Lagrange multiplier method is normally used in the equilibrium equation of motion for contact constrained optimisation. The Lagrange multiplier method proceeds by treating (λ) as unknown and solving Equations (4.1) and (4.2),

$$ks + \lambda = mg \tag{4.1}$$

$$s + 0 = Y \tag{4.2}$$

The two equations developed here are used to solve for the Lagrange multiplier (λ). Therefore, the Lagrange multiplier can be obtained by:

$$\lambda = mg - ks \tag{4.3}$$

The last method, namely the penalty method, can be formulated from the illustration (x_3) in which a reasonable spring is added to induce a penalty stiffness (k_u). The term "reasonable" that is used here simply means that once the magnitude of k_u is too small or too big, a degree of converging difficulties should be expected. However, in the case of it being too small, a provision has been made that the augmented Lagrange method can be used, though the computational cost may increase. The method is similar to that of the Lagrange method, but with penalty variables associated. Refer to (Sippola, 2011) for clarity on the augmented Lagrange method. Initially the equilibrium equation of the penalty method is given as follows:

$$(k + k_u)s = mg \tag{4.4}$$

The only limitation found with the augmented Lagrange method is that though improved, the converging rate cannot intervene successfully with problems of multi-dimensional contact constraints of deformable bodies during the process increment. The discrepancy raised here can be adjusted by considering independently that the parameters which were added on the equation of equilibrium contact constraints were added to both explicit and implicit analyses (Sippola, 2011).

4.1.5 Explicit contact constraint method

This section is dedicated to explicit finite element analysis. The contact constraint, in the explicit form of analysis, is arranged such that the penalty method could easily or directly be implemented in the equilibrium Equation (2.1) to improve contact constraints. The penalty method for a dynamic system is illustrated by the minimum energy conservation principle by taking into account the residual vector ($\bar{Q}$), previously mentioned in Chapter 3, as well as the contact constraint contribution matrix $[C^b]^T$. This can be obtained using partial derivatives in terms of the contribution matrix. Refer to Equation (4.7) (Sippola, 2011). Therefore, the penalty method can be obtained as follows:

$$\bar{Q} + k_u[C^b]^T[Q^b] = 0 \tag{4.5}$$

$$\bar{Q} = -k_u[C^b]^T[Q^b] \tag{4.6}$$

$$[C^b] = \frac{\partial[Q^b]}{\partial S} \tag{4.7}$$

At this stage the contact constraint method can be added in the equilibrium Equation (2.1) in the form of a residual vector to define the nodal acceleration in terms of displacement, velocity, applied force, and internal force as follows:

$$\ddot{S} = [M]^{-1}\left(R_p^{exit} + \bar{Q} - [S]\dot{S}_{p-\frac{1}{2}} - R_p^{int}\right) \tag{4.8}$$

or:

$$\ddot{S} = [M]^{-1}\left(R_p^{exit} - k_u[C^b]^T[Q^b] - [S]\dot{S}_{p-\frac{1}{2}} - R_p^{int}\right) \tag{4.9}$$

For all constraints, the penalty stiffness is adopted similarly throughout the process. The implementation of the Lagrange multiplier method in the explicit analysis is not as easy as the penalty method, as it requires other point considerations which comprise predictor and

corrector type of algorithms to encourage the contact constraints adequately. The Lagrange multiplier method which can be added to the equation is obtained as well, by associating the minimum conservation principle that permits the residual vector ($\bar{Q}$) with the contact constraint contribution matrix $[C^b]^T$ to be used. This gives:

$$\bar{Q} = -[C^b]^T \Lambda \tag{4.10}$$

where Λ stands for the vector of the Lagrange multiplier which can be obtained from each time step; a deeper insight can be obtained from Wriggers (2006). The Lagrange multiplier is added in the equilibrium equation by a method called a predictor algorithm, which means that, at an earlier stage, the process can be considered unconstrained and later can be constrained by the corrector type of algorithm method. These two methods can generate an equation, which is to be used in the equilibrium equation in the form of a nodal velocity. Refer to Equation (4.11) (Wriggers, 2006).

$$\dot{S}_{P-\frac{1}{2}} = \frac{\Delta t_{p+1} + \Delta t_p}{2} [M]^{-1} \left\{ -Q - \left(\dot{R}^{ext} - R^{int} \right)_p \right\} \tag{4.11}$$

or:

$$\dot{S}_{P-\frac{1}{2}} = \frac{\Delta t_{p+1} + \Delta t_p}{2} [M]^{-1} \left\{ [C^b]^T \Lambda - \left(\dot{R}^{ext} - R^{int} \right)_p \right\} \tag{4.12}$$

This velocity type of Equation (4.11) is only considered when following an assumption that the contact constraint matrix is the same for the gap and gap rate as their velocities and displacements are derived from the shape functions for interpolation purposes.

4.2 Implicit contact constraint method

In the implicit arrangement, Equation (2.1) can be used to iteratively solve contact problems under certain applicable initial conditions as well. The Lagrange multiplier is the boundary condition that will be used in this section. Before discussing the implicit contact constraint in particular, the incremental method applied will be introduced briefly. The iterative increment Lagrange multiplier method is given by:

$$[K^{Lm}]\left(U^b\right)\left(\Delta U^{b+1}\right) = \bar{Q}^{Lm}(U) \tag{4.13}$$

$$U^b = U^{b+1} - \Delta U^{b+1} \tag{4.14}$$

Ahead of the two initial equations (4.12) and (4.13), the Lagrange multiplier method suggested that there were other extra variables which were compiled in vector form as follows:

$$U = (S^T \Lambda^T)^T \tag{4.15}$$

Besides the Lagrange multiplier (Λ), equation (4.15) is inclusive of the nodal displacement (S) to enable the iteration process (Wriggers, 2006). The Lagrange multiplier method can be used in conjunction with any of the three contact constraint solving steps in which the Newmark method is used for single-step time integration.

The Newton-Raphson method can be used to linearise nonlinear equations and Gauss-Seidel relaxation is used to fulfil the contact condition and friction model. These solving steps can also be used adequately without considering the Lagrange multipliers or penalty functions (Wriggers, 2006). However, in this study, only the Newton-Raphson method is considered, which was previously introduced in section 2.9 (Sippola, 2011).

$$K^{Lm} = \begin{bmatrix} \left[K_{imp}\right]^b + \left[K_t^b\right]^b & [C^b]^{bT} \\ [C^b]^b & [0] \end{bmatrix} \tag{4.16}$$

4.3 Contact mechanics computational implementation

In ABAQUS code, the two contact algorithms have been introduced, which are frictionless contacts and frictional contacts. However, the frictionless contact algorithms are only introduced, but not considered in detail. The present study is based on a dynamic load which is time-dependent.

With the assumptions made in the ABAQUS code, the following equation was used to determine the contact constraints for the interaction steps. Thus, the equation could be written in a manner as:

$$[M]\ddot{S} + [C]\dot{S} + [K]S + R^{int} - R^{ext} \tag{4.17}$$

4.4 Canister partitioning and refinements

The transportable storage cask (TSC), which is the most important component of all, was partitioned and refined towards its bottom surface 2 m from the bottom edge. This was chosen

for assessing the possibility of plastic straining. Plastic straining is not permitted on the canister, since it contains nuclear spent fuel assemblies. Refer to Figure 6.5. For all the components including the canister, structured meshing was avoided, since free meshing was preferable to capture complex geometry and high deformation gradients.

Structured meshing does provide an option that is based on the region topology. The pattern of the mesh can be predicted. But it is not acceptable to predict a free mesh pattern before generating the mesh. Owning to the distinction, free meshing permits more flexibility than structured meshing.

The free mesh approach in ABAQUS code allows complex region topologies to be meshed with triangular, quadrilateral or quad-dominated element shape options. For more information on two-dimensional regions or the tetrahedral element shape option for three-dimensional regions, refer to Dassault Systèmes (2014, Sect. 17.18.2).

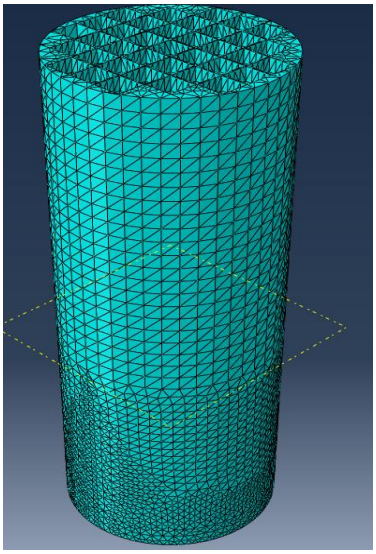

Figure 4.4: The preliminary partitioned configuration of the transportable cask.

The mesh refinement approach shown in Figure 4.4, is used to improve the accuracy of the results in regions of highest error in the solution field for the transportable storage cask (TSC). This region with high solution gradients in the displacement and stress fields, up to 2m from the bottom edge, is refined based on the mesh refinement algorithm in Abaqus/Explicit.

5. SIMULATION MODEL

5.1 Typical model geometry

A simplified model of the IDSC was developed considering its major components at the transportation stage only. The assembly of the IDSC was analysed when empty, thus nullifying the need for the cooling or safety components during simulation. In instance where these omitted components were considered, the inertial effects could be noted during simulation. The inertial effects were taken into consideration by increasing the densities of the materials i.e. stainless steel 304L and Low alloy steel. As previously mentioned, the design of the IDSC was based on the Magnastor safety analysis report. The reported densities were 7940 kg/m^3 for stainless steel 304L and 7821 kg/m^3 for alloy steel. These densities were changed to 8100 kg/m^3 and 7850 kg/m^3 respectively. The change in density brought the total weight of the components very close to the true weight of the IDSC i.e. 107 tons. The current model weight of 107.3 tons is given in Table 5.1. Therefore, it is not required to add a counterweight to take account of the inertia effects. The true stress and true strain data for low alloy steel were substituted with those of mild steel. This was because there are no data published on low alloy steel tensile test for dynamic strain rates as shown in Figure 5.6.

5.1.1 Model geometry

The complete geometry of the IDSC and the concrete pad is shown in Figure 5.1. The geometries were imported from Solidworks to Abaqus /CAE. The initial dimensions of the concrete pad are presented in XYZ-coordinates, which were x = 8 m, y = 1.2 m and z = 8 m, see Figure 5.1 for the coordinate axes. The dimensions of the IDSC part geometries can be seen in Figure 5.2. The initial model position assigned to the IDSC assembly was 1 mm away from the concrete pad. Whether use 1 mm or 0.1 mm makes no difference to the results, since the initial velocity is based on the drop height of 9 m. A larger gap will just mean that the simulation will take more computational time to solve – nothing happens until the cask makes contact.

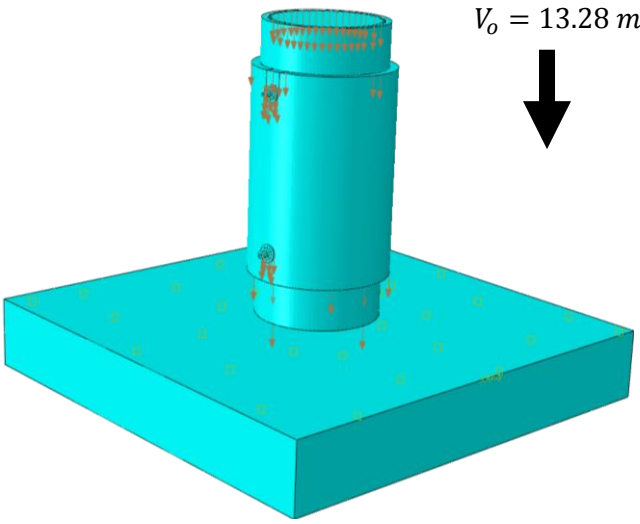

Figure 5.1: The IDSC assembly.

During the handling drop of the cask, the energy is conserved. Thus, the impact velocity can be calculated using the drop height (9 m) and equals 13.28 m/s. The drop height was assumed to be 9 m, as the worst-case scenario, which follows the testing standards established by the nuclear energy standards regulators-refer to the safety standard report (Magnastor, 2008). Initially, the movement of the IDSC was assumed symmetrical and upright towards the centre of the concrete pad throughout the process. This assumption stands quite reasonable, which optimises the contact surface area in the middle of the concrete floor. Thereafter the cask assembly was positioned at oblique angles of 60 degrees and 45 degrees with respect to the XZ plane of the concrete pad - see Figure 5.2.

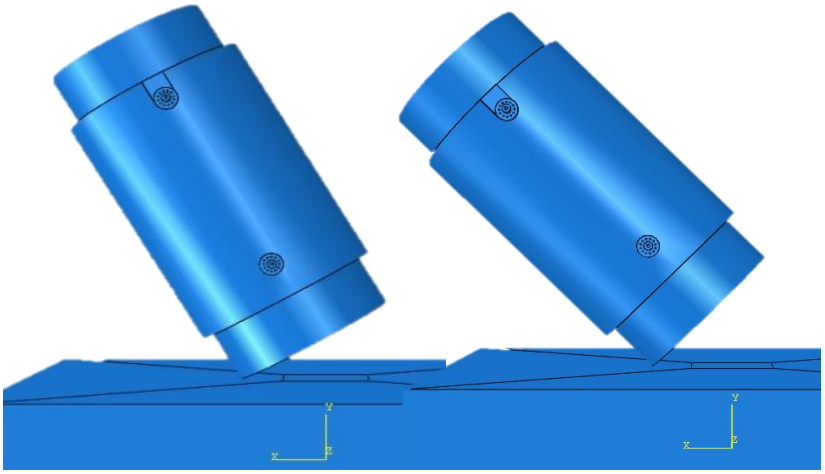

Figure 5.2: The IDSC assembly rotates at an oblique angle of 60 degrees (left) and 45 degrees.

The IDSC assembly is shown at oblique angles of 60 degrees and 45 degrees with respect to the horizontal plane. Besides the vertical drop test, it is crucial that the drop test is conducted

at these two oblique angles to establish whether the rate of deformation increases or decreases with the inclination.

The regions of higher von Mises equivalent stresses along the facet of the transportable storage cask and concrete floor are shown at the contact points in Figure 5.2. These regions of higher stress concentrations were refined to capture reasonable stress values to be compared to their material limit stresses. The mesh refinement approach is used to improve the accuracy of the results in regions of highest error in the solution field for the transportable storage cask (TSC). This region with high solution gradients in the displacement and stress fields, up to 2 m from the bottom edge, is refined based on the mesh refinement algorithm in Abaqus/Explicit. The refinement method was carried out using partition cells, which is a method to create a separation between the areas of high stress concentrations and that of low stress concentrations. For convergence purposes, different mesh density ratios are used on the (TSC) only; this will be carried out in both regions of high and low concentrations stress concentrations.

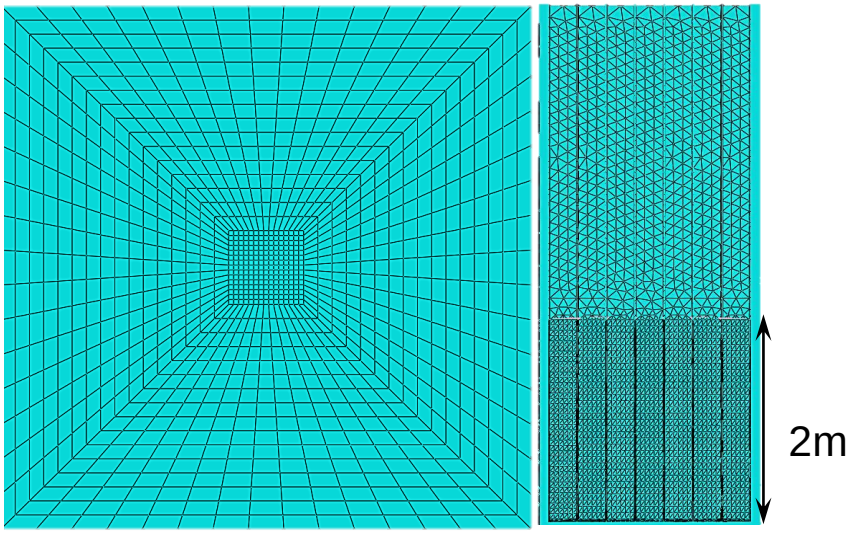

Figure 5.3: Refinement by cell partition

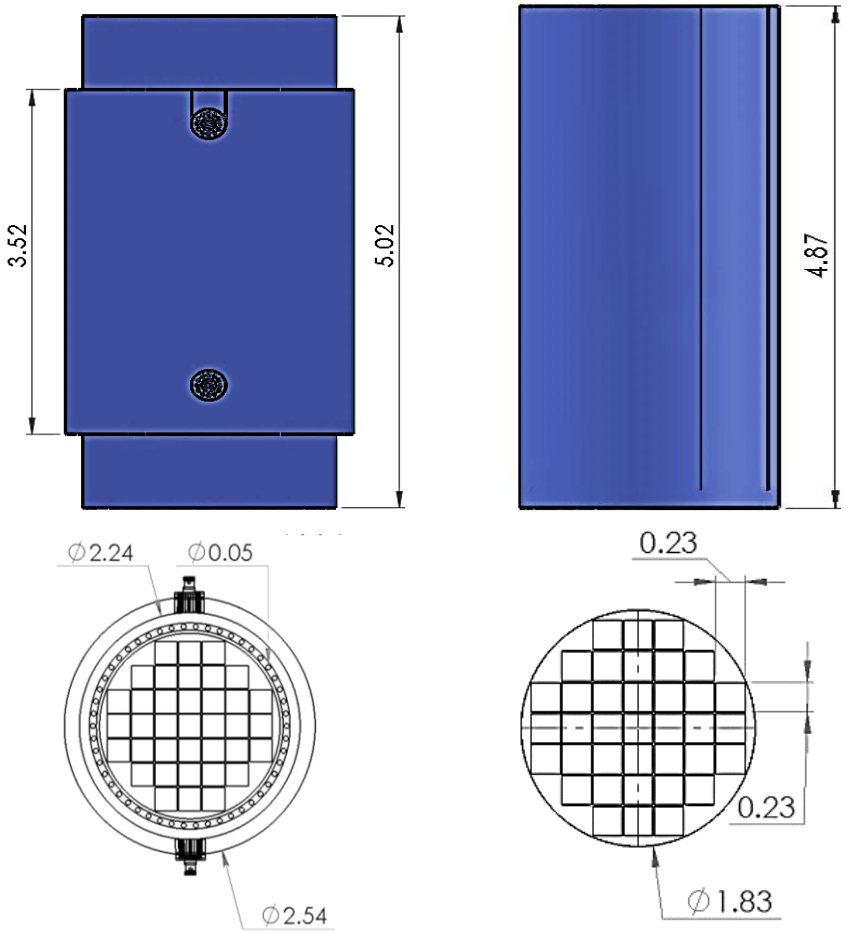

Figure 5.4: Transfer cask (left) and transportable storage cask (right)

The IDSC at transportation stage consists of a transportable storage canister (TSC) positioned inside a transfer cask (TC). Furthermore, the TC consists of an outer shell with two top and two bottom handles, as shown in Figure 5.4. There are four handles in total located on the sides of the transfer cask, for lifting purposes. The profiles and dimensions of the handles are shown in Figure 5.5.

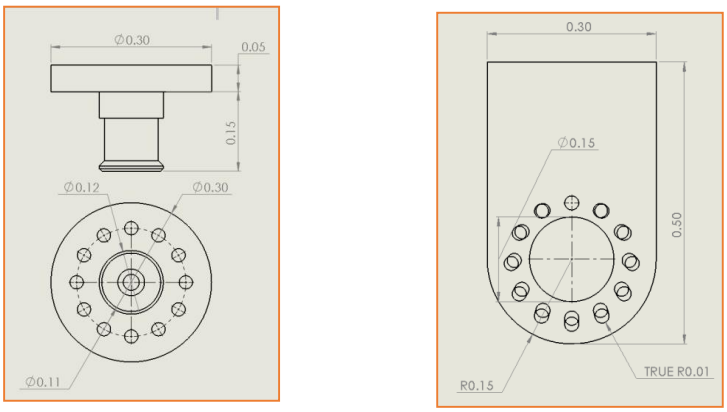

Figure 5.5: Grip handles of the IDSC dimensioned in metres.

Table 5.1: Mass properties for Whole model of IDSC at the transportation stage

Quantity	Mass (Tons)	Volume (m^3)
Body Cover	1.818	0.232
Outer shell	31.21	3.976
Transportable Storage Canister (TSC)	44.00	5.605
Transfer Cask (TC)	30.14	3.721
Top handle X2	0.140	0.018
Bottom handle X2	0.036	0.005
Total mass of the IDSC	107.3	
Total volume of the IDSC		13.56

5.2 Methods to finite element analysis

5.2.1 Explicit dynamic analysis for handling drop of IDSC onto a concrete floor

The central-difference method was used in ABAQUS/Explicit code to determine the dynamic response of the structure. The idealised central-operation theorem was introduced in the literature section. The minimum time-step size in ABAQUS/Explicit could be generated instantly by means of the Courant principle or Taylor series principle. These two principles are also mentioned in Chapter 2. The dilatational wave speed (C_d) is introduced in the code, instead of that of sound speed in a material. Equation (5.1) shown is dedicated to an isotropic material used to determine the dilatational wave speed.

$$C_d^2 = \left(\sqrt{\frac{\bar{\lambda} + 2\bar{\mu}}{\rho}}\right)^2 \tag{5.1}$$

The effective lame constants are given figuratively, i.e. $\bar{\lambda}$ and $\bar{\mu_e}$ (Sippola, 2011). As per previous studies, it was suggested that, to improve the computational efficiency, the time scale of the process should be set to a small value without inducing any computational defects while running the simulations.

As stated earlier in Chapter 2, explicit analysis is strongly relevant under the following simulations demands:

- Large dynamics problems;
- Problems associated with complicated contact surfaces (IDSC handling drop simulations or two-vehicle collisions);

- When large deformations and rotations are anticipated;
- Allows for both automatic and fixed time incrementation.

5.2.2 Energy output in explicit dynamic analysis

The energy output is mostly vital in checking the accuracy of the solution as established in the ABAQUS/Explicit: dynamic analysis, which is the total energy (ETOTAL), and it should be constant throughout the simulation process, or close to constant with an approximate error of 1%. However, there are other forms of energy, prior to the determination of the accuracy of the results, which are also known as “artificial” energies, which includes the artificial strain energy (ALLAE), the damping dissipation (ALLVD), and the mass scaling work (ALLMW). The artificial strain energy should not be greater than 5–10% of the strain energy, otherwise hourglassing could be expected and the model could require a further evaluation with different meshes to validate the accuracy of the results. The mass scaling is often used in Abaqus/Explicit for computational efficiency in case of a small step time, there is no need to perform mass scaling. Thus, the calculation results should be within the scope, once beyond the scope, then the calculation results are unreliable and need to be re-calculated.

5.2.3 Energy absorption on the concrete floor

The energy absorption on the concrete floor can be assessed with the generic static constitutive model for unconfined concrete. The method uses the generic static equation for energy conservation after being impacted by the IDSC. Therefore, the magnitude of energy absorbed by IDSC can be generated after the dynamic simulations. The generic static equation is based on the estimation conducted earlier on the expected penetration depth; as refer to section 3.2.2.

5.2.4 Material properties

The choice of the material at transportation stage is based on structural integrity as well as radioactive protection (Magnastor, 2008). Thus, a metallic structured system is used to prevent highly radioactive material from passing through to the environment (Romanato, 2011). The TC is made from low alloy steel and the TSC of a stainless steel**.** The transportation of the IDSC to its final disposal occurs over a concrete floor. The properties of all materials for the analysis are presented in Table 5.2. Based on these material properties, the IDSC components can be analysed for both linear elastic and plastic deformation.

Table 5.2: Material properties of metallic interim dry storage cask

Material	Density	Young's Modulus	Poisson's Ratio	Yield Stress
Austenitic Stainless Steel 304 L	8100 kg/m^3	193 GPa	0.27	410 MPa
Mild Steel	7850 kg/m^3	210 GPa	0.3	366 MPa

In addition to Table 5.2, the ABAQUS FE code, which is used for the FE analysis, requires that the above tabulated material properties to be associated with material strain values. These values could be initially obtained from the uniaxial tensile test, which yields the following values of strain:

$$\varepsilon_m = 0.51 \quad \text{and} \quad \varepsilon_u = 0.38$$

$$\varepsilon_m = 0.37 \quad \text{and} \quad \varepsilon_u = 0.29$$

where ε_m the engineering strain at breaking point, and can be obtained from the pre-stressed length of the tensile specimen after the test, and ε_u is the necking strain at the corresponding ultimate stress (Laubscher, 1997). The corresponding ultimate stresses measured at necking are as follows:

$$\sigma_u = 650 \text{ MPa} \qquad \text{and} \qquad \sigma_u = 567 \text{ MPa}$$

The preferred plasticity model uses the associative flow rule with von Mises yield criterion and isotropic hardening. In ABAQUS code, it is suggested that the logarithmic elastic strain has to be small in order for the additive strain rate decomposition to be used (Sippola, 2011). The total strain of the solid continuum in ABAQUS code plasticity models is determined by an integral to the rate of deformation.

In order to approximately calculate this integral point, the central-difference scheme is used in association with the approximated rigid body rotations during the increment. More details may easily be found in the ABAQUS code (Dassault Systèmes, 2014). ABAQUS code also provides the approximated matrix, although the approximation made in the formulation improved the convergence rate.

The approximations made in the formulation work better with the use of isotropic plastic behaviour and isotropic hardening but may give problems with anisotropic plastic behaviour of the kinematic hardening, when large strains and rotations are present (Sippola, 2011). The

uniaxial plasticity data has to be converted to the true stress and logarithmic plastic strain measures. The formulae for version are:

$$\sigma_t = \sigma_e(1 + \varepsilon_e) \tag{5.2}$$

and

$$\varepsilon_{log}^{p} = ln(1 + \varepsilon_e) - \frac{\sigma_{true}}{E} \tag{5.3}$$

where σ_t is the true stress, ε_{log}^{p} the logarithmic plastic strain (also known as true plastic strain); E the elastic modulus; σ_e the engineering stress; and ε_e the engineering strain (Dowling, 2012). The engineering strain of a homogeneous material specimen is equated to the necking strain at the corresponding ultimate stress $\varepsilon_e = \varepsilon_u$. This relationship can be used in Equation 5.2 and Equation 5.3. The strain values are required on the stress-strain curve to determine the approximate linear work hardening curve for the material input data. However, the implementation of true stress and true strain formulations is not needed because the data provided in the conducted tensile tests with different metallic material properties by Laubscher 1997 will be used as input to the ABAQUS/Explicit FE Code. The presented results were obtained using both quasi static and dynamic strain rates, where the stress-strain fitting parameter was 0.2% which is the engineering offset strain. Thus, a set of true stress and true strain values were made available for materials such as mild steel and austenitic stainless steel (304L), as shown in Figure 5.6. The engineering stresses and true stresses are shown below at their respective strains:

$\sigma_y = 410$ MPa at $\varepsilon_{log}^{p} = 0$ and $\sigma_t = 897$ MPa at $\varepsilon_{log}^{p} = 0.32$

$\sigma_y = 366$ MPa at $\varepsilon_{log}^{p} = 0$ and $\sigma_t = 697$ MPa at $\varepsilon_{log}^{p} = 0.22$

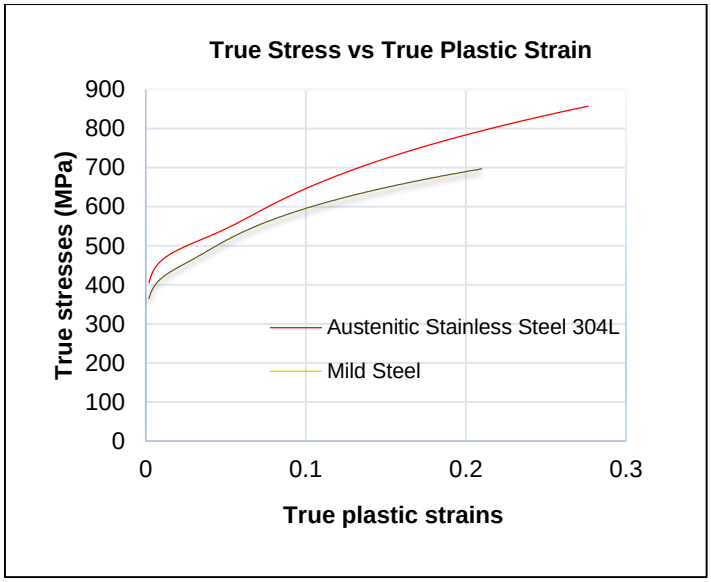

Figure 5.6: Stress- strain curves for both austenitic stainless steel (304L) and mild steel

This conforms to the previous conducted tensile tests for different dynamic strain rates (Laubscher, 1997). The strain rate for austenitic stainless steel (304L) was $0.5x10^2$ and that for low alloy steel as $0.9x10^2$. The stress-strain curve were effected using Mathcad. This study uses three types of materials, which includes austenitic stainless (304L), unconfined concrete and low alloy steel. The material restrictions used as an input to ABAQUS and are tabulated in Tables 5.3 and 5.4, in additional to Table 5.2.

Table 5.3: Material properties

Material	Engineering Strain	Necking Strain	Ultimate Strength
Austenitic Stainless 304 steel	0	0.32	897 MPa
Mild Steel	0	0.22	697 MPa

Table 5.4 below shows data input to ABAQUS taken from a previously conducted study for four different concrete grades as mentioned in section 3.2. The data is that for grade 50 concrete strength (B50).

Table 5.4: Material properties for unconfined concrete floor with SCDP in grade 50

Material parameters	B50	Plastic parameters	
		Dilation angle	31
Concrete elastic		eccentricity	0.1
Young modulus (GPa)	33.4 0.2	f_{bo}/f_{co}	1.16
		K	0.67
		Viscosity parameter	0
Concrete compressive behaviour		Concrete compression damage	
Yield stress (MPa)	Inelastic strain	Damage parameter	Inelastic strain
25.5	0	0	0
50	0.0066772	0	0.0066772
Concrete tensile behaviour		Concrete tension damage	
Yield stress (MPa)	Cracking strain	Damage parameter	
5	0	0	0
0.05	0.001494322	0.99	0.00149322

5.3 Boundary conditions

The drop test analysis requires an understanding for both deformable and rigid bodies. During the FE-simulations, the concrete pad base was set as both rigid and deformable for energy absorption purposes.

5.3.1 Deformable body model

For all of the IDSC parts' geometries, the same boundary conditions for the symmetric planes were set; this included all the possible parts of the assembly as could be seen in Chapter 4. A proper understanding of contact mechanics was established between the parts in contact. In ABAQUS, surface contact constraints are purely a master to slave algorithm. This algorithm procedure is very important in node-to-surface discretisation (Dassault Systèmes, 2014).The corresponding displacement boundary condition of the cask assembly was set similarly to that of the rigid body model with an option of 9 m drop test. In this procedure, all assembly components and the concrete pad were set as deformable bodies. Therefore, it reduced the energy absorption of the IDSC assembly. The concrete floor was fixed at the bottom surface in order to prevent movement during the simulations.

5.3.2 Rigid body model

At the reference point of the rigid body, the concrete pad was fixed in all directions of the degrees of freedom. Similar to that of a deformable body, a corresponding boundary condition displacement of the cask assembly was set to move downwards after being suspended from a height of 9 m. ABAQUS provided a rigid body capability for computational efficiency. Compared to deformable bodies, rigid bodies are more advantageous as their motion is categorised completely by no more than six degrees of freedom at a specific node.

Deformable element bodies therefore require many degrees of freedom and costly element calculations to control the deformations. Once such deformations are not accounted for or are of less interest, the component is modelled as a rigid body and produces substantial computational savings without upsetting the general results. This implies that in work studies, rigid bodies were used at a certain stage to assess the energy absorbed by the IDSC.

5.3.3 Mesh convergence and elements

Mesh convergence study was mentioned earlier in Chapter 2. The method facilitates several mesh refinements in the regions of higher stress concentrations at an assigned mesh density ratio. Figure 6.2 is a stress versus degrees of freedom; this should be in an illustration of a degree of convergence permitted during the simulation.

5.3.4 Element types

First-order elements such as brick element (C3D8R) and tetrahedral element C3D4 were used in this study. As previously mentioned, brick element was used on concrete floor and tetrahedral element used on IDSC assembly. Brick element has a better convergence rate than tetrahedral element C3D4. It is very convenient to mesh a complex shape with tetrahedral element. The problem with tetrahedral element C3D4 is that, it may exhibit slow convergence with mesh refinement; however, convergence and accuracy results can still be possible with very fine meshing, to avoid the solution to diverge.

5.3.5 Uniaxial tests result for duplex stainless steel

The experimental uniaxial tests were conducted on duplex stainless steel 2205 as part of this work. These tests were conducted using 4 samples at different exposure temperatures (due to radiation heating of stored spent nuclear fuel), as shown in Figure 5.8. The idea was initiated in order to disclose a comparison between the yield stresses of duplex stainless steel 2205 (DSS) and austenitic stainless steel 304L (Magnastor, 2008) used in this study, for possible future work. The results obtained are briefly introduced below.

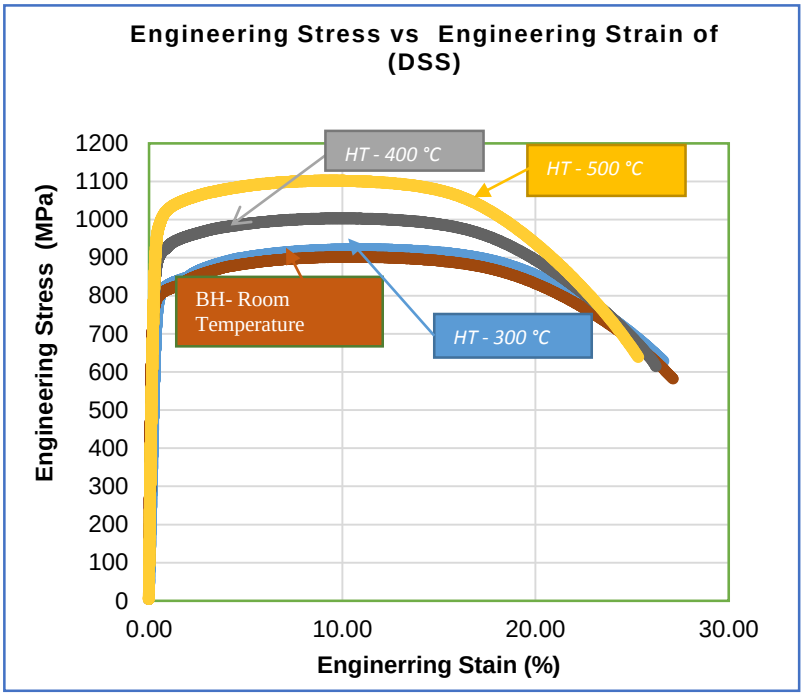

Figure 5.7: Idealised stress-strain curve for duplex stainless steel 2205.

The comparison between austenitic stainless steel 304L and duplex stainless steel 2205 is illustrated in Figure 5.8. The yield stress plotted in Figure 5.6 was recoded at an ambient temperature of 20 degrees. Figure 5.8 was plotted using different sample temperatures to obtain engineering values and can be used to determine true stress and true strain values. The true values obtained are relevant for ABAQUS input data. Based on Figure 5.8, duplex stainless steel 2205 gives a higher yield strength (800MPa) at ambient temperature, as compared to the yield strength of austenitic stainless steel 304L (410MPa) used in this study.

5.3.6 Explicit analysis element

During the ABAQUS/Explicit analysis, solid continuum elements were most suitable in conjunction with first-order elements. Excessive element distortions were encountered with the use of second-order elements. Therefore, ABAQUS/Explicit analysis was carried out with first–order elements and the accuracy of the results was acceptable.

5.3.7 Accuracy of finite element analysis

The accuracy in results of the IDSC simulations requires a proper selection of element types and mesh sizes. Therefore, in the regions of high deformation, mesh refinement was applied and the element type changed accordingly to improve the accuracy of the results.

5.4 ABAQUS/Explicit contact definition

5.4.1 Explicit analysis contact interaction modelling

ABAQUS/Explicit code provides two ways in which contact interaction can be modelled: general contact and contact pairs (Hofsrud, 2017). General contact allows the definition of contact between many or all regions of a model with a single interaction. General contact can reach many disengaged regions of a model. Contact pairs describe contact between two surfaces and need more precision on contact definition. Every possible contact pair interaction must be defined, and many restrictions are associated with the types of surfaces involved. Figure 5.8 and Figure 5.9 below illustrate the contact definition between each component as well as the construction of the IDSC and concrete pad. The interfaces between components of the IDSC require contact interactions to be defined. All parameters necessary to define contact interactions are taken into account. These include the proper definition of the friction coefficient of the surfaces in contact as well as the mechanical constraint formulation, i.e. the penalty contact parameter to avoid surface penetration (Crocker, 2017). The magnitude of the coefficient of friction over all surface contacts is based on a previous study (Peng-Cheng et al. 2008) in which the coefficients of friction for steel-steel and steel-concrete were established experimentally using the table shaker method. It was concluded that the friction coefficient for steel-steel can range from 0.15 to 0.6, and for steel-concrete from 0.5 to 0.8. In this study, a value of 0.5 was used for steel-steel contact, and 0.7 for steel-concrete contact. The choice of friction parameter can have an impact on the deformation. By using higher levels of friction, greater deformation of the surface can be obtained (Crocker, 2017), and is therefore a conservative approach in ensuring design integrity.

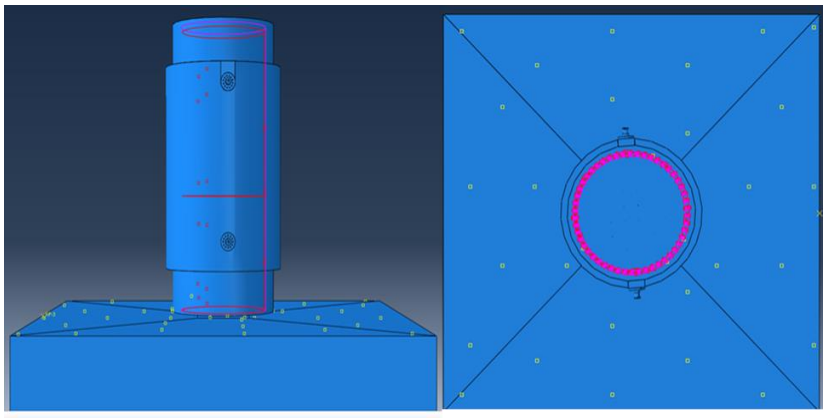

Figure 5.8: Contact interactions between components of the IDSC assembly.

Each part was selected independently and assigned either master surface or slave surface with an appropriate rubbing coefficient of friction of 0.5. This coefficient of friction stands for steel-steel contact.

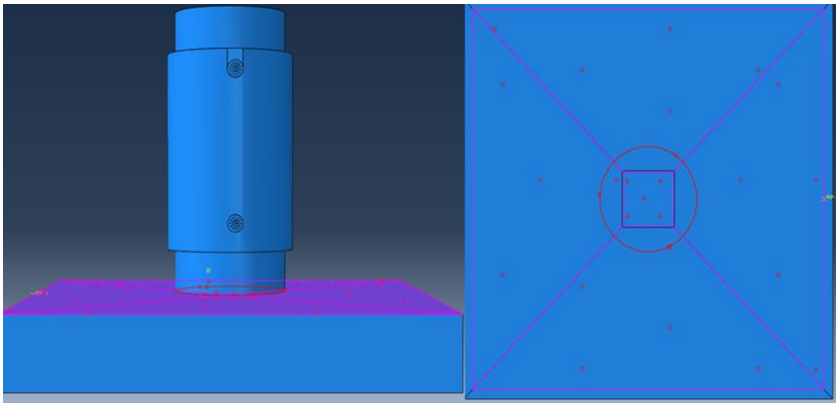

Figure 5.9: Contact interaction between concrete pad and the bottom face of the IDSC.

This was the last contact interaction for the model with a rubbing coefficient of friction of 0.7 as based on their material properties.

5.4.2 Explicit analysis contact interaction modelling

In ABUQUS/Explicit analysis simulation, it is possible that both contact pairs and general contact are used together. The application of contact pairs is aligned with the explanation provided in Chapter 4. The method required that surfaces in contact to be well defined in terms of master and slave surfaces. Whereas general or automatic contact doesn't need any surface definition. Contact definitions are not entirely automatic with the general contact algorithm but are greatly simplified.

Both contact approaches require that each contact interaction is aligned with a contact property, and this includes contact pressure-clearance relationships and friction. In the same way, each selected element is to be aligned to an element property. This invokes a decision on the relative sliding magnitude to assess whether small sliding or finite sliding occurs during contact interaction. The default is the finite-sliding method. The small-sliding method, however, is advised to find the relative motion of the two surfaces lower than a small proportion of the characteristic length of an element face. Hence, using the small-sliding method can result in a more efficient analysis.

.

6. RESULTS DISCUSSIONS AND VALIDATION

6.1 Mesh convergence study

Mesh convergence study was conducted by increasing the number of elements in the regions of higher stress concentrations. There are two of the seven components of the IDSC that needed careful study of regions of high stress concentrations: the inner-shell 2 m from its bottom edge and the outer-shell along the full shape. The number of elements was increased by changing to finer mesh density ratios (1:6, 1:8, and 1:10, 1:12 and 1:14). These meshing density ratios were tested at a drop angle of 90 degrees to the horizontal. As found by many researchers, the mesh quality and mesh density ratios are directly associated with the solution accuracy. Therefore, this process was carried out in order to select a suitable mesh density ratio that could be maintained throughout the FE-simulations of the two oblique drops at the orientation angles of 45 degrees and 60 degrees as well the rigid base. After initiating the convergence study, the results converged very well as expected. Nevertheless, there were discretisation errors that occurred at the very first mesh density ratio of 1:6, as shown in Figure 6.1. The converged results presented in Figure 6.1 were recorded in the regions of higher stress concentrations along the entire shape of the IDSC model.

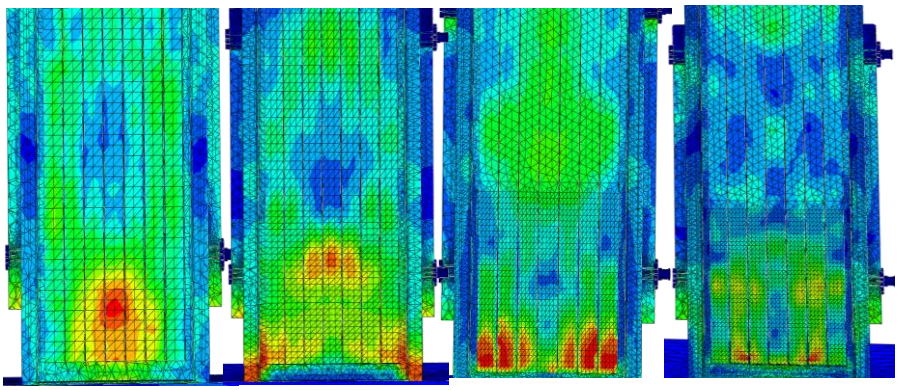

1:6	681	1:8	424.8	1:10	425.4	1:12	426	1:14	426.6	MPa

Figure 6.1: Converged von Mises stresses for entire model (IDSC).

Different meshes are developed with different body, face, and edge sizing control in ABAQUS/EXPLICIT.

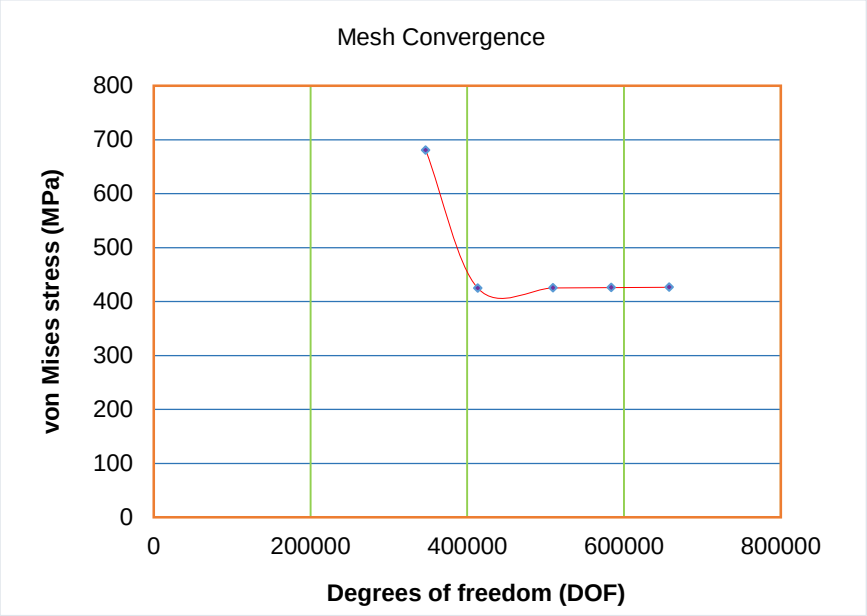

Figure 6.2: Graph of degrees of freedom versus von Mises stress for all model (cask).

The discretization error that occurred when using a mesh density ratio of 1:6 is shown in Figure 6.2, for which high stress values were obtained for the case of fewer elements. The results started converging from a mesh density of 1:8 up to 1:14, due to the higher number of nodes, resulting in stable energy transfers as shown in Table 6.1. Mathematical or experimental simulations can be performed to obtain the meshing density that should be used in numerical analysis. The convergence study revealed that the mesh density of 1:12 is preferred over 1:14, since the latter requires more computational time with no significant change in the von Mises stresses. In this study, solid hexahedron elements and tetrahedron elements were used.

Table 6.1: Mesh density ratios and associated simulation parameters

Mesh Ratios	User Time (Sec)	CPU Time (Sec)	Total Internal Energy(J)	Number of Elements
1:6	25100	39000	0.947×10^{12}	495877
1:8	26500	30900	0.948×10^{12}	581756
1:10	33200	38600	0.948×10^{12}	720434
1:12	41000	47900	0.948×10^{12}	824103

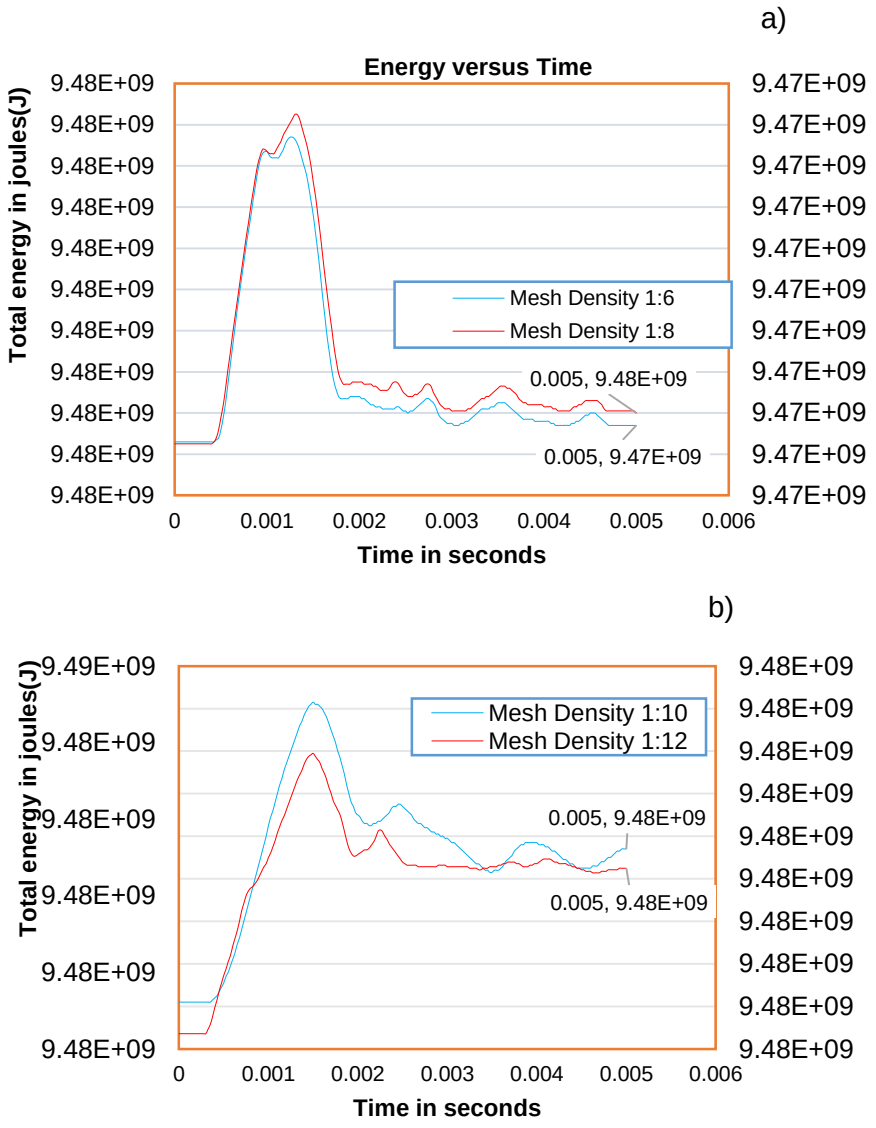

Figure 6.3: Convergence of the total energy for the entire model (IDSC).

The curves shown in Figure 6.3 depict the converged results for the total energy, presented in a sequence of different mesh density ratios: (a) 1:6 and 1: 8, (b) 1:10 and 1:12. The total energy of the entire model is obtained from the energy balance equation for the entire model which is the additional internal energy (ALLIE), the viscous energy dissipated (ELVD), the frictional energy dissipated (ALLFD), the kinetic energy (ALLKE), and the work done by the externally applied loads (ALLWK), which is zero in drop test analyses. Based on the ABAQUS guidelines, the total energy across the majority of the critical elements should be constant, but with only an approximate constant error of less than 1%. Thus, the plots of the four mesh density ratios illustrate the approximate constant error of less than 1%. This ensures the dependability of the results obtained. Another important aspect that can be observed to ensure

the accuracy of the results is the comparison between the two last mesh ratios of 1:10 and 1:12. The results obtained for these two mesh ratios show no difference, as shown Figure 6.2.

6.2 Vertically drop over a deformable floor

6.2.1 Von Mises equivalent stresses

In the finite element method, at any point, there are stresses acting in different directions, thus the direction and magnitude of stresses change from point to point. The von Mises criterion is a formula for calculating whether the stress combination (effective stress) at a given point will cause failure as based on the yielding criterion of a ductile material. The displacements and rotation, if present in the finite element analysis, are calculated at each nodal point, but the stresses and strains are evaluated at the element integration points. In this study, the attention is more on the two major components of the IDSC, which ate the TSC and TC as mentioned earlier. The magnitudes of displacements, equivalent plastic strains and stresses are recorded along the surfaces of the TSC and TC in the high stress concentrations regions. The recorded results of stresses were compared with the yield stress of the material at hand. Figure 6.4 below illustrates different mesh densities along the surfaces of the TC.

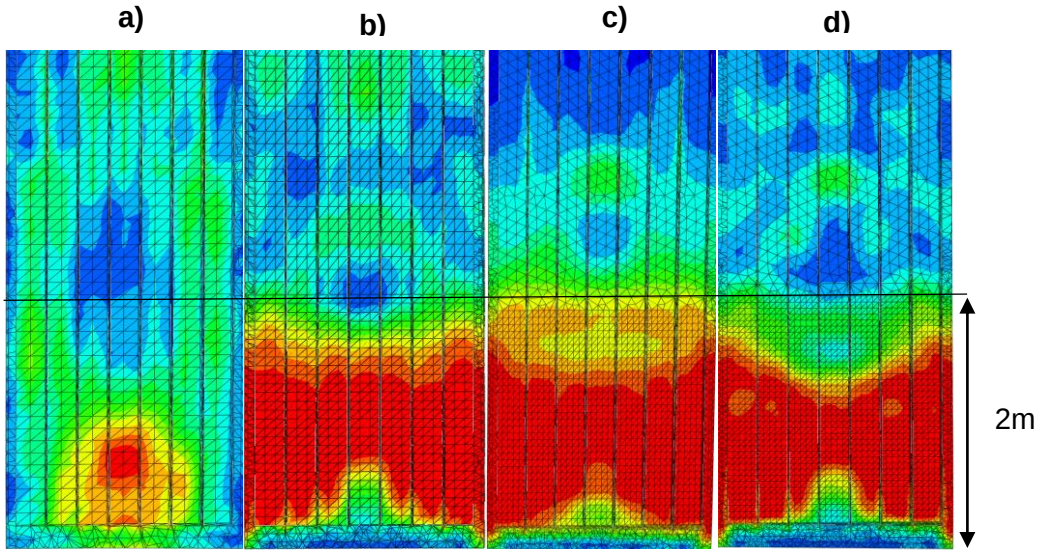

Figure 6.4: Mesh density ratios in the region of high stress concentration of the inner-shell.

It is shown in Figure 6.4 that the number of elements amended with the choice of the mesh density which includes: a) 1:6, b) 1:8, c) 1:10 and d) 1:12.

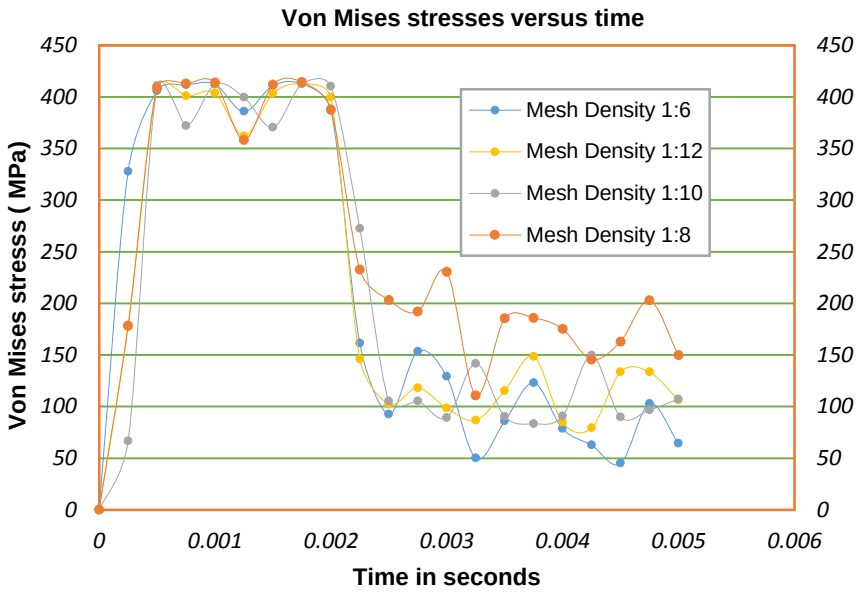

Figure 6.5: Stresses in the region of high stress concentration of the inner-shell vs time.

The results of the von Mises stresses shown in Figure 6.5 are consistent in the regions of high stress concentrations when using different values of mesh density in each element formulation. Whether using the low mesh density or the high mesh density of mesh modes, all cases recorded the same value of von Mises stress in a particular group of element formulation used. Hence, it appears that using different types of mesh densities does not affect the results significantly. The maximum von Mises stress was recorded as 413 MPa at a mesh density of 1:12, which exceeded the material yield strength (410 MPa). This implies that plastic deformation should be expected of greater than zero on the inner-shell.

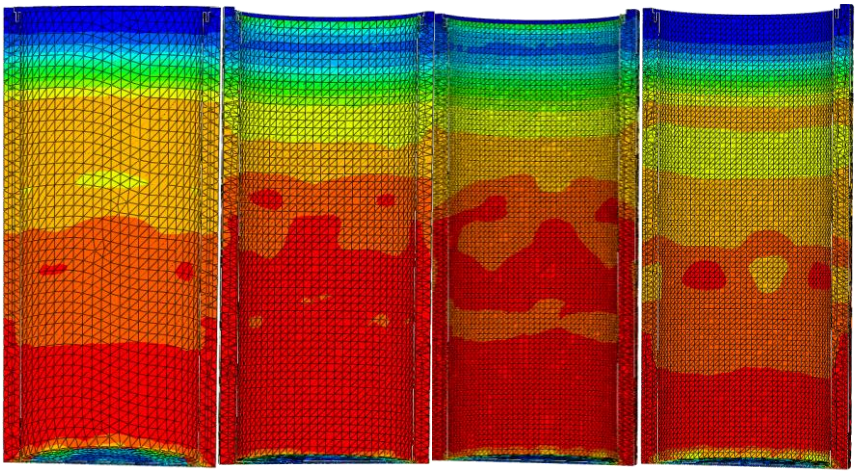

Figure 6.6: Mesh density ratios in high stress concentration region on the outer-shell.

Figure 6.6 depicts that the region of high stress concentration occurs along the full surface of the outer-shell, whereas on the inner-shell, it is just across 2 m from the bottom (point of

impact). The mesh density ratios were kept the same as on the inner-shell as shown Figure 6.7.

.

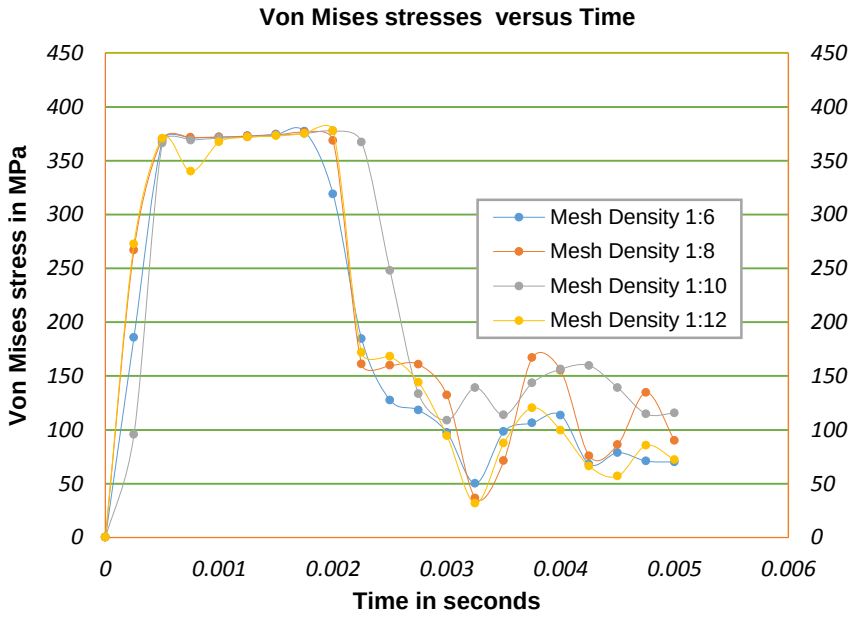

Figure 6.7: Stress distribution vs time in high stress concentration region on the outer-shell.

The result of von Mises stress is consistent in the region of higher stress concentrations as well when using different value of converged mesh density. In comparison with the inner-shell the recorded result of stress (378 MPa) went beyond the material's limit stress such mild steel 366 MPa. Therefore, it appears that the outer-shell absorbed more impact stress rather than the inner-shell or any other component of the IDSC.

6.2.2 Equivalent plastic strain at integration points

The ABAQUS code provides the equivalent plastic strain in a material (PEEQ) as a scalar variable that should be used to characterise the material plastic deformation. This variable, once greater than zero, indicates that the material has reached its yielding range. Figure 6.8 and Figure 6.9 show the results of equivalent plastic strains when using the various types of element sizes as mentioned above.

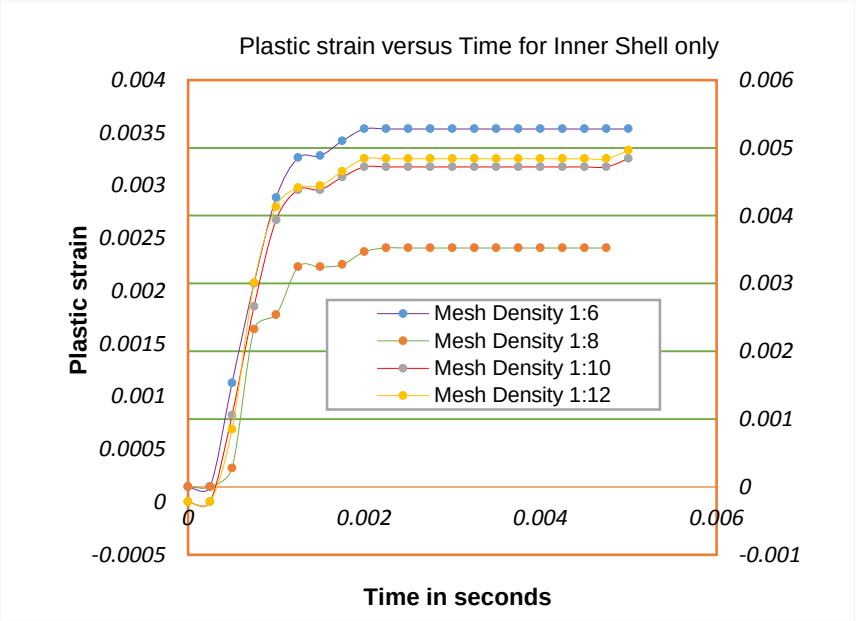

Figure 6.8: Plastic strain vs time in high stress concentration region of the inner-shell

Figure 6.8 illustrates two equivalent plastic strain scales of the converged results. The equivalent plastic strain values on the left can be used for three mesh densities except that of 1:10, which varies with the equivalent plastic strain values on the right. For all four mesh densities, the results converged to a value of less than 0.1 or not greater than 0.0035. This shows that numerical analysis of the IDSC indicates no significant plastic deformation on the inner-shell.

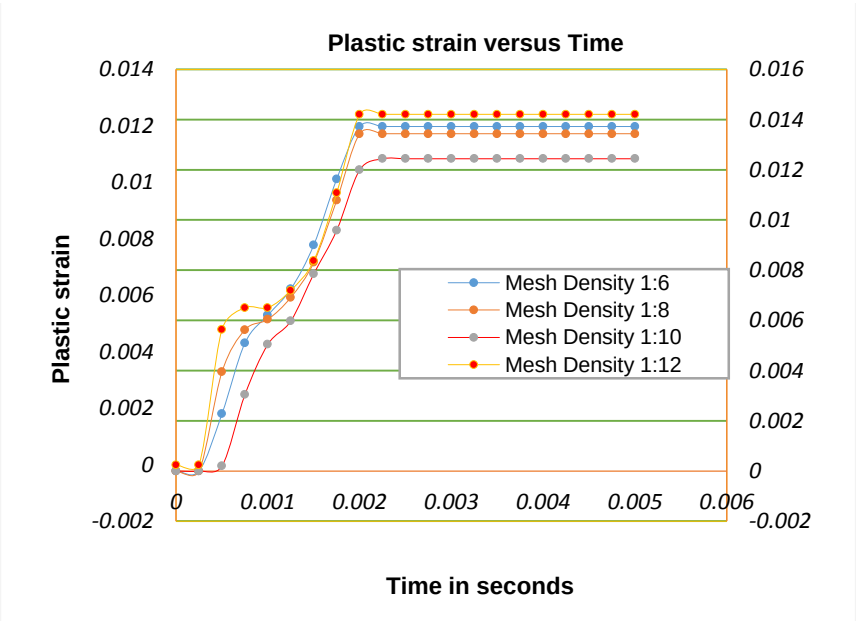

Figure 6.9: Plastic strain vs time in high stress region on the outer-shell.

Figure 6.9 illustrates two sets of the converged results of the equivalent plastic strain, which read the same as those shown in Figure 6.8. As mentioned earlier, the von Mises stresses obtained during the simulation exceeded the limit stress in the high stress region on the outer-shell. This induced an equivalent plastic strain (0.0124) that exceeded that obtained on the inner-shell. However, the equivalent plastic strain obtained is far less than that compared to the true plastic strain limit of 0.22 at a material point. This shows that though the plastic deformation may be expected on the outer-shell but the material will not fracture, as explained in Section 5.1.

6.3 Oblique drops over a deformable floor

The results obtained for an impact angle of 45 degrees on the inner-shell as shown in Figure 6.10 were higher as compared to the 90 degrees drop (Figures 6.5 and 6.8), by 30% on stress and 98.4% on strain, but less than the results obtained for a drop at an angle of 60 degrees as shown in Figure 6.11. The latter increased by a percentage difference of 0.02% on stress and 0.1% on strain. The results obtained exceeded the limits of the yield stress for stainless-steel grade 304L (410MPa). Based on engineering judgement, once stresses in a given material exceed the yield limit, plastic strains are present in these areas of high stress concentrations.

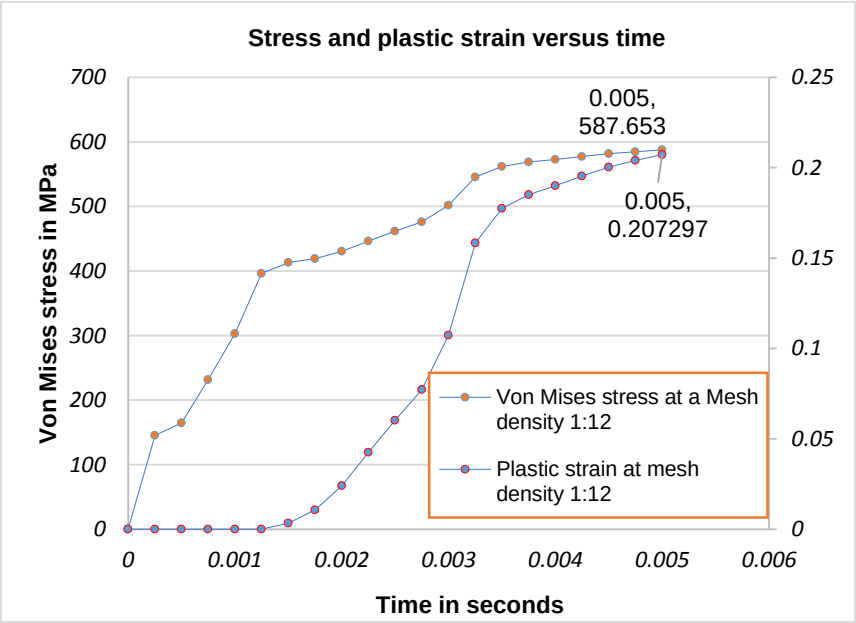

Figure 6.10: Maximum stress and maximum plastic stain on the inner-shell related to time at a 45 degrees angle.

.

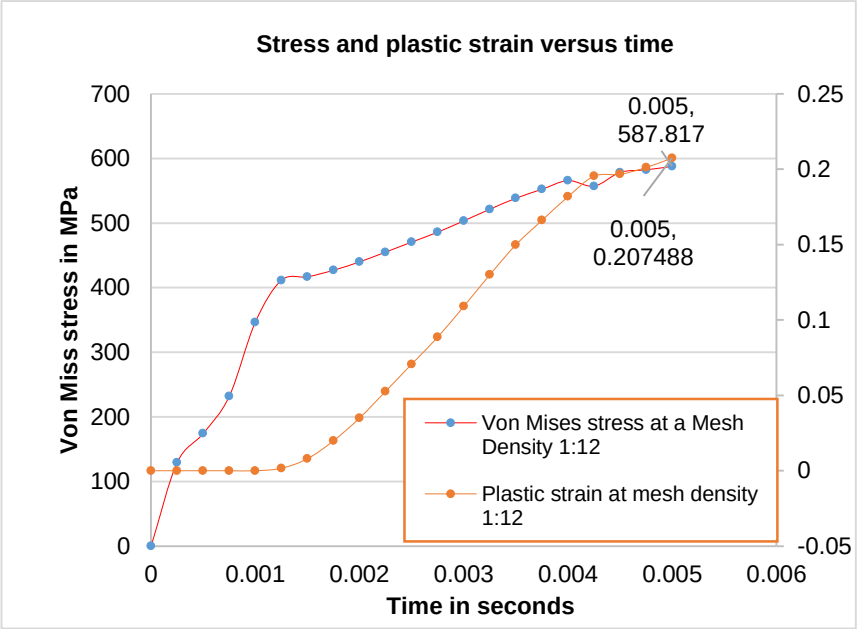

Figure 6.11: Maximum stress and maximum plastic stain on the inner-shell related to time at a 60 degrees angle.

Figure 6.11 shows that the results of von Mises stresses and equivalent plastic strains when using an oblique drop at an angle of 60 degrees with a mesh density of 1:12. The depicted results were captured in the region of high stress concentrations, which is approximately near the bottom surface of the shape. The maximum von Mises stress was 587.8 MPa, which gives a plastic strain of 0.22. This implies that an oblique drop may cause more damage on the IDSC in comparison to a vertical drop.

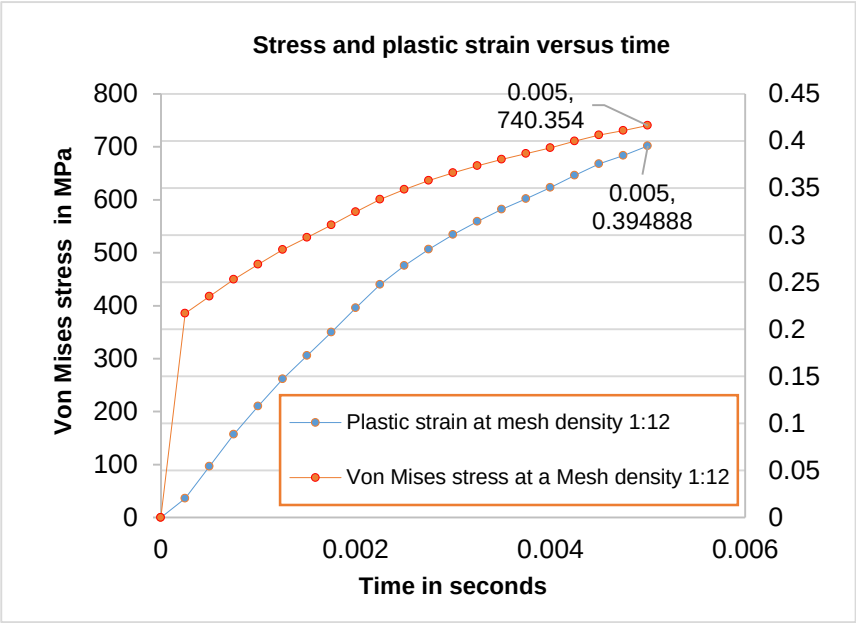

Figure 6.12: Maximum stress and maximum plastic stain on the outer-shell at a 45 degrees angle.

The magnitudes of von Mises stress and equivalent plastic strain obtained on the outer-shell are high (740.4 MPa and 0.4) as compared to the results obtained on the inner-shell. This shows that more impact energy was absorbed by the outer-shell.

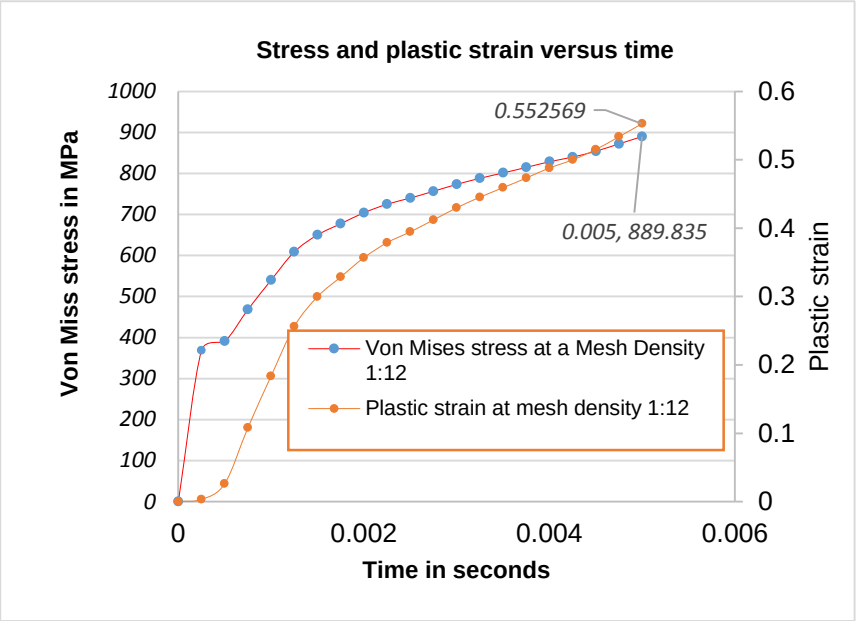

Figure 6.13: Captured maximum stress and maximum plastic stain on the outer-shell at a 60 degrees angle.

Figure 6.13 displays the results obtained on the outer-shell when for an oblique angle of 60 degrees. The magnitudes of von Mises stress and equivalent plastic strain obtained on the outer-shell are higher (889 MPa and 0.55) as compared to the results obtained on the inner-shell. The results are higher as compared to the two previous orientations considered, i.e. the 45 degrees and 90 degrees' impacts. This implies that a drop at an angle greater than 45° but less than 90° can induce greater damage to the IDSC.

6.4 Spatial displacement at nodes

Nodes in finite element analysis have nodal displacements or degrees of freedom which may comprise translations, rotations, and higher order derivatives of displacements in special cases. When the nodes displace, will necessitate the move of the elements along in a certain manner dictated by the element formulation. This implies that, displacements of any points in the element will be interpolated from the nodal displacements. This is the fundamental reason for the approximate nature of the solution. Abaqus/Explicit analysis uses variables such as displacement, velocity, and acceleration at a nodal point of an element. The nodal displacements are used to calculate velocities and accelerations.

The analysis uses the incremental procedure, which allows the variables such as velocities and accelerations to vary from their current increment position of p to calculate the next

increment of $p+1$. The displacement as a result of the changed increment is given as S_{P+1} and the velocity term varied by half a time increment is $\dot{S}_{P-\frac{1}{2}}$. In this type of analysis, the expectation is that, if the increments are small enough, the results will be accurate. But the problem with this method is that numerous small increments are required for accuracy and are time consuming. If the number of increments is not sufficient, the solution tends to drift from the correct solution.

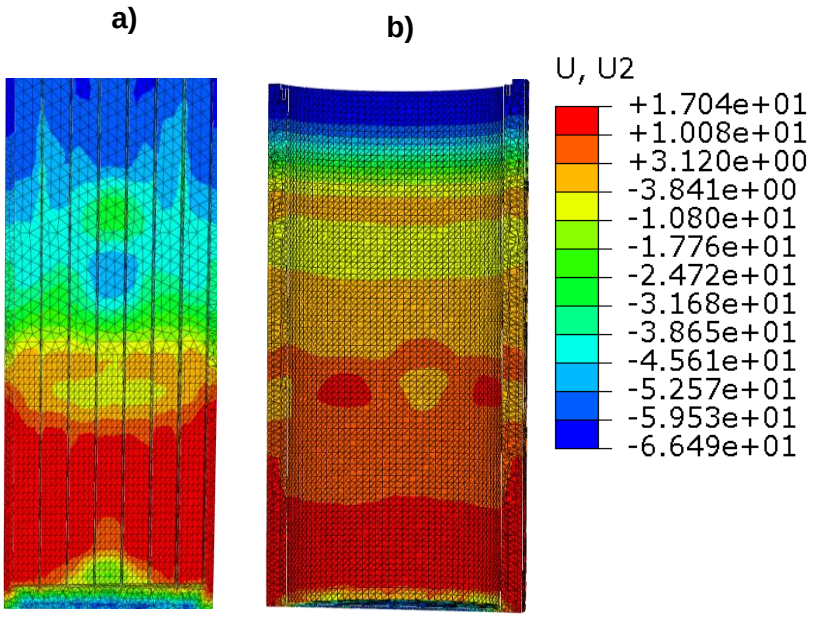

Figure 6.14: Maximum displacement on the inner shell (a) and outer-shell (b).

The results of maximum displacement in the Y-axis (U2) under the vertical drop are shown in Figure 6.14. The maximum compressive displacement of 66.49 mm is experienced on the outer-shell. This magnitude of displacement should as well be expected on the inner-shell at a 90 degrees drop. With inclusion of the concrete floor, tensile displacement in a direction U2 is absorbed by the concrete floor.

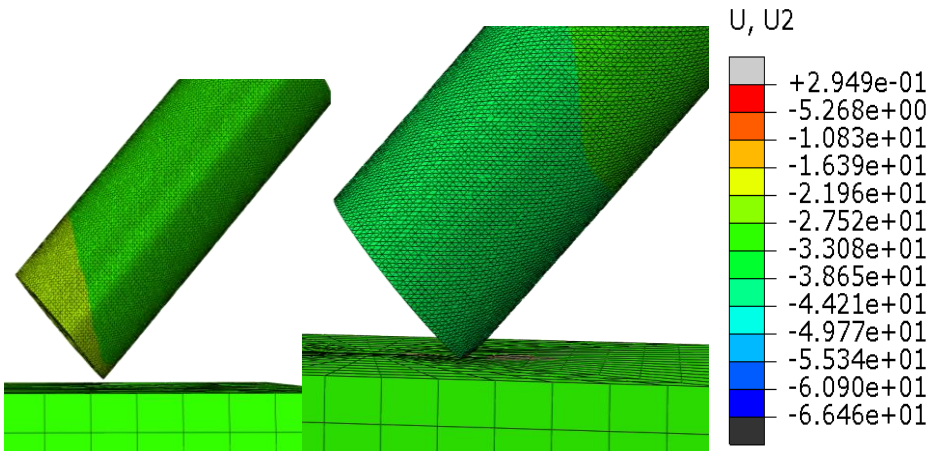

Figure 6.15: Maximum displacement at an oblique angle 45 degrees.

There was negligible difference between the nodal displacement results (66.46 mm) in the U2 (Y-axis) direction at the rotational angle 45 degrees and those obtained at an angle of 90 degrees as shown in the above configurations (Figure 6.14 and Figure 6.15).

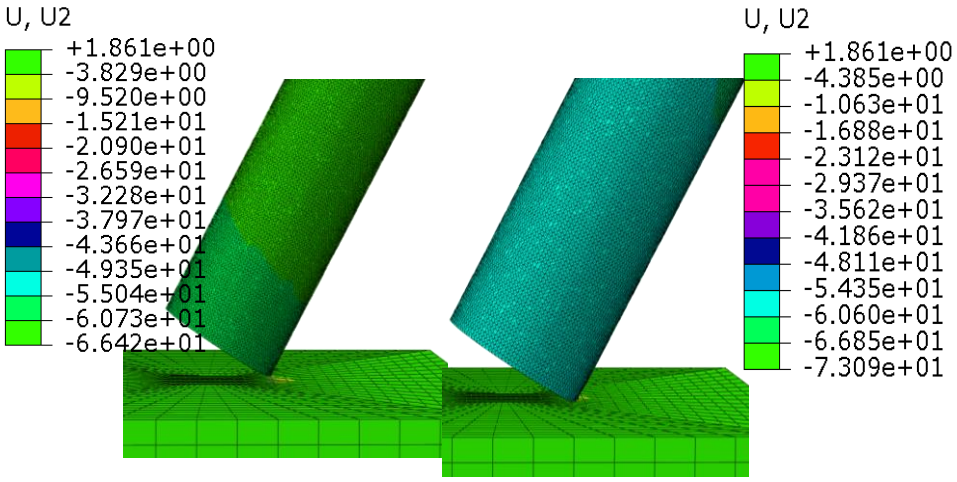

Figure 6.16: Maximum displacement at an oblique 60 degrees.

Figure 6.16 shows, the displacement results (73.09 mm) in the U2 (Y-axis) direction at a rotational angle of 60 degrees were slightly higher than those obtained at the angles of 90 degrees and 45 degrees. This implied that if the IDSC was dropped at angle between 45 degrees and 90 degrees, it would result in a slightly higher displacement.

6.5 Vertical drop over a rigid floor

The vertical drop was tested on both deformable and rigid bases in the FE-simulation in order to investigate whether it is possible to capture the large deformations in the ABAQUS/Explicit code, as presented in the theory section of this study.

The highest von Mises stress value obtained on the inner-shell while dropped over a rigid base is 6 times greater than the maximum stress value obtained over a deformable base, see Figure 6.5 and Figure 6.18. Therefore, the energy absorbed by the IDSC during the simulation of the entire geometry of the IDSC will experience a larger plastic deformation if it falls over a rigid surface. The model of the IDSC is made of seven different parts, but only one component is the most important i.e. the TSC, which is made of stainless steel and in which the spent fuel assemblies are held.

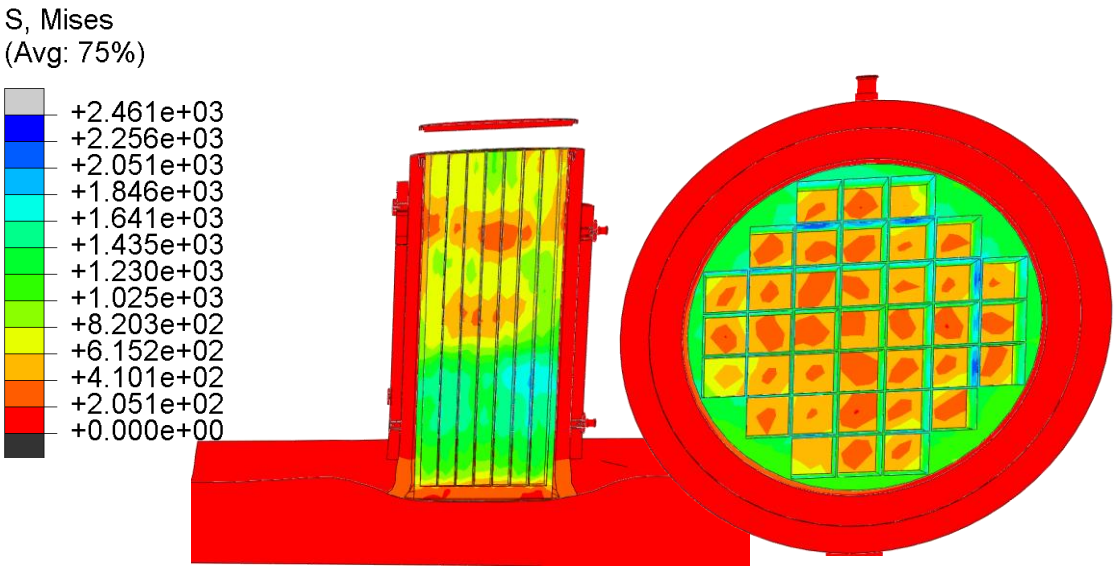

Figure 6.17: Maximum von Mises equivalent stress [MPa] over a rigid base.

Figure 6.17 shows the maximum von Mises stress value obtained is 2461 MPa. Based on the spectrum, the maximum stress is obtained on the facet of the inner-shell. This maximum stress exceeded the input yield stress of 410 MPa for stainless-steel grade 304L. When compared with inner-shell material, the outer-shell experienced less energy concentration. This, because the edge of the bottom facet sheared. Therefore, the energy absorbed by the IDSC during the simulation showed that the entire geometry of the IDSC will experience a larger plastic deformation if it falls over a rigid surface.

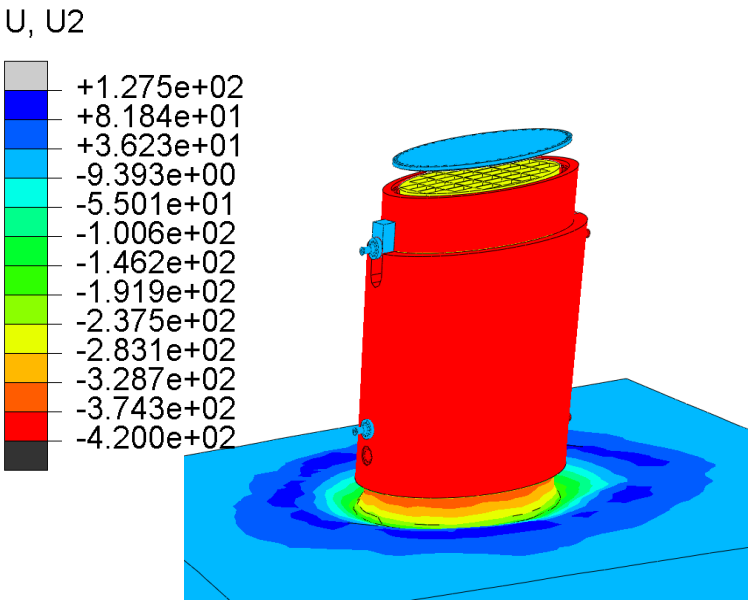

Figure 6.18: Illustration of the maximum displacement at an angle of 90 degrees over a rigid base.

The nodal displacement results in the U2 (Y-axis) direction are shown in Figure 6.18. The maximum compressive displacement undergone by the IDSC is -420 mm. This magnitude of displacement induced shear stress on the top cover of the IDSC.

6.6 Results validation

It is crucial as required in engineering design that any FE-simulation results be validated by another FE-simulation code or a relevant experimental test method. This is to examine whether there is a correlation between both FE-simulation codes and the experimental test method to assure the dependability of the results.

Note that no experimental work was conducted to validate the results obtained by FE-simulation presented in this thesis. Therefore, the results validation in this study was executed with regard to a work study conducted by Shin Lee et al. (2005) using both LS-DYNA3D and ABAQUS/Explicit.

6.6.1 Comparison of results

Table 6.2: Von Mises stress on the inner and outer shell using ABAQUS/Explicit

Orientations	Inner Shell (TSC)			Outer Shell (TC)		
	Stress (MPa)	Displacement (mm)	Plastic strain	Stress (MPa)	Displacement (mm)	Plastic strain
Vertical drop	413	-66.49	0.003	377.8	-66.49	0.012
Oblique drop 45 degrees	587.7	-66.46	0.207	740.4	-66.46	0.395
Oblique drop 60 degrees	587.8	-66.42	0.207	889.9	-73.09	0.553

The results obtained by the current work study are shown in Table 6.2.

Table 6.3: Von Mises stress for inner and outer shell using ABAQUS/Explicit and LS-DYNA3D

Orientations	ABAQUS/Explicit (MPa)		LS-DYNA3D (MPa)	
Drop orientation	Inner shell	Outer shell	Inner shell	Outer shell
Vertical drop	278	273	260	262
Oblique drop 68 degrees	288	298	286	299

Table 6.3 are the results of the work study conducted by Shin Lee et al. (2005) using both LS-DYNA3D and ABAQUS/Explicit. It is clear from these results that a high rate of deformation may be expected during an oblique drop. Thus, it is important to test different impact angles to ascertain the highest possible deformation.

The tabulated results in both previous and current studies demonstrated that higher von Mises stress can be expected during an oblique drop. The results in both studies show that the impact energy absorbed by the outer-shell (the transfer cask – TC) compared to the inner shell (the transportable storage cask – TSC) is less during the vertical drop. However, analysing the handling drop at an oblique angle can result in a higher impact energy being absorbed on the outer-shell as compared to the inner-shell.

The (TSC) absorbed more energy during the vertical drop and less during the two oblique drops, while the outer-shell absorbed less energy during the vertical impact as compared to the two oblique drops. Owing to the difference in energy absorptions, there were differences

between the spatial displacement at nodes and the equivalent plastic strain at integration points. The equivalent plastic strain values obtained for the two oblique drops are higher compared to the vertical drop. The two plastic strain values were 0.395 and 0.55 respectively, and higher than the material plastic limits of 0.32 and 0.22 for the TSC and the TC respectively. Base on the stress-strain curves drawn as a reflexion of the input materials, is that once the two maximum plastic strain values exceed the set plastic limits fractures should be expected along the shape of the IDSC. ABAQUS/Explicit code uses equivalent plastic strain (PEEQ) as scale to determine plastic deformation along a certain region of the structure (Marohnić, 2016).

6.6.2 Results summary

The FE-simulations procedure behaves like three different/separate modelling techniques, each dependent on their orientations. Larger stress concentrations could be detected around the regions 2 m from the bottom face of the TSC and along the full length of the TC. The stress concentrations with a rigid base went about uncontrolled, distributed over a larger area in the vertical drop orientation to a point of inducing shearing stress. Refer to Figure 6.18.
As shearing stress could be detected while falling on the rigid body, it was assumed to be the case for the two oblique orientations as well. This shearing stress affected mostly the top cover to an extent that it was removed from its initial position. Owing to the shearing stress, less deformation was detected by the TSC, when it was dropped on a rigid surface.

During the FE-simulation over a deformable base (concrete floor), it was decided that the reinforced concrete had to be taken as plain concrete. This was to access the magnitude of the energy dissipation in the deformable base.

Table 6.4: Results summary for different mesh density ratios using ABAQUS/Explicit

Orientations	Inner -Shell (TSC)		Outer- Shell (TC)	
Mesh density ratios	Stresses (MPa)	PEEQ	Stresses (MPa)	PEEQ
1:6	408	0.0052	369	0.0137
1:8	410	0.0035	370	0.1341
1:10	412	0.0033	375	0.0124
1:12	413	0.0033	378	0.0124

Relatively high stress concentrations are experienced up to two metres from the bottom face of the IDSC. As per the tabulated stress magnitudes of the two finer mesh ratios, a small percentage different (0.4%) occurred on both inner-shell and outer-shell. The percentage difference of the results shows acceptable convergence for the refined mesh, as illustrated in Table 6.4.

Table 6.5: Results summary for inner and outer shell using ABAQUS/Explicit

Orientations	Inner Shell (TSC)			Outer Shell (TC)		
	Stress (MPa)	Displacement (mm)	Plastic strain	Stress (MPa)	Displacement (mm)	Plastic strain
Vertical drop	413	- 66.49	0.003	377.8	- 66.49	0.012
Oblique drop 45 degrees	587.7	- 66.46	0.207	740.4	- 66.46	0.395
Oblique drop 60 degrees	587.8	- 66.42	0.207	889.9	-73.09	0.553

The all three orientations illustrations that during the transportations stage of the IDSC to the final disposal a handling drop should be avoided at any drop angle, since all induce a plastic strain value of greater than zero. With inclusion of the tabulated spatial displacements at nodes, a lager displacement was obtained at the outer-shell while analysing a drop at an angle of 60 degrees.

6.7 Summary of boundary conditions

In many commercial industries such as cell phone packaging and engineering industries, the drop test method is important and soundly corresponds with experimental results. The only limitation considered with the experimental method in general is that the test only resulted in an intact model or damage absorbed by the tested model. It is not easy to see damage propagation along the shape of the model (IDSC).

Some important parameters considered are the impact height and total weight. Therefore, the magnitude of the elastic energy or plastic energy absorbed by the IDSC during the impact does not isolate itself from the two considered parameters. However, besides the parameters mentioned, the IDSC structure was tested at different angles of impact and different base surface textures. The latter were made rigid and deformable bases. These were important to investigate the behaviours of the IDSC when hitting the top surface of the concrete base or pad at an appropriate impact angle.

The drop position or impact angle of the IDSC before impact is difficult to observe as the total drop test occurs in less than 300 ms. Owing to the complexity of the IDSC structure, it was understood to be time-consuming to analyse the IDSC at different heights. This occurs merely because several components of the IDSC are assembled together and treated as one unit or assembly. Otherwise different heights could have been taken into account to establish an indication of what height the IDSC can withstand.

Therefore, only one worst case scenario was considered for both DYNA3D and ABAQUS/Explicit FE- simulations, namely a drop from a height of 9 m. Note that the question here is related to the interactions between the IDSC assembly and concrete pad during the impact. Underneath the reinforced concrete pad is the soil, which has a positive rather than a negative effect on the IDSC. The soil does compress during the impact though compacted; this dissipates some of the energy.

Therefore, only the induced effects of the concrete floor on the IDSC are taken into account. This should be carefully analysed to assure or improve the integrity of the IDSC structure. The IDSC structure is constructed of seven components in total, but only one is most crucial: that is the stainless steel canister that provides protection from the SNF assemblies.

7. CONCLUSION, AND RECOMMENDATIONS

7.1 Conclusion

The three modelling techniques used were simple and comprehensive. They were the vertical drop and oblique drop at orientation angles of 45 degrees and 60 degrees. The benefits with these approaches were that it was easy to update the geometry in the FE-model. The geometry of the IDSC could be controlled. The volume and mass could be certified against the real dimensioning of the IDSC.

The difficulties were to capture the large deformations across all the three modelling techniques of the IDSC, and the interactions between the components of the IDSC and the concrete pad. In order to capture the large deformations, the different finer mesh ratios were used over all the components of the IDSC initiated from the default mesh sizes. The first mesh density ratio of 1:6 and 1:8 were used, later reduced to 1:10 and 1:12 of their default. At all three meshing density ratios the results were accepted but were more accurate at the very last finer mesh density ratio that was 1:12.

The results obtained show that the highest von Mises equivalent stresses arise in the case of an oblique drop at an angle of 60 degrees to the horizontal. These were encountered along the length of the IDSC on the outer shell, i.e. the transfer cask (TC).
The inner shell of the IDSC, i.e. the transportable storage cask (TSC), experiences slightly lower stresses in all cases, with a maximum similarly at an oblique angle of 60 degrees. For the three drop cases, all the magnitudes von Mises equivalent stresses exceeded the plastic limit for the particular of IDSC design considered. This does raise a concern relating to damage due to large deformation and deformation rates.

The PEEQ and Von Mises stress obtained during the vertical drop are lower compared to the two oblique angles of 45 degrees and 60 degrees. This is due to the area of contact between the IDSC and the concrete pad while dropped and inertia effect. This means that a larger area hits the concrete pad during the vertical drop and a smaller area in the oblique drops. In the vertical drop the IDSC has a better capability to resist handling drop. The impact will also last for a longer time but the total impulse will be the same. The conclusion is that the vertical fall has a more moderate impact than the oblique fall.

The oblique drop can therefore be well-defined as the most dangerous impact orientation. This behaviour corresponds well with the knowledge with analysis in the safety analysis report for SAR (Magnastor, 2008). Finally, the main purpose of this thesis is achieved since it has been

shown that it is possible to FE-simulate the dynamic event of IDSC drop test with all seven parts considered.

The total energy across the majority of the processed elements was constant but some were close to a constant for an approximate error of about 1%. This is as appraised by ABAQUS/EXPLICIT that the total energy (ETOTAL) in dynamic analysis should be a constant throughout the majority of the simulation process, or close to a constant with an approximate error of 1 %. Refer to Figure 6.3. The behaviour of the dropped orientations of the IDSC in the FE-simulations parallel compared well with regard to their drop height, velocity and oblique angles of the IDSC. The results obtained while tested over both deformable and rigid body seem to correspond well to the experimental drop tests based on the total weight of the IDSC. Further, material properties often fracture in this manner. An interesting observation was that during the rigid base testing very high shear stresses were captured to the extent that fewer plastic deformations were experienced by the TSC. These shear stresses in an IDSC is that of the vertical dropped only, which are allocated in the regions of high stress concentrations and regions of contact interactions between components.

This result requires further investigation to establish if such a correlation exits. The regions with different stress concentration areas were detected in IDSC in a direction along the height of the IDSC. The height is estimated in the thesis as 2 m from the bottom edge of the IDSC. This may be a motivating point of consideration to assess further since the affected regions could help to determine whether the ISDC can resist a handling drop incident.

7.2 Recommendations

The results obtained in the FE-model can be improved by adjusting a few things, such as the parameters that were taken into account. Detailed areas that essentially need to be improved are the meshing ratio of the TSC and top cover, as well as the material description of the reinforced concrete pad. To be able to further assess the TSC and top cover, the current mesh ratio needs to be replaced by a finer mesh size. However, before changing the mesh, a partitioning of the areas under consideration is required. It would, therefore, be desirable to check the central computational time due to the new mesh size. The material description can be improved by assigning the properties of the reinforced concrete rebar precision command in ABAQUS code. Each steel bar requires a proper definition of the reinforced concrete command. The chosen defining method for rebar in the structure and membrane elements is defined by the layers of the reinforcement used as a part of the element section definition (Dassault Systèmes, 2014, Sect 2.2.4). This will permit the material to have different bending properties in tension and compression. An experimental test can be used to examine if there

is connectivity between the cracks and the shear stresses. In this case, the materials of the IDSC behave in the same way. This could explain why some materials of the IDSC resist cracks.

A damage accumulation criterion can be developed to assess the plastic deformation of the IDSC during the two oblique drops (Kwon, 2017). There is enough plastic deformation that damage needs to be considered to assess the safety of the design. A comparison between the results obtained at constant plastic modulus (refer to Figure.5.5) to that could be obtained a different set of plastic strain values (refer to Figure. 5.6).

Based on the yield stresses results obtained while running an experimental uniaxial tensile tests for duplex stainless steel at the set of room temperatures. It was observed that the duplex stainless steel has high yield stress if compared to the grade 304L stainless steel.

Therefore, it is then vital that the designers of the interim dry storage cask to consider the use of duplex stainless at the design stage.

REFERENCES

1. Anon., 2013. *The Finite Element Method for the Analysis of Non-lLinear and Dynamic Systems Non-Linear and Dynamic Systems.* Swiss Federal Institute of Technology Zurich, s.n.
2. Aquaro, D., Zaccari, N., Di Prinzio, M. & Forasassi, G., 2009. Numerical and experimental analysis of the impact of a nuclear spent fuel cask. *Nuclear Engineering and Design,* 240(4): 706-712.
3. Baisden, P. A. & Choppin, G. R., 2007. Nuclear Waste Management and the Nuclear Fuel Cycle. *Radiochemistry and Nuclear Chemistry.*
4. Chopra, A., 1995. *Dynamics of structures Theory and Applications to Earthquake engineering.* Fourth Edition ed. San Francisco, California: Prentice Hall.
5. Choung, J. M. & Cho. S. R., 2008. Study on true stress correction from tensile tests. *Journal of Mechanical Science and Technology,*vol. 22, pp. 1039-1051.
6. Dassault Systèmes, 2014. *Abaqus Theory Guide (6.14),* Sect 2.2.4.
7. Feiveson, H., Z. Mian, M., Ramana. & Hippel, F., 2011. *Managing Spent Fuel from Nuclear Power Reactors*: An Overview of a New Study by the International Panel on Fissile Material.
8. Gu, X., 2016. Mechanical Properties of Concrete and Steel Reinforcement. *Basic Principles of Concrete Structures.* 3rd ed. Tongji University Press, Shanghai. China: Springer-Verlag Berlin Heidelberg, pp. 21-24.
9. Soetaert, K. and Herman,P.M.J. 2009. *A Practical Guide to Ecological Modelling:* Using R as a Simulation Platform. Netherlands Institute of Ecology: Springer Science+Business Media B.V, pp. 273-278.
10. Hyeon, J. H., Sanghee, K. & Thomas, H., 2017. Energy-Based Penetration Model for Local Impact Damaged Concerete Members. *ACI Structural Journal*, No. 114-S97, pp.1189-1200.
11. IAEA, 2004. *Developing Multinational Radioactive Waste Repositories: Infrastructural framework and scenarios of cooperation*. International Atomic Energy Agency.
12. Irgens, F., 2008. *Continuum Mechanics.* Bergen, Norway: Springer-Verlag.
13. Klymyshyn, N., Karri, N., Adkins, H. & Hanson, B., 2013. Structural sensitivity of dry storage canisters. US Department of Energy Used Fuel Disposition Campaign.
14. Kwon, Y. J., 2017. Dynamic and static structural responses of the spent nuclear fuel disposal canister due to the accidental drop and impact on to the ground. *Cogent Engineering (2017), 4: 1373417,* United Kingdom: Taylor & Francis Group, pp. 5-15.
15. Laubscher, R. F., 1997. *An evaluation of strain rate sensitivity of certain stainless steels*, Johannesburg: Rand Afrikaans University.

16. LeVeque, J. R., 2005. *Finite Difference Methods for Differential Equations,* draft version for use in the course amath 585–586 University of Washington, United States of America, pp. 13-15.

17. Macfarlane, A., 2001. Interim Storage of Spent fuel in the United States. Annual Review of Energy and the Environment, 26: 201-235.

18. Magnastor, 2008. *Magnastor System Safety Analysis Report Docket No. 72-1031,* Geogia: s.n.

19. Marohnić, Robert Basan & Tea, 2016. *Constitutive Modeling and Material Behavior,* University of Rijeka Faculty of Engineering, Rijeka, pp. 8-12.

20. Nickell, R. E., 1972. A Survey of Direct Integration Methods in Structural Dynamics. Defense Technical Information Centre.

21. Nishant, K, 2003. Numerical Integration of Nonlinear Structural Models*.* Unpublished dissertation, Texas Tech University, United States of America.

22. Ogunlade, D., Harald, W., Andrew, K., Gisela, P., Jabavu, N. Debbie, S., Mark, H., and Thomas, A., 2006. *Energy policies for sustainable development in South Africa,* Cape Town: Energy Research Centre, University of Cape Town, South Africa.

23. Parks V. J. and Durelli, A. J., 1964. Various Forms of the Strain-displacement Relation Applied to Experimental Strain Analysis. *Experimental Mechanics*, 4(2): 37-47.

24. Peng-Cheng, Z., Takuya, N., Jason, M., Masahiro, I., Mika, K. & Masayoshi, N., 2008. Friction-Based Sliding Between Steel and Steel, Steel and Concrete, and Wood and Stone. *The 14th World Conference on Earthquake Engineering* October 12-17, 2008, Beijing. China: Xiamen University, pp. 6-8.

25. Prasad.B.B, 2018. *The theory of continuum and elasto-plastic materials The theory of continuum and elasto-plastic materials*. Technische Universität Berlin, Faculty V - Mechanical Engineering and Transport Systems. Researchgate: Magdeburg, Saxony-Anhalt, Germany. Volume 3, pp. 45-46.

26. Roylance, D., 2001. *Stress-Strain Curves, Cambridge:* Massachusetts Institute of Technology. of Technology. United States of America.

27. Roylance, D., 2008. *Mechanical Properties of Materials,* Cambridge: Massachusetts Institute of Technology. United States of America.

28. Rigby, D. B., 2010. *Evaluation of the Technical Basis for Extended Dry Storage and Transportation of Used Nuclear Fuel*: United States Nuclear Waste Technical Review Board, pp. 45-46.

29. Seshu, P., 2012. *Finite Element Analysis, Department of Mechanical Engineering.* 10th ed. Mumbai: Asoke, K. Ghosh.

30. Shabana, A. A., 2012. *Theory of Vibration: Discrete and Continuous Systems.* New York: Springer Science & Business Media.

31. Shin Lee, Y., Ryu, C-H, Kim, H-S. & JChoi, Y-J., 2005. A study on the free drop impact of a cask using commercial FEA codes. *Nuclear Engineering and Design*, 235(20): 2219-2226.

32. Sippola, P., 2011. *Finite element simulation of thick steel plate stamping,* Unpublished Masters dissertaion: Tampere University of Technology. Finland.

33. Wriggers, P., 2006. *Analysis and Simulation of Contact Problems.* Hannover. Germany : Springer-Verlag, pp. 45-114.

34. Zienkiewicz, O. C. & Tailor, L. R., 1967. *The Finite Element Method.* 5th ed. London: Butterworth-Heinemann.

APPENDIX. A

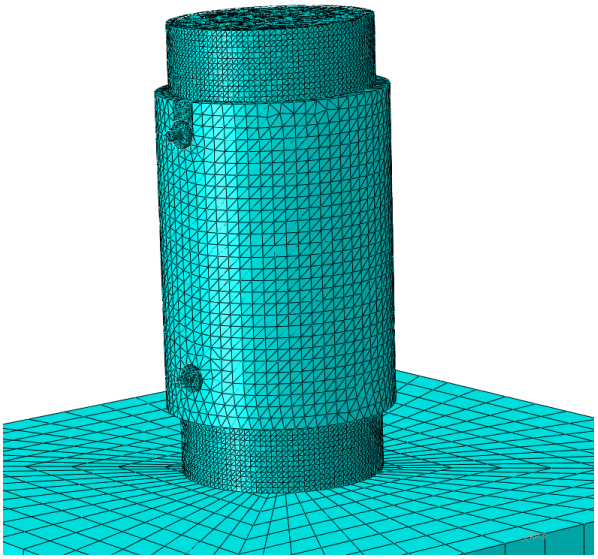

Figure A-1: First mesh density ratio of 1:12 at vertical drop

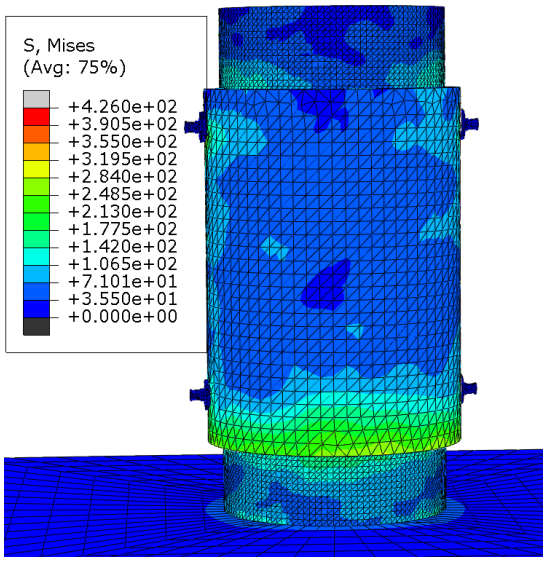

Figure A-2: Von Mises stress at mesh density ratio of 1:12 vertical drop

The results here were compared with that obtained using finer meshing. Refer to Figure A-5.

Step	Increment	Total Time	CPU Time	Step Time	Stable Time Inc	Kinetic Energy	Total Energy
1	69045	0.00420943	28788.4	0.00420943	6.02868e-08	1.63229e+09	9.48372e+09
1	69367	0.00422877	28908.6	0.00422877	6.02868e-08	1.62744e+09	9.48372e+09
1	69689	0.00424812	29028.8	0.00424812	6.02868e-08	1.62326e+09	9.48371e+09
1	69721	0.00425004	29041.8	0.00425004	6.02868e-08	1.62275e+09	9.48371e+09
1	70040	0.0042692	29160.9	0.0042692	6.02868e-08	1.61665e+09	9.48371e+09
1	70362	0.00428854	29280.9	0.00428854	6.02868e-08	1.60886e+09	9.48371e+09
1	70685	0.00430795	29401.2	0.00430795	6.02868e-08	1.59912e+09	9.48371e+09
1	71007	0.00432729	29521.2	0.00432729	6.02868e-08	1.58846e+09	9.48371e+09
1	71330	0.00434669	29641.4	0.00434669	6.02868e-08	1.57913e+09	9.4837e+09
1	71653	0.0043661	29761.7	0.0043661	6.02868e-08	1.57163e+09	9.4837e+09
1	71976	0.0043855	29881.8	0.0043855	6.02868e-08	1.56551e+09	9.48369e+09
1	72299	0.0044049	30002.1	0.0044049	6.02868e-08	1.56013e+09	9.48369e+09
1	72621	0.00442424	30122.1	0.00442424	6.02868e-08	1.55534e+09	9.48369e+09
1	72943	0.00444359	30242	0.00444359	6.02868e-08	1.5514e+09	9.48368e+09
1	73266	0.00446299	30362.2	0.00446299	6.02868e-08	1.54763e+09	9.48368e+09
1	73589	0.00448239	30482.3	0.00448239	6.02868e-08	1.54262e+09	9.48368e+09
1	73883	0.00450005	30592.7	0.00450005	6.02868e-08	1.53576e+09	9.48367e+09
1	74202	0.00451921	30711.8	0.00451921	6.02868e-08	1.52575e+09	9.48367e+09
1	74525	0.00453862	30832.1	0.00453862	6.02868e-08	1.51351e+09	9.48366e+09
1	74848	0.00455802	30952.4	0.00455802	6.02868e-08	1.50075e+09	9.48366e+09
1	75171	0.00457742	31072.7	0.00457742	6.02868e-08	1.48922e+09	9.48366e+09
1	75494	0.00459683	31193	0.00459683	6.02868e-08	1.47901e+09	9.48366e+09
1	75816	0.00461617	31313	0.00461617	6.02868e-08	1.46969e+09	9.48365e+09
1	76138	0.00463551	31433	0.00463551	6.02868e-08	1.46118e+09	9.48365e+09
1	76460	0.00465485	31553.1	0.00465485	6.02868e-08	1.45439e+09	9.48365e+09
1	76782	0.0046742	31673	0.0046742	6.02868e-08	1.44942e+09	9.48365e+09
1	77104	0.00469354	31793	0.00469354	6.02868e-08	1.44424e+09	9.48365e+09
1	77426	0.00471288	31913.1	0.00471288	6.02868e-08	1.43738e+09	9.48366e+09
1	77748	0.00473222	32033.2	0.00473222	6.02868e-08	1.43073e+09	9.48366e+09
1	78044	0.00475	32144.5	0.00475	6.02868e-08	1.42681e+09	9.48366e+09
1	78363	0.00476917	32263.8	0.00476917	6.02868e-08	1.42554e+09	9.48366e+09
1	78685	0.00478851	32384	0.00478851	6.02868e-08	1.42483e+09	9.48366e+09
1	79007	0.00480785	32504.2	0.00480785	6.02868e-08	1.42317e+09	9.48367e+09
1	79329	0.00482719	32624.3	0.00482719	6.02868e-08	1.42035e+09	9.48367e+09
1	79651	0.00484654	32744.4	0.00484654	6.02868e-08	1.41613e+09	9.48367e+09
1	79973	0.00486588	32864.5	0.00486588	6.02868e-08	1.41039e+09	9.48367e+09
1	80295	0.00488522	32984.6	0.00488522	6.02868e-08	1.40376e+09	9.48367e+09
1	80617	0.00490457	33104.7	0.00490457	6.02868e-08	1.39695e+09	9.48367e+09
1	80939	0.00492391	33224.8	0.00492391	6.02868e-08	1.38984e+09	9.48368e+09
1	81261	0.00494325	33344.8	0.00494325	6.02868e-08	1.38286e+09	9.48368e+09
1	81583	0.00496259	33464.7	0.00496259	6.02868e-08	1.37566e+09	9.48368e+09
1	81905	0.00498202	33584.9	0.00498202	6.28354e-08	1.36741e+09	9.48368e+09
1	82191	0.005	33692.3	0.005	6.28329e-08	1.35926e+09	9.48368e+09

Search Text

Step	Increment	Total Time	CPU Time	Step Time	Stable Time Inc	Kinetic Energy
1	69045	0.00420943	28788.4	0.00420943	6.02868e-08	1.63229e+09
1	69367	0.00422877	28908.6	0.00422877	6.02868e-08	1.62744e+09
1	69689	0.00424812	29028.8	0.00424812	6.02868e-08	1.62326e+09
1	69721	0.00425004	29041.8	0.00425004	6.02868e-08	1.62275e+09
1	70040	0.0042692	29160.9	0.0042692	6.02868e-08	1.61665e+09
1	70362	0.00428854	29280.9	0.00428854	6.02868e-08	1.60886e+09
1	70685	0.00430795	29401.2	0.00430795	6.02868e-08	1.59912e+09

Log | Errors | ! Warnings | Output | Data File | Message File | Status File

```
-------------------------------------------------------------------------------
 MODEL INFORMATION (IN GLOBAL X-Y COORDINATES)
-------------------------------------------------------------------------------

   Total mass in model = 1.84427E+05
   Center of mass of model = (-3.228495E-05, 9.600102E+03,-1.203171E-05)

    Moments of Inertia :
                 About Center of Mass              About Origin
      I(XX)           1.022600E+12                 1.801979E+13
      I(YY)           1.976423E+12                 1.976423E+12
      I(ZZ)           1.022600E+12                 1.801979E+13
      I(XY)           1.307597E+04                 7.023718E+04
      I(YZ)          -7.991339E+02                 2.050328E+04
      I(ZX)          -6.362209E+03                -6.362209E+03

-------------------------------------------------------------------------------
 STABLE TIME INCREMENT INFORMATION
-------------------------------------------------------------------------------


  The stable time increment estimate for each element is based on
  linearization about the initial state.


   Initial time increment = 3.71449E-08

   Statistics for all elements:
      Mean = 4.50260E-06
      Standard deviation = 6.00730E-05

   Most critical elements:
    Element number   Rank    Time increment   Increment ratio
    (Instance name)
   ---------------------------------------------------------
       20579           1       3.714493E-08      1.000000E+00
    Body Cover
       26491           2       4.823087E-08      7.701483E-01
    Body Cover
       27401           3       6.066345E-08      6.123114E-01
    Body Cover
       22915           4       7.468164E-08      4.973769E-01
    Body Cover
       52113           5       7.674272E-08      4.840189E-01
    Cask handle lock
       52113           6       7.675295E-08      4.839544E-01
    Cask handle lock_4
       52114           7       8.691043E-08      4.273932E-01
    Cask handle lock
       52114           8       8.692081E-08      4.273422E-01
    Cask handle lock_4
       18477           9       8.801915E-08      4.220096E-01
```

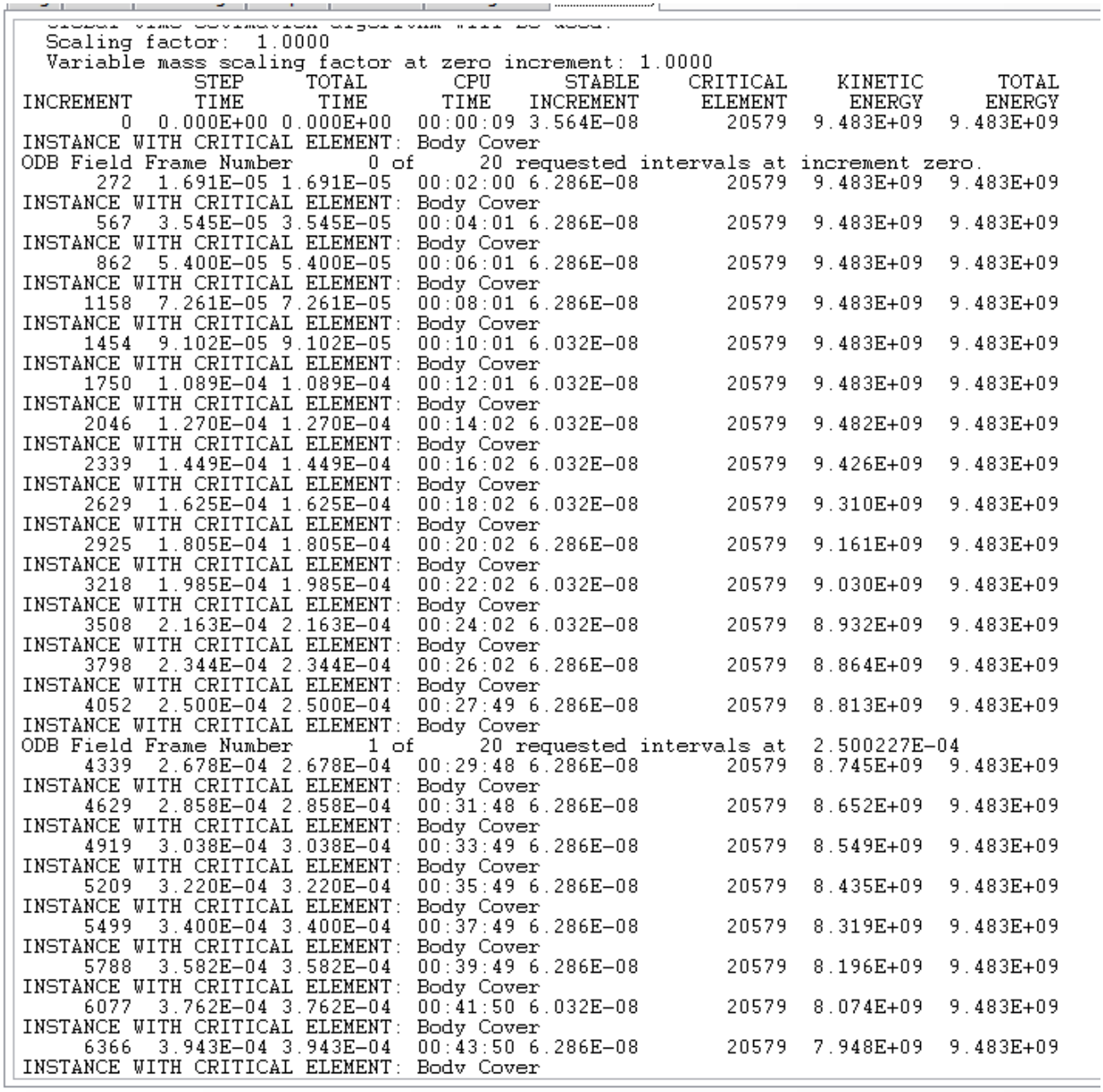

```
  Scaling factor:  1.0000
  Variable mass scaling factor at zero increment: 1.0000
             STEP      TOTAL       CPU      STABLE    CRITICAL    KINETIC      TOTAL
INCREMENT     TIME       TIME      TIME   INCREMENT     ELEMENT     ENERGY     ENERGY
        0  0.000E+00 0.000E+00  00:00:09 3.564E-08       20579  9.483E+09  9.483E+09
INSTANCE WITH CRITICAL ELEMENT: Body Cover
ODB Field Frame Number      0 of     20 requested intervals at increment zero.
      272  1.691E-05 1.691E-05  00:02:00 6.286E-08       20579  9.483E+09  9.483E+09
INSTANCE WITH CRITICAL ELEMENT: Body Cover
      567  3.545E-05 3.545E-05  00:04:01 6.286E-08       20579  9.483E+09  9.483E+09
INSTANCE WITH CRITICAL ELEMENT: Body Cover
      862  5.400E-05 5.400E-05  00:06:01 6.286E-08       20579  9.483E+09  9.483E+09
INSTANCE WITH CRITICAL ELEMENT: Body Cover
     1158  7.261E-05 7.261E-05  00:08:01 6.286E-08       20579  9.483E+09  9.483E+09
INSTANCE WITH CRITICAL ELEMENT: Body Cover
     1454  9.102E-05 9.102E-05  00:10:01 6.032E-08       20579  9.483E+09  9.483E+09
INSTANCE WITH CRITICAL ELEMENT: Body Cover
     1750  1.089E-04 1.089E-04  00:12:01 6.032E-08       20579  9.483E+09  9.483E+09
INSTANCE WITH CRITICAL ELEMENT: Body Cover
     2046  1.270E-04 1.270E-04  00:14:02 6.032E-08       20579  9.482E+09  9.483E+09
INSTANCE WITH CRITICAL ELEMENT: Body Cover
     2339  1.449E-04 1.449E-04  00:16:02 6.032E-08       20579  9.426E+09  9.483E+09
INSTANCE WITH CRITICAL ELEMENT: Body Cover
     2629  1.625E-04 1.625E-04  00:18:02 6.032E-08       20579  9.310E+09  9.483E+09
INSTANCE WITH CRITICAL ELEMENT: Body Cover
     2925  1.805E-04 1.805E-04  00:20:02 6.286E-08       20579  9.161E+09  9.483E+09
INSTANCE WITH CRITICAL ELEMENT: Body Cover
     3218  1.985E-04 1.985E-04  00:22:02 6.032E-08       20579  9.030E+09  9.483E+09
INSTANCE WITH CRITICAL ELEMENT: Body Cover
     3508  2.163E-04 2.163E-04  00:24:02 6.032E-08       20579  8.932E+09  9.483E+09
INSTANCE WITH CRITICAL ELEMENT: Body Cover
     3798  2.344E-04 2.344E-04  00:26:02 6.286E-08       20579  8.864E+09  9.483E+09
INSTANCE WITH CRITICAL ELEMENT: Body Cover
     4052  2.500E-04 2.500E-04  00:27:49 6.286E-08       20579  8.813E+09  9.483E+09
INSTANCE WITH CRITICAL ELEMENT: Body Cover
ODB Field Frame Number      1 of     20 requested intervals at  2.500227E-04
     4339  2.678E-04 2.678E-04  00:29:48 6.286E-08       20579  8.745E+09  9.483E+09
INSTANCE WITH CRITICAL ELEMENT: Body Cover
     4629  2.858E-04 2.858E-04  00:31:48 6.286E-08       20579  8.652E+09  9.483E+09
INSTANCE WITH CRITICAL ELEMENT: Body Cover
     4919  3.038E-04 3.038E-04  00:33:49 6.286E-08       20579  8.549E+09  9.483E+09
INSTANCE WITH CRITICAL ELEMENT: Body Cover
     5209  3.220E-04 3.220E-04  00:35:49 6.286E-08       20579  8.435E+09  9.483E+09
INSTANCE WITH CRITICAL ELEMENT: Body Cover
     5499  3.400E-04 3.400E-04  00:37:49 6.286E-08       20579  8.319E+09  9.483E+09
INSTANCE WITH CRITICAL ELEMENT: Body Cover
     5788  3.582E-04 3.582E-04  00:39:49 6.286E-08       20579  8.196E+09  9.483E+09
INSTANCE WITH CRITICAL ELEMENT: Body Cover
     6077  3.762E-04 3.762E-04  00:41:50 6.032E-08       20579  8.074E+09  9.483E+09
INSTANCE WITH CRITICAL ELEMENT: Body Cover
     6366  3.943E-04 3.943E-04  00:43:50 6.286E-08       20579  7.948E+09  9.483E+09
INSTANCE WITH CRITICAL ELEMENT: Body Cover
```

Figure A-3: Results output mesh density ratio of 1:12 at vertical drop

The output results depict that the kinetic energy and total energy of most of the elements are shown in Figure A-3 for a mesh density such as 1:12.

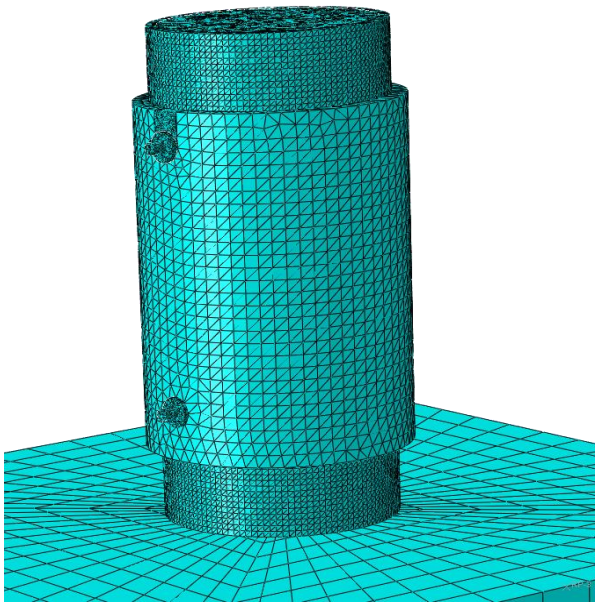

Figure A-4: Second mesh density ratio of 1:6 at vertical drop

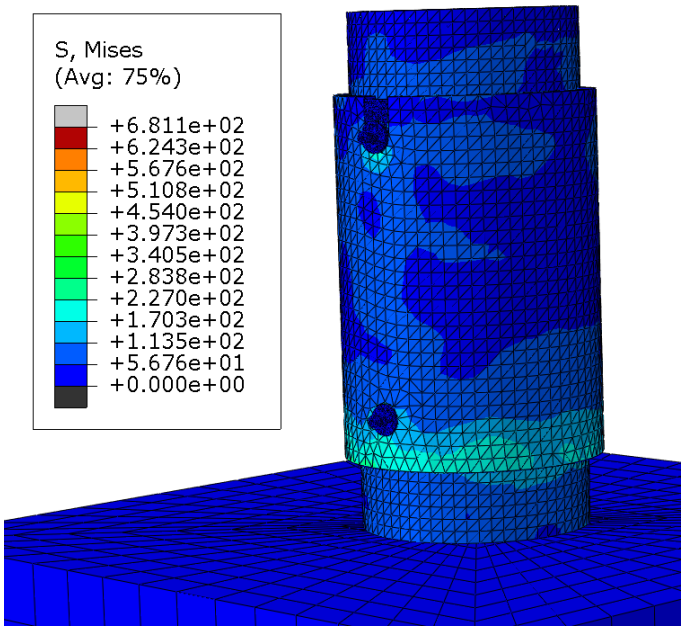

Figure A-5: Von Mises stress at mesh density ratio of 1:6 vertical drop

The results obtained here in comparison to that of the mesh density ratio of 1:12 portray that using finer meshing density ratio of 1:12, the accuracy in results could be obtained. Since the aim in most of the dynamic FE-simulations is to capture a larger magnitude of deformation as possible.

Log | Errors | ! Warnings | Output | Data File | Message File | Status File

```
MODEL INFORMATION (IN GLOBAL X-Y COORDINATES)

  Total mass in model = 291.41
  Center of mass of model = (-1.411370E-02, 1.067241E+04, 1.667093E-02)

   Moments of Inertia :
                  About Center of Mass                  About Origin
      I(XX)           1.961682E+09                  3.515383E+10
      I(YY)           2.104178E+09                  2.104178E+09
      I(ZZ)           1.955526E+09                  3.514767E+10
      I(XY)           2.550412E+04                  6.939900E+04
      I(YZ)          -2.285877E+04                 -7.470686E+04
      I(ZX)          -2.020948E+04                 -2.020941E+04

STABLE TIME INCREMENT INFORMATION

  The stable time increment estimate for each element is based on
  linearization about the initial state.

   Initial time increment = 3.71449E-08

   Statistics for all elements:
      Mean = 1.75028E-06
      Standard deviation = 2.67229E-06

   Most critical elements:
    Element number    Rank    Time increment    Increment ratio
    (Instance name)
    ------------------------------------------------------------
       20579           1       3.714491E-08      1.000000E+00
    Body Cover
        9048           2       4.058172E-08      9.153116E-01
    Cask body1
       13521           3       4.062705E-08      9.142902E-01
    Cask body1
       26491           4       4.823087E-08      7.701482E-01
    Body Cover
       15036           5       5.105177E-08      7.275930E-01
    Cask body1
       13518           6       5.119920E-08      7.254979E-01
    Cask body1
       97263           7       5.129532E-08      7.241385E-01
    Canister stainless steel
       84365           8       5.607045E-08      6.624686E-01
    Canister stainless steel
       27401           9       6.066345E-08      6.123112E-01
    Body Cover
       79207          10       6.295741E-08      5.900007E-01
    Canister stainless steel

  Instance name for the most critical element will be printed if the critical
  element changes or at the beginning of a new page.
```

Job: 2-3newsize Status: Completed

Step	Increment	Total Time	CPU Time	Step Time	Stable Time Inc	Kinetic Energy	Total Energy
1	1461	9.16222e-05	120.2	9.16222e-05	6.28592e-08	9.4577e+11	9.4577e+11
1	2390	0.00015002	205.9	0.00015002	6.28592e-08	9.4577e+11	9.4577e+11
1	3859	0.000242367	325.7	0.000242367	6.28592e-08	9.4577e+11	9.4577e+11
1	4776	0.000300014	396.6	0.000300014	6.28592e-08	9.4577e+11	9.4577e+11
1	6356	0.000399339	516.4	0.000399339	6.28592e-08	9.4577e+11	9.4577e+11
1	7162	0.000450008	577.9	0.000450008	6.28592e-08	9.4577e+11	9.4577e+11
1	8741	0.000549271	697.7	0.000549271	6.28592e-08	9.4577e+11	9.4577e+11
1	9548	0.000600002	758.4	0.000600002	6.28592e-08	9.4577e+11	9.4577e+11
1	11113	0.000698385	878.2	0.000698385	6.28592e-08	9.28713e+11	9.45704e+11
1	11935	0.000750059	942.3	0.000750059	6.28592e-08	9.25622e+11	9.45428e+11
1	13478	0.000847059	1062.1	0.000847059	6.28592e-08	9.13151e+11	9.44917e+11
1	14321	0.000900053	1127.6	0.000900053	6.28592e-08	9.10961e+11	9.44832e+11
1	15858	0.000996676	1247.4	0.000996676	6.28592e-08	9.11312e+11	9.44785e+11
1	16707	0.00105005	1314	0.00105005	6.28592e-08	9.05779e+11	9.4471e+11
1	18238	0.00114629	1433.9	0.00114629	6.2858e-08	8.94729e+11	9.44557e+11
1	19093	0.00120004	1501.1	0.00120004	6.2858e-08	8.93411e+11	9.44515e+11
1	20619	0.00129597	1620.9	0.00129597	6.2858e-08	8.94876e+11	9.44451e+11
1	21479	0.00135004	1688.4	0.00135004	6.2858e-08	8.93886e+11	9.44401e+11
1	22995	0.00144534	1808.3	0.00144534	6.2858e-08	8.89167e+11	9.44262e+11
1	23865	0.00150003	1876.7	0.00150003	6.2858e-08	8.87082e+11	9.44149e+11
1	25379	0.00159521	1996.5	0.00159521	6.2858e-08	8.83579e+11	9.43893e+11
1	26251	0.00165002	2065.6	0.00165002	6.2858e-08	8.79523e+11	9.43765e+11
1	27771	0.00174558	2185.5	0.00174558	6.2858e-08	8.72198e+11	9.43548e+11
1	28637	0.00180002	2253.9	0.00180002	6.2858e-08	8.69589e+11	9.43412e+11
1	30150	0.00189513	2373.6	0.00189513	6.2858e-08	8.66315e+11	9.43179e+11
1	31023	0.00195001	2442.7	0.00195001	6.2858e-08	8.64349e+11	9.43038e+11
1	32535	0.00204506	2562.5	0.00204506	6.2858e-08	8.60397e+11	9.42781e+11
1	33409	0.00210001	2631.7	0.00210001	6.2858e-08	8.58206e+11	9.42626e+11
1	34922	0.00219512	2751.5	0.00219512	6.2858e-08	8.54509e+11	9.4233e+11
1	35795	0.00225	2820.7	0.00225	6.2858e-08	8.51997e+11	9.42152e+11
1	37315	0.00234555	2940.6	0.00234555	6.2858e-08	8.47146e+11	9.4185e+11
1	38182	0.00240006	3009.2	0.00240006	6.2858e-08	8.44875e+11	9.41685e+11
1	39691	0.00249492	3129.1	0.00249492	6.2858e-08	8.41891e+11	9.41431e+11
1	40568	0.00255005	3198.6	0.00255005	6.2858e-08	8.4004e+11	9.41296e+11
1	42082	0.00264523	3318.4	0.00264523	6.2858e-08	8.36702e+11	9.41061e+11
1	42954	0.00270005	3387.5	0.00270005	6.2858e-08	8.35102e+11	9.40918e+11
1	44474	0.0027956	3507.4	0.0027956	6.2858e-08	8.32061e+11	9.40665e+11
1	45340	0.00285004	3576	0.00285004	6.2858e-08	8.29732e+11	9.40502e+11
1	46849	0.0029449	3695.7	0.0029449	6.2858e-08	8.25582e+11	9.40165e+11
1	47726	0.003	3765.5	0.003	6.2858e-08	8.23622e+11	9.39971e+11

Figure A-6: Results output mesh density ratio of 1:6 at vertical drop.

The output results here are presented for the kinetic energy and total energy of most of the elements. This is to illustrate how the energy variations along the elements of the model. An important point of observation was that the kinetic energy and total energy of most of the elements increased. This leads to the accuracy of the results.

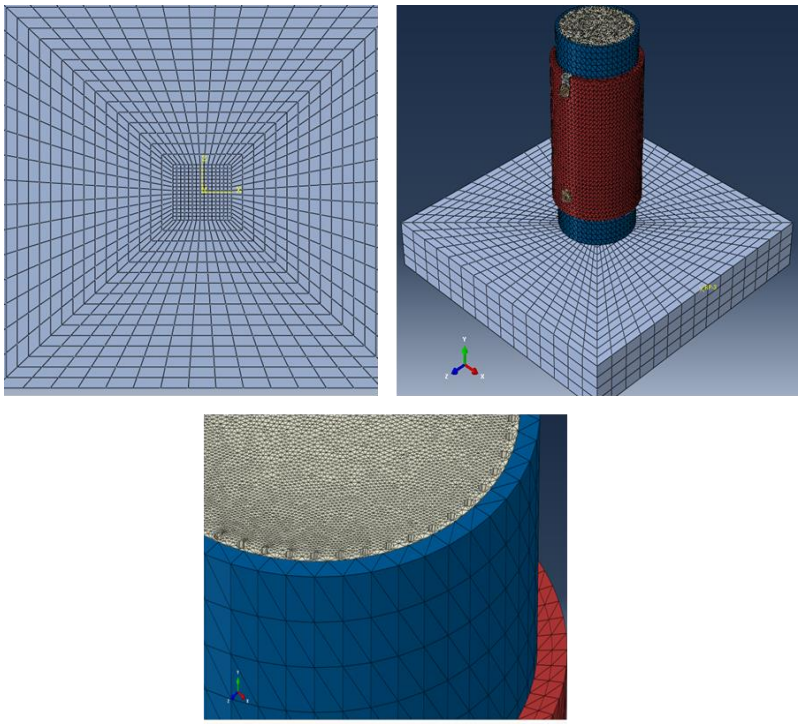

Figure A-7: Third mesh density ratio of 1:12 at vertical drop

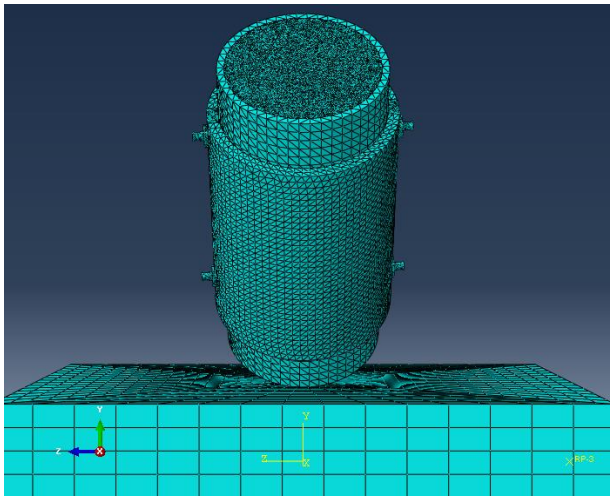

Figure A-8: Mesh density ratio of 1:12 at oblique drop 45 degrees

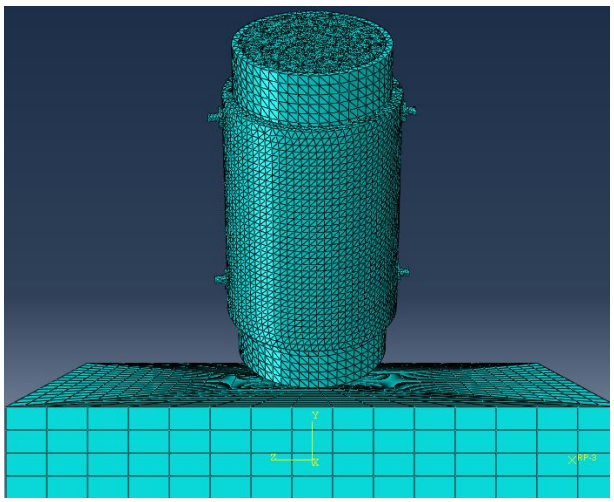

Figure A- 9: Mesh density ratio of 1:12 at oblique drop 60 degrees

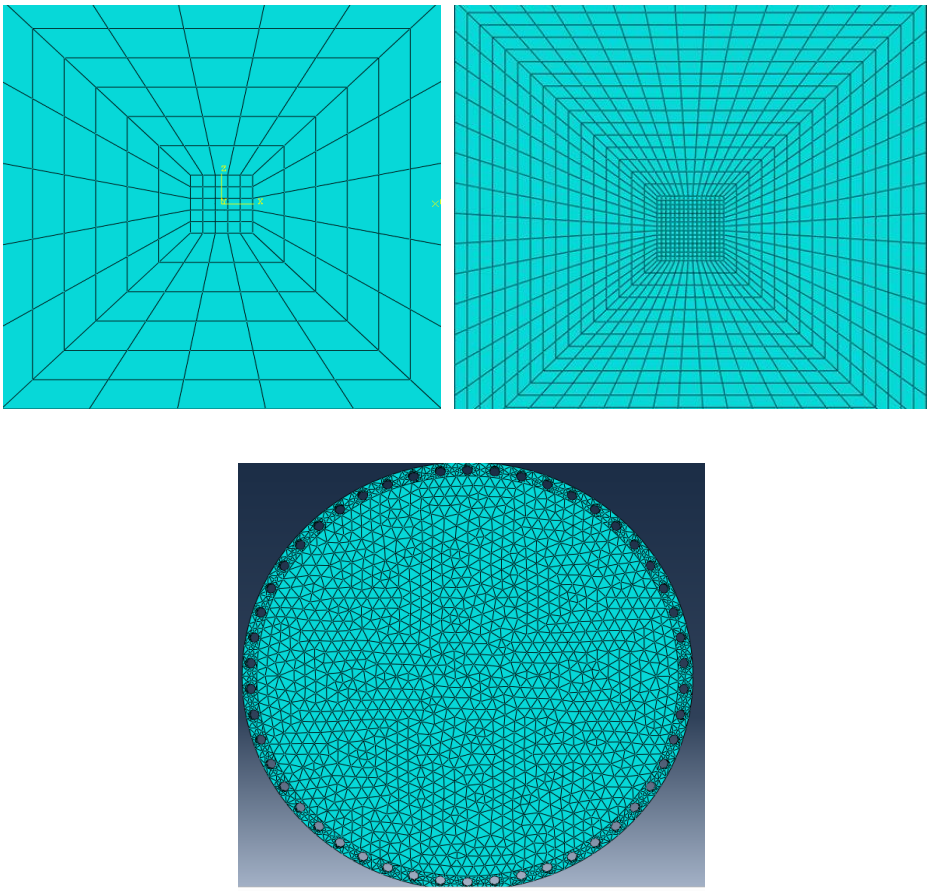

Figure A-10: Mesh density ratio of 1:6 and 1:12